



Universiteit
Leiden
The Netherlands

Imaging complex model catalysts in action: From surface science towards industrial practice using high-pressure scanning tunneling microscopy

Mom, R.V.

Citation

Mom, R. V. (2017, June 29). *Imaging complex model catalysts in action: From surface science towards industrial practice using high-pressure scanning tunneling microscopy*. Retrieved from <https://hdl.handle.net/1887/51108>

Version: Not Applicable (or Unknown)

License: [Licence agreement concerning inclusion of doctoral thesis in the Institutional Repository of the University of Leiden](#)

Downloaded from: <https://hdl.handle.net/1887/51108>

Note: To cite this publication please use the final published version (if applicable).

Cover Page



Universiteit Leiden



The handle <http://hdl.handle.net/1887/51108> holds various files of this Leiden University dissertation

Author: Mom, R.V.

Title: Imaging complex model catalysts in action: From surface science towards industrial practice using high-pressure scanning tunneling microscopy

Issue Date: 2017-06-29

Imaging Complex Model Catalysts in Action

From Surface Science Towards Industrial Practice
Using High-Pressure Scanning Tunneling Microscopy

Proefschrift

ter verkrijging van
de graad van Doctor aan de Universiteit Leiden,
op gezag van Rector Magnificus prof. mr. C.J.J.M. Stolker,
volgens besluit van het College voor Promoties
te verdedigen op donderdag 29 juni 2017
klokke 16:15

door

Rik Valentijn Mom

geboren te Haarlem
in 1988

Promotor:
Prof. dr. J.W.M. Frenken *Universiteit Leiden*

Co-promotor:
dr. I.M.N. Groot *Universiteit Leiden*

Promotiecommissie:
Prof. dr. U. Diebold *Technische Universität Wien*
dr. J.V. Lauritsen *Aarhus University*
Prof. dr. M.T.M. Koper *Universiteit Leiden*
Prof. dr. E.R. Eliel *Universiteit Leiden*

Casimir PhD series 2017-13, Delft-Leiden

ISBN 978-90-8593-296-3

An electronic version of this thesis can be found at <https://openaccess.leidenuniv.nl>

The work described in this thesis has been performed at the Huygens-Kamerlingh Onnes Laboratory, Leiden Institute of Physics, Leiden University, The Netherlands. The project was financially supported by a Dutch SmartMix grant and by NIMIC partner organizations through NIMIC, a public-private partnership. More information can be found at <https://nimic.physics.leidenuniv.nl>

The front cover shows an impression of a high-pressure scanning tunneling microscopy experiment at the atomic level. The ball models represent the molecules and catalyst nanoparticles present during the hydrodesulfurization reaction studied in this thesis. The back cover shows a similar impression for the oxidation of Au(111), where the depicted particle is the structure proposed for the most dense phase of Au surface oxide observed in this thesis.

Table of Contents

1	Introduction.....	1
1.1	Understanding a catalytic process.....	2
1.2	The role of surface science.....	4
1.3	In this thesis.....	5
2	Tuning the properties of molybdenum oxide on Al₂O₃/NiAl(110): metal versus oxide deposition	9
2.1	Introduction.....	10
2.2	Methods.....	11
2.2.1	XPS analysis.....	11
2.2.2	Sample preparation.....	11
2.2.3	Particle statistics.....	12
2.3	Model for nucleation on Al ₂ O ₃ /NiAl(110).....	13
2.4	Results and discussion.....	14
2.4.1	Nucleation of metallic Mo and MoO _x	14
2.4.2	Preparation of MoO _x via Mo.....	18
2.5	Conclusion.....	20
	Supporting information.....	24
2.6	Mo coverage from STM images.....	25
2.7	XPS analysis.....	27
3	In situ observations of an active MoS₂ hydrodesulfurization model catalyst	29
3.1	Introduction.....	30
3.2	Results and discussion.....	31
3.3	Conclusion.....	38
3.4	Methods.....	39
3.4.1	Model catalyst preparation.....	39
3.4.2	High-pressure experiments.....	39
3.4.3	Theoretical analysis.....	39
	Supporting information.....	45
3.5	Appearance of MoS ₂ edge structures in scanning tunneling microscopy.....	46
3.6	Effect of the Au support on the relative stability of MoS ₂ edge structures.....	47
3.7	Comparison of the calculations to literature.....	48
3.8	CH ₃ SH adsorption on MoS ₂	48

4 The growth and stability of Au surface oxides on WO₃/Au(111) and ReO₃/Au(111) inverse model catalysts.....	51
4.1 Introduction.....	52
4.2 Methods.....	53
4.2.1 Model catalyst preparation.....	53
4.2.2 Generation of Au oxide precoverage.....	53
4.2.3 XPS analysis.....	53
4.3 Results and discussion.....	54
4.3.1 Disordered surface oxide.....	55
4.3.2 Surface oxide in 500 mbar O ₂	57
4.3.3 Low coverage needle oxide.....	59
4.3.4 Energetics of Au surface oxide.....	61
4.4 Conclusion.....	64
Supporting information.....	70
4.5 Reduction and surface alloying of WO ₃ at elevated temperature.....	71
4.6 X-ray beam induced desorption of surface oxides.....	72
4.7 Evolution of WO ₃ /Au(111) during pressure ramp to 500 mbar O ₂	73
4.8 Influence of the preparation conditions on the structure and coverage of the needle phase Au oxide.....	75
5 Simultaneous scanning tunneling microscopy and synchrotron X-ray measurements in a gas environment.....	77
5.1 Introduction.....	78
5.2 Instrument design.....	79
5.2.1 High-pressure cell.....	79
5.2.2 Coaxial tips and mounting scheme.....	80
5.2.3 Tip-beam alignment.....	83
5.2.4 Electronics scheme for separating the regular from the X-ray induced tunneling current.....	83
5.3 Performance.....	86
5.3.1 Current contributions from the gas environment.....	86
5.3.2 Background reduction using coaxial tips.....	88
5.3.3 Imaging.....	89
5.3.4 X-ray induced tunneling current enhancement.....	91
5.4 Conclusion and outlook.....	92
Summary and outlook.....	96
Samenvatting.....	99
Acknowledgments.....	103
List of publications.....	104
Curriculum Vitae.....	106

Chapter 1

Introduction

Whether it cures a disease, causes a colorful explosion in fireworks, or forms glittering crystals, chemistry has the power to amaze. Much of this amazement is caused by the seemingly incomprehensible relation between cause and effect when materials react. In 1727, the early days of chemical research, a frustrated Hermann Boerhaave noted [1]:

“For chemistry is no science form'd à priori; 'tis no production of the human mind, framed by reasoning and deduction: it took its rise from a number of experiments casually made, without any expectation of what follow'd; and was only reduced into an art or system, by collecting and comparing the effects of such unpremeditated experiments, and observing the uniform tendency thereof. So far, then, as a number of experimenters agree to establish any undoubted truth; so far they may be consider'd as constituting the theory of chemistry.”

Fortunately, the modern-day chemist can rely on extensive fundamental understanding to explain the how and why of chemical reactions. However, *predicting* chemistry is much more difficult than *explaining* it after the fact. In practice therefore, chemical research remains highly empirical. This is particularly true in the search for catalysts, compounds that accelerate a chemical reaction without being consumed (except for some slow degradation). To find new catalysts, chemical companies mostly use a brute-force approach, i.e. trial and error guided by the empirical trends from previous trial-and-error studies. While this approach has proven fruitful for optimizing the chemical processes that we employ today, the lack of fundamental understanding of catalyst behavior hampers the introduction of new chemistry.

Now that society is more and more aware of the effects that humanity has on the environment, there is a growing desire for a transition from fossil-oil-based chemistry to sustainable chemistry. Such a transition requires a complete makeover of the chemical industry, with many new industrial catalytic processes to be developed. The current empirical approach for finding catalysts may therefore no longer suffice. Hence, a vital next step in catalytic research is to increase our understanding from the point where we can give an explanation of catalysis to the point where we can formulate predictive guidelines.

1.1 Understanding a catalytic process

Any chemical reaction consists of one or more elementary bond breaking and/or bond making steps, which rearrange the way the atoms in the reactant molecules are bound to one another. Such a reaction can either consume or release energy. To calculate this change in reaction energy, we use the chemical potential of each molecule in the reaction, which describes its relative stability under the applied conditions of temperature and concentration at which molecules of the same species are present in the medium. Throughout this thesis, the chemical potential will be defined as:

$$\mu = E + E_{ZP} - ST + k_B T \ln(P) + C_P T \quad (1.1)$$

In equation 1.1, E is the electronic energy of the molecule at 0 K, E_{ZP} is the molecule's vibration energy at 0 K, k_B is Boltzmann's constant, T is the temperature, S is the entropy of the molecule, P is its (partial) pressure (for gases), and C_P is its heat capacity. With this definition, the chemical potential of a molecule is the energy gained from putting it together using electrons and ionic cores, and bringing it to a certain temperature and pressure. The change in Gibbs free energy accompanying the reaction $w A + x B \rightleftharpoons y C + z D$ is:

$$\Delta G_r = y\mu_C + z\mu_D - w\mu_A - x\mu_B \quad (1.2)$$

If this number is negative, the net forward reaction is thermodynamically favorable, meaning that at some point it will occur. It does, however, not tell us anything about the reaction kinetics. For example, the reaction of oxygen with the sugar, fat and protein of the human body to form CO_2 and H_2O is thermodynamically favorable, but fortunately extremely slow.

To go from one atomic arrangement to the other, the reactant molecules usually have to be distorted into an unfavorable configuration before new bonds can be formed. Such a distortion costs energy, thus creating a barrier for the reaction to occur (see Figure 1.1). In the simplest approximation and for a reaction consisting of one elementary step, the net reaction rate can be determined from the energy barrier and reaction energy by:

$$r = [A][B] \frac{k_B T}{h} e^{-\Delta G_a/k_B T} - [C][D] \frac{k_B T}{h} e^{-(\Delta G_a + \Delta G_r)/k_B T} \quad (1.3)$$

In equation 1.3, $[A]$, $[B]$, $[C]$, and $[D]$ are the concentrations or partial pressures of molecules A, B, C, and D, h is Planck's constant and ΔG_a is the activation barrier of the reaction. For many uncatalyzed reactions, ΔG_a is very large compared to $k_B T$, leading to very low reaction rates. A catalyst lowers the reaction barrier by providing a different reaction pathway (see Figure 1.1). Such a catalytic pathway typically consists of the molecules binding to the catalyst, dissociating, forming new bonds, and

desorbing from the catalyst (see Figure 1.1). For a good catalyst, the binding strength of the reactant and product molecules to the surface is balanced (Sabatier's principle)[2]. Strong binding makes it easy for the reactants to dissociate, but inhibits the desorption step. Weak binding, on the other hand, insufficiently aids the dissociation of the reactants.

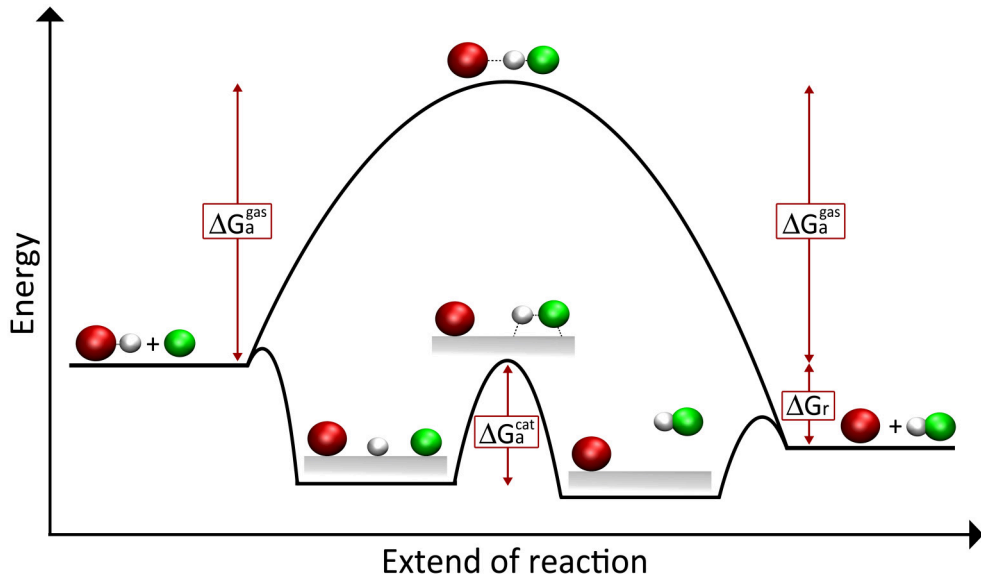


Figure 1.1: Illustration of the elementary steps in a chemical reaction. In the gas phase, a large free energy barrier needs to be overcome for the reaction to proceed. A catalyst offers an alternative pathway with lower energy barriers, thus speeding up the reaction.

In many cases, reactant molecules can bind to one another in several ways, yielding a variety of products. For example, a mixture of CO and H₂ can produce methane [3], methanol [4], ethanol [5], and alkanes [6]. To control which product is formed, catalysts are tuned to selectively accelerate the reaction forming only one product.

Most industrial catalytic processes are examples of heterogeneous catalysis: gaseous and/or liquid reactants interact with a solid catalyst. At the atomic level, the surface of the catalyst is very inhomogeneous. Most catalysts consist of nanoparticles fixed on a chemically robust oxide support such as Al₂O₃, SiO₂, or TiO₂ (see Figure 1.2). The nanoparticles provide a variety of surface sites to bind the reactant molecules, each with its own binding properties and hence catalytic activities. Even a simple, pure fcc metallic nanoparticle, with only (111) and (100) type facets, has 5 different atomic nearest-neighbor configurations, providing 12 different adsorption sites. The nanostructuring of the support and the use of additives and promoters increase this number drastically. Another addition to the complexity of catalysis is the fact that the reaction rate on all the different binding sites depends on the temperature and the concentration of reactants and products at the catalyst surface (see equation 1.3).

Hence, the mass and heat transport within the reactor also play a key role in the overall behavior of the process. These considerations show that it is far from trivial to couple cause and effect in catalytic research.

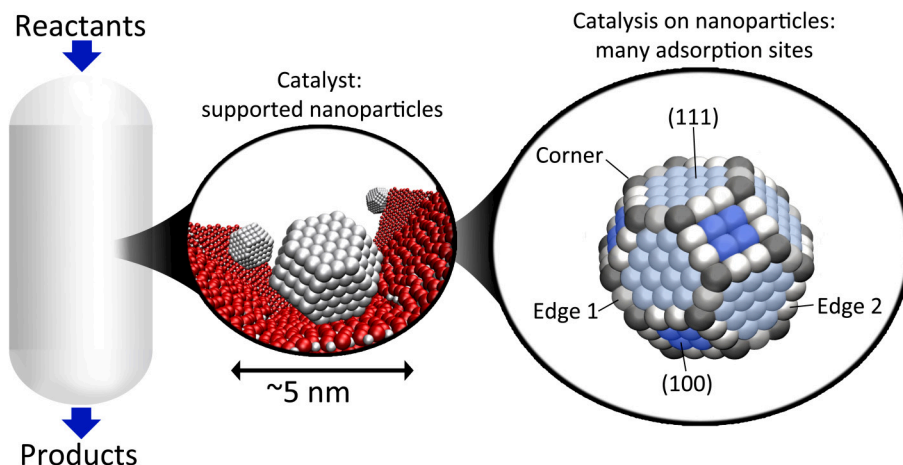


Figure 1.2: Essence of the structure of an industrial catalyst. The reactor is filled with a porous oxide material that supports the catalytic nanoparticles. The nanoparticles offer a variety of adsorption sites to which the reactants can bind. The structural complexity of the catalyst, together with its dynamic nature and the interplay with the mass and heat transfer in the reactor, make the relation between cause and effect extremely complex in catalysis.

1.2 The role of surface science

To disentangle the many factors that determine how well a catalyst works, one needs to be able to vary them independently, so that cause and effect are clear. For industrial catalysts, full control over the structural and chemical properties is not feasible, however. The surface science approach resolves this issue by using simplified model catalysts, in which some of the structural complexity is eliminated. The aim of surface-science experiments is to have a very high degree of control over all parameters in the experiment and to have complete understanding of the surface chemistry at the atomic level.

To allow for such control and understanding, surface science experiments are traditionally performed on polished single crystals that expose predominantly one or two atomic arrangements over their entire surface [7]. Furthermore, the gas environment is controlled by working in ultrahigh vacuum ($<10^{-6}$ mbar), so that only gases that are leaked into the system reach the sample surface. The additional advantage of the vacuum is that the surface can be studied using refined techniques

that rely on the interaction of electrons, ions, or atoms with the sample. The simple structure of the single-crystalline model catalyst allows for comparison to density functional theory (DFT) calculations, which describe the (electronic) structure and energetics of a limited number of atoms in great detail [8].

The bottom-up approach described above has allowed for a very good understanding of fundamental adsorption/desorption phenomena. If one is interested in the details of a specific catalytic process, however, single crystals in vacuum are too simplified to be representative of industrial catalysis. Two main oversimplifications can be identified: the *materials gap* and the *pressure gap* [9]. The materials gap originates from the fact that the same type of adsorption site on a catalyst nanoparticle and a single crystal may have very different properties. The electronic structure of a supported nanoparticle deviates from that of bulk material because of its small size and the interaction with the catalyst support [10,11]. Furthermore, some types of adsorption sites that exist on a nanoparticle cannot be created on a single crystal. The pressure gap further complicates matters due to the fact that the shape and surface structure of nanoparticles can change at elevated pressures [12,13]. Such surface reconstructions require the combination of a high driving force for adsorption and sufficient atomic mobility, i.e. high temperature. This combination can often not be achieved in vacuum.

To reconcile the fundamental experiments with industry, the modern trend in surface science is to bridge the materials and pressure gaps step by step. For the materials gap, this is typically achieved by the deposition of nanoparticles on single-crystalline supports. Theoretical models follow this development, although the computational cost limits the particle size that can be handled [11–15]. The effects of elevated pressures and temperatures can be modeled by straightforward addition of entropy terms (see equation 1.1), or in more detail using microkinetic modeling [16,17]. From the experimental side, the main challenge to bridge the pressure gap is the development of instrumentation that allows characterization of the catalyst's structure while it is operating [9,18,19]. One could imagine performing measurements in vacuum before and after using the catalyst. However, many of the reconstructions occurring on catalysts are reversible and will therefore not be visible in such measurements [9]. Hence, to gain proper understanding of how a catalyst works, *operando* structural and chemical characterization of well-defined nanoparticle model catalysts is essential.

1.3 In this thesis

In my PhD work, I have studied aspects of both the materials and the pressure gap using scanning tunneling microscopy (STM). This technique relies on measuring the tunneling current between the (conductive) sample surface and a sharp metal wire (the STM tip). The current decays from short circuit when tip and sample make

physical contact, to practically zero at a tip-sample distance of roughly 1 nm. Hence, the tunneling current can be used to track the morphology of the sample surface with atomic precision. A detailed treatment of STM can be found in Ref. [20].

Although STM is primarily used to study flat substrates, it can also be employed to characterize supported nanoparticles. In Chapter 2, I have used the combination of STM and X-ray photoelectron spectroscopy to investigate the nucleation and growth of MoO_x on Al₂O₃/NiAl(110). The aim of this study is to find handles for controlled preparation of complex model catalysts. Most work on such models has been performed on pure metallic nanoparticles [21–24]. From these studies, a clear picture has emerged of how the metal-support interaction influences the nucleation process. In Chapter 2, I extend this type of analysis to metal oxide particles.

Using a special scanning tunneling microscope, the ReactorSTM [25], I have performed measurements under high-temperature, high-pressure conditions. In Chapter 3, I discuss the structure of MoS₂ nanoparticles on Au(111) during the industrially important hydrodesulfurization reaction, in which sulfur is removed from organic molecules:



Zooming in on the atomic level detail of catalysts during this reaction, I investigate how the structure of the MoS₂ particles depends on the partial pressures of the reactants/products. A comparison to DFT calculations shows to what extent the reaction kinetics affect the MoS₂ structure.

In Chapter 4, I study the formation of Au surface oxides on WO₃/Au(111) and ReO₃/Au(111) inverse model catalysts. Such oxides could be important reaction intermediates on Au-based oxidation catalysts, but their existence under reaction conditions is questioned. Using the temperature dependence of the Au oxide coverage, I show that Au oxides are thermodynamically favored over a wide range of conditions.

In the last Chapter of this thesis, I discuss how one can increase the information depth from high-pressure STM by combining it with X-ray absorption spectroscopy (XAS). In a proof-of-principle study, I show that our integrated STM-XAS set-up is able to measure the X-ray-induced changes in the tunneling current, which opens the way to obtaining local chemical information with nanometer spatial resolution.

References

- [1] H. Boerhaave, *A New Method of Chemistry*, 1727.
- [2] O. Deutschmann, H. Knözinger, K. Kochloefl, T. Turek, *Heterogeneous Catalysis and Solid Catalysts*. Ullmann's Encyclopedia of Industrial Chemistry., Wiley-VCH, Weinheim, 2009.
- [3] M.P. Andersson, F. Abild-Pedersen, I.N. Remediakis, T. Bligaard, G. Jones, J. Engbæk, O. Lytken, S. Horch, J.H. Nielsen, J. Sehested, J.R. Rostrup-Nielsen, J.K. Nørskov, I. Chorkendorff, Structure sensitivity of the methanation reaction: H₂-induced CO dissociation on nickel surfaces, *J. Catal.* 255 (2008) 6–19.
- [4] M. Behrens, F. Studt, I. Kasatkin, S. Kühn, M. Hävecker, F. Abild-pedersen, S. Zander, F. Girgsdies, P. Kurr, B. Kniep, M. Tovar, R.W. Fischer, J.K. Nørskov, R. Schlögl, The Active Site of Methanol Synthesis over Cu/ZnO/Al₂O₃ Industrial Catalysts, *Science* 336 (2012) 893–898.
- [5] J.J. Spivey, A. Egbebi, Heterogeneous catalytic synthesis of ethanol from biomass-derived syngas, *Chem. Soc. Rev.* 36 (2007) 1514.
- [6] A.Y. Khodakov, W. Chu, P. Fongarland, Advances in the development of novel cobalt Fischer-Tropsch catalysts for synthesis of long-chain hydrocarbons and clean fuels, *Chem. Rev.* 107 (2007) 1692–1744.
- [7] H. Ibach, *Physics of Surfaces and Interfaces*, Springer, Berlin, 2006.
- [8] O. Deutschmann, *Modeling and Simulation of Heterogeneous Catalytic Reactions: From the Molecular Process to the Technical System*, Wiley-VCH, Weinheim, 2011.
- [9] J. W.M. Frenken, I.M.N. Groot, *Operando Studies in Heterogeneous Catalysis*, Springer, Heidelberg, 2016.
- [10] E. Roduner, Size matters: why nanomaterials are different, *Chem. Soc. Rev.* 35 (2006) 583–592.
- [11] E.D. Hermes, G.R. Jenness, J.R. Schmidt, Decoupling the electronic, geometric and interfacial contributions to support effects in heterogeneous catalysis, *Mol. Simul.* 41 (2015) 123–133.
- [12] B. Zhu, Z. Xu, C. Wang, Y. Gao, Shape Evolution of Metal Nanoparticles in Water Vapor Environment, *Nano Lett.* 16 (2016) 2628–2632.
- [13] M.A. Newton, Dynamic adsorbate/reaction induced structural change of supported metal nanoparticles: heterogeneous catalysis and beyond, *Chem. Soc. Rev.* 37 (2008) 2644–2657.
- [14] R.M. Anderson, D.F. Yancey, L. Zhang, S.T. Chill, G. Henkelman, R.M. Crooks, A theoretical and experimental approach for correlating nanoparticle structure and electrocatalytic activity, *Acc. Chem. Res.* 48 (2015) 1351–1357.
- [15] B.C. Han, C.R. Miranda, G. Ceder, Effect of particle size and surface structure on adsorption of O and OH on platinum nanoparticles: A first-principles study, *Phys. Rev. B.* 77 (2008) 075410.
- [16] J.K. Nørskov, M. Scheffler, H. Toulhoat, Density Functional Theory in Surface Science and Heterogeneous Catalysis Modeling, *MRS Bull.* 31 (2006) 669–674.
- [17] K. Reuter, M. Scheffler, First-principles kinetic Monte Carlo simulations for heterogeneous catalysis: Application to the CO oxidation at RuO₂(110), *Phys. Rev. B.* 73 (2006) 045433.
- [18] M. Salmeron, R. Schlögl, Ambient pressure photoelectron spectroscopy: A new tool for surface science and nanotechnology, *Surf. Sci. Rep.* 63 (2008) 169–199.
- [19] F.D. Ogletree, H. Bluhm, E.D. Hebenstreit, M. Salmeron, Photoelectron spectroscopy under ambient pressure and temperature conditions, *Nucl. Instruments Methods Phys.*

- Res. Sect. A Accel. Spectrometers, Detect. Assoc. Equip. 601 (2009) 151–160.
- [20] C.J. Chen, *Introduction to Scanning Tunneling Microscopy*, Oxford University Press, New York, 1993.
- [21] M. Bäumer, M. Frank, M. Heemeier, R. Kühnemuth, S. Stempel, H.-J. Freund, Nucleation and growth of transition metals on a thin alumina film, *Surf. Sci.* 456 (2000) 957–962.
- [22] M. Bäumer, H.-J. Freund, Metal deposits on well-ordered oxide films, *Prog. Surf. Sci.* 61 (1999) 127–198.
- [23] R.P. Galhenage, H. Yan, S.A. Tenney, N. Park, G. Henkelman, P. Albrecht, D.R. Mullins, D.A. Chen, Understanding the Nucleation and Growth of Metals on TiO₂: Co Compared to Au, Ni, and Pt, *J. Phys. Chem. C.* 117 (2013) 7191–7201.
- [24] C.T. Campbell, Ultrathin metal films and particles on oxide surfaces: structural, electronic and chemisorptive properties, *Surf. Sci. Rep.* 27 (1997) 1–111.
- [25] C.T. Herbschleb, P.C. van der Tuijn, S.B. Roobol, V. Navarro, J.W. Bakker, Q. Liu, D. Stoltz, M.E. Cañas-Ventura, G. Verdoes, M.A. van Spronsen, M. Bergman, L. Crama, I. Taminiu, A. Ofitserov, G.J.C. van Baarle, J.W.M. Frenken, The ReactorSTM: atomically resolved scanning tunneling microscopy under high-pressure, high-temperature catalytic reaction conditions., *Rev. Sci. Instrum.* 85 (2014) 083703.

Chapter 2

Tuning the properties of molybdenum oxide on $\text{Al}_2\text{O}_3/\text{NiAl}(110)$: metal versus oxide deposition

Model metal oxide nanoparticle catalysts are usually either prepared by the deposition of metal oxide or by deposition of metal in an O_2 background. From the example of MoO_x on $\text{Al}_2\text{O}_3/\text{NiAl}(110)$, we find that this choice can have profound consequences for the structure of the resulting catalyst. We interpret our findings in terms of the interaction between the deposited material and the support, which is stronger for MoO_x than for Mo. The observed difference between the two preparation methods suggests that the Mo atoms are oxidized typically only after having attached to a stable Mo or MoO_x nucleus.

Published as:

Tuning the Properties of Molybdenum Oxide on $\text{Al}_2\text{O}_3/\text{NiAl}(110)$: Metal Versus Oxide Deposition

R.V. Mom, M.J. Rost, J.W.M. Frenken, I.M.N. Groot,
Journal of Physical Chemistry C 120 (2016), 19737-19743

2.1 Introduction

Mixed metal oxide catalysts are commonly used in the chemical industry for a wide range of oxidation, reduction and isomerization reactions [1]. Due to their flexible bonding behavior and variable oxidation state, the rational design of such catalysts remains extremely challenging. The bottom-up approach of surface science allows one to disentangle the multitude of effects that play a role in metal oxide catalysis.

Well-defined model catalysts are typically prepared in ultrahigh vacuum (UHV) by physical vapor deposition of the active phase onto flat oxide single crystals [2–9] or onto thin oxide films supported on single crystals [10–14]. For mixed metal oxide catalysts, the most common procedure is the deposition of metal using electron-beam evaporation in an oxygen background. Metal oxides that are volatile at elevated temperature may also be evaporated directly onto the support, either from an oxide powder source [3] or from an oxidized metal rod or wire[2].

The formation of the catalyst using the methods mentioned above usually starts with some form of nucleation and particle growth of the deposited material. There are several parameters that affect the nucleation process [15,16], such as the deposition flux, the substrate temperature and the interactions between the deposited material and the support. These provide handles to tune the model catalyst properties. For supported metal clusters and nanoparticles, these parameters have been studied extensively both theoretically [15,16] and experimentally [5,17,18]. It was shown that a high flux and a strong metal-support interaction result in the formation of a high density of small particles, while the combination of a low flux and a high temperature yields fewer, yet larger particles. As, in general, the surface energy of metals is higher than oxides, metals usually form three-dimensional particles on oxide surfaces (Volmer-Weber type growth) [18,19]

The nucleation and growth stage of mixed metal oxide catalysts is much less studied and shows much larger variation. In some cases, Volmer-Weber type growth is observed, such as for VO_x [12] and NbO_x [14] on $\text{Al}_2\text{O}_3/\text{NiAl}(110)$. In other cases, particles grow in two-dimensional islands [2], or they do not agglomerate beyond oligomeric clusters [3,6]. Hence, particle sizes and densities may vary strongly, even for similar deposition fluxes and temperatures, depending on the precise choices of the supporting and the active phase oxides. Despite the differences in the nucleation behavior of supported metals and oxides, the general aspects of the nucleation theories developed for metals should also apply to oxides, particularly when nucleation leads to sufficiently large particles to satisfy the capillary approximation [20].

An aspect that has no analogue in the simple case of supported metals is the possibility to deposit different starting materials for making the same metal-support combination. Indeed, mixed metal oxide catalysts can be prepared from deposited metal atoms but also from monomeric or even oligomeric oxide clusters. The large

differences between these precursor materials may provide interesting opportunities to tune the properties of the resulting catalyst.

Here, we use X-ray photoelectron spectroscopy (XPS) and scanning tunneling microscopy (STM) to study the effect of the choice of deposited material on the dispersion of MoO_x on $\text{Al}_2\text{O}_3/\text{NiAl}(110)$. We have prepared model catalysts both through the evaporation of MoO_x and through the deposition of metallic Mo in an O_2 environment. The resulting catalysts are compared to structures observed after the deposition of metallic Mo on $\text{Al}_2\text{O}_3/\text{NiAl}(110)$. We find that MoO_x prepared via Mo deposition reflects the nucleation behavior of metallic Mo. The observations are discussed in terms of nucleation theory and the timing of the oxidation of deposited Mo atoms.

2.2 Methods

All experiments were carried out in a home-built UHV apparatus described in detail elsewhere [21]. The system is equipped with a commercial photoelectron spectrometer (SPECS Phoibos), a commercial e-beam evaporator (Oxford Applied Research), standard sample preparation equipment and a scanning tunneling microscope.

2.2.1 XPS analysis

All XPS experiments were carried out with the X-ray incidence angle at 54° off normal and electron collection along the surface normal. Peak fitting was performed using the Gaussian/Lorentzian curves implemented in the CasaXPS [22] software package. For fitting of the Mo 3d spectra, peak positions were constrained to within 0.1 eV around literature values [23] for Mo^{6+} , Mo^{5+} , Mo^{4+} and Mo^0 . All peak widths (FWHM) were constrained to be equal. The spin-orbit-split peak pairs were forced to obey a 3:2 peak area ratio. Fitting of the Ni 3p /Al 2p area was performed using one doublet for the Ni signal and two for Al (Al^0 , Al^{3+}). Again doublets were constrained in area (2:1) and FWHM.

2.2.2 Sample preparation

The NiAl(110) sample (Surface Preparation Laboratory [24]) was cleaned by cycles of 1.5 keV Ar^+ bombardment and annealing at 1300 K. Growth of the alumina film was accomplished through three cycles of oxidation at 550 K in a 5×10^{-6} mbar O_2 background (1×10^{-6} mbar O_2 in the last cycle) and subsequent UHV annealing at 1100 K (1050 K in the last cycle) [25]. The cleanliness of the film was checked by XPS and STM.

The $\text{MoO}_x/\text{Al}_2\text{O}_3/\text{NiAl}(110)$ catalysts were prepared using an electron-beam evaporator. All depositions were carried out with the $\text{Al}_2\text{O}_3/\text{NiAl}(110)$ support at room temperature. When depositing MoO_x , the Mo evaporator rod temperature was set at approximately 1200 K (as determined from the color of the rod), and an O_2 background of 5×10^{-6} mbar was applied. Under these circumstances, volatile MoO_x species are generated on the rod [2]. The mild rod temperature ensures that no metallic Mo evaporates ($P_{\text{vap}} = 1.6 \times 10^{-18}$ mbar [26]). Due to the relatively mild oxygen background, we do not expect the formation of oligomeric $(\text{MoO}_3)_n$ clusters, which are the predominant gas phase species when MoO_3 powder is evaporated [27]. We confirmed this by performing a deposition experiment on $\text{Au}(111)$, which shows less on-surface oxidation. We observe predominantly Mo^{4+} and Mo^{5+} in XPS. As the formation of oligomeric $(\text{MoO}_3)_n$ requires a high surface concentration of Mo^{6+} species on the evaporation rod, we can conclude that this process is unlikely.

For the preparation using Mo as the deposited material, the rod temperature was set at approximately 2000 K in an O_2 background of 5×10^{-7} mbar. Under these conditions, the net oxygen coverage on the rod will be low, while the flux of subliming Mo is high. Hence, Mo should be deposited predominantly in metallic form and become oxidized only after arrival on the $\text{Al}_2\text{O}_3/\text{NiAl}(110)$ support.

2.2.3 Particle statistics

Statistics on the number density, height and size of the particles were obtained using the Gwyddion software package[28]. The package offers a variety of particle recognition methods, which were crosschecked against each other to ensure robustness of the results with respect to the specific procedure applied. Furthermore, errors found in the automated particle recognition were corrected by hand. Using the “Watershed” algorithm, apparent agglomerates were separated into the individual particles. For the statistical analysis, only image segments without steps in the substrate were used.

A combination of STM and XPS results was used to determine the Mo coverage on the sample. The Mo 3d/(Al 2p + Ni 3p) ratio was determined from the XPS spectra for all samples. Using a series of experiments where metallic Mo was sequentially deposited on the support, we established a linear relation between the Mo 3d/(Al 2p + Ni 3p) ratio and the coverage obtained from the STM images. To obtain the Mo coverage from an STM image, we calculated the total volume of the particles in the image, with thresholding as the particle detection method. Because STM overestimates the particle height of metallic particles on $\text{Al}_2\text{O}_3/\text{NiAl}(110)$ by approximately 0.3 nm at the sample bias used in this work (-2 V) [13], the recognition threshold was set at this value and the volume was calculated with respect to the horizontal plane defined by the threshold. STM also overestimates the lateral dimensions of the particles. Based on simple geometrical models, one can establish that this results in a volume overestimation between 2.1x and 17x for the particle sizes investigated here (see supporting information). Assuming the tip radius to be of similar size as the particles,

we have divided the total volume obtained by the thresholding method by 4. After calibration of the XPS Mo 3d/(Al 2p+Ni 3p) ratio versus the STM coverage, a coverage estimate could also be obtained for the MoO_x samples. All coverages are expressed in monolayers of the Mo(110) surface (1 ML corresponds to 1.43x10¹⁵ Mo atoms cm⁻²).

2.3 Model for nucleation on Al₂O₃/NiAl(110)

In contrast to standard nucleation theory, nucleation is strongly heterogeneous for metal clusters on Al₂O₃/NiAl(110). It is governed by three types of nucleation sites [17]: the steps, domain boundaries and point defects of the alumina film. The first two are found to be energetically preferred over the latter. However, depending on the deposition parameters and the nature of the deposited material, atoms can become trapped at the point defects before reaching the domain boundaries or steps. When deposition is performed at low sample temperatures or in case of strong deposition material-support interaction, nucleation may even occur almost exclusively at point defects[10,17]. Hence, understanding of the nucleation at point defects is key to understanding the overall nucleation behavior on Al₂O₃/NiAl(110).

A rate equation model for point defect nucleation, showing excellent agreement with experimental data, was put forward by Venables and Harding [15]. For mild sample temperatures and pure point defect nucleation, the only important factor is the average occupation of the defect sites by monomers. At very low temperatures, even a single atom is stably bound at a defect site on the timescale relevant to nucleation. In this regime, the particle density is fully determined by the point defect density and will, therefore, be independent of the deposition flux and the nature of the deposited material[17,18]. For metal particles at room temperature, a dimer is usually the smallest stable cluster at point defects on oxide supports [15]. Hence, monomers hop on and off the point defects, leading to not continuously occupied sites. Therefore, it is possible to pass them and move on to other nucleation sites (steps and domain boundaries). The fraction of point defects that is covered in this regime increases with increasing deposition flux and increasing trapping energy. The latter is the energy gained by adsorption of a deposited monomer at a point defect with respect to a regular terrace site. An increase in diffusion rate will lower the fraction of occupied point defects.

Both the diffusion rate and the trapping energy can be expected to depend on the interaction strength between the deposited material and the support. Hence, the interaction strength may be a useful parameter to understand trends as a function of the choice of deposited material. For metals, the heat of formation of the highest metal oxide is often used as an indicator for metal-support interactions. Indeed, the average particle size and the particle density of metals deposited on Al₂O₃/NiAl(110)[17] were found to correlate with that energy.

An important factor in the description above is the point defect density, for which an STM or XPS characterization is unfortunately not available. However, electron paramagnetic resonance [18] and cathodoluminescence [29] experiments have proven their existence, and comparative nucleation studies have estimated their density to be in the order of $1 \times 10^{13} \text{ cm}^{-2}$ [30]. It was not established directly whether this value is reproducible, yet from the trend observed for different metals on $\text{Al}_2\text{O}_3/\text{NiAl}(110)$ produced in various labs [13,17,18,31], we infer that the point defect density must be reproduced quite well. We rationalize this observation by the fact that the point defects in $\text{Al}_2\text{O}_3/\text{NiAl}(110)$ originate from imperfections in the crystallinity of the alumina film, and not from loss of oxygen during annealing, such as in the case of $\text{TiO}_2(110)$ [32].

2.4 Results and discussion

With the description from Section 2.3 in mind, we will analyze the dispersion of MoO_x and Mo particles on $\text{Al}_2\text{O}_3/\text{NiAl}(110)$, prepared via the two different routes described in Section 2.2.

2.4.1 Nucleation of metallic Mo and MoO_x

In order to establish the nucleation characteristics of Mo atoms and MoO_x species, a series of experiments was conducted in which various amounts of Mo (without O_2 background) and MoO_x (via MoO_x deposition) were deposited onto the $\text{Al}_2\text{O}_3/\text{NiAl}(110)$ support. Figure 2.1 compares the results of both procedures through two STM images. It is clear that even at the qualitative level there are profound differences.

Metallic Mo, like most metals on $\text{Al}_2\text{O}_3/\text{NiAl}(110)$, strongly decorates the step edges. Furthermore, lines of particles are visible on the terraces, indicating that the domain boundaries are also decorated. However, this effect is not as pronounced as for other metals such as Pd and Rh [13,17,18,31]. The clear decoration of steps and domain boundaries shows that the average occupation of the point defects was low during the deposition, indicating a mild interaction between the deposited material and the support. Still, the interaction is stronger than for many other metals, such as Pd, Rh and Cu [13,17,18,31], as can be expected from the comparatively high heat of formation of MoO_3 [33].

The MoO_x particles have an entirely different dispersion. They show no clear preference for steps or domain boundaries. This is similar to VO_x [12] and NbO_x [14] on $\text{Al}_2\text{O}_3/\text{NiAl}(110)$, and to metals on this substrate when deposited at 90 K [17]. The lack of step edge/domain boundary decoration indicates that the interaction of MoO_x with the $\text{Al}_2\text{O}_3/\text{NiAl}(110)$ support is much stronger than that of metallic Mo. Mo^{6+} is the dominant oxidation state found for the MoO_x particles (see Supporting

Information). This is a higher oxidation state than the Mo^{4+} and Mo^{5+} that is deposited under these conditions (see Section 2.2), which can be taken as evidence for strong on-surface oxidation during the deposition. Note that the deposition flux was larger for Mo than for MoO_x . Hence, the intrinsic differences between the nucleation behavior of Mo and MoO_x may be even larger than those observed here.

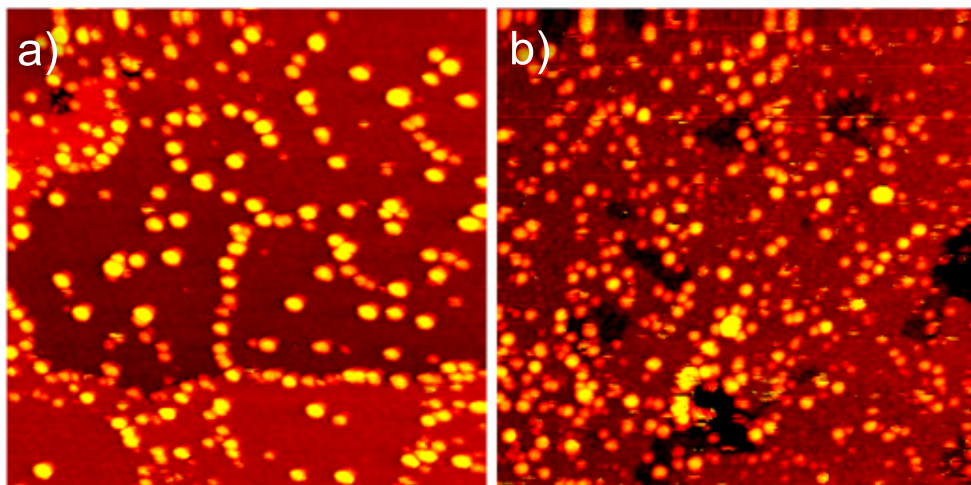


Figure 2.1: STM images of a) 0.069 ML metallic Mo, deposited at 1.1×10^{-2} ML/min, and b) 0.073 ML MoO_x , deposited at 1.5×10^{-3} ML/min. Size: 80 nm x 80 nm, sample bias -2 V and tunneling current 50 pA.

Figure 2.2 shows the observed particle height distributions for metallic Mo and MoO_x , and their dependence on the Mo coverage. Note that the observed height will in both cases deviate from the actual topographic height, since STM probes the local density of states rather than atomic positions. The alumina film has a semiconducting character. When measuring on the terrace at mild sample voltage, the tunneling electrons originate from the metallic NiAl(110) rather than from the alumina film [13,18]. For this reason, the particle height of metal particles on $\text{Al}_2\text{O}_3/\text{NiAl}(110)$ is overestimated when a bias voltage within the band gap of the alumina film is used. At -2 V, this overestimation is approximately 0.3 nm [13].

The data of metallic molybdenum clearly evidence Volmer-Weber type growth also observed for other metals on $\text{Al}_2\text{O}_3/\text{NiAl}(110)$ [10,13,17]. The comparatively low particle height fits well with the relatively strong Mo-alumina interaction expected based on the high heat of formation of MoO_3 [33]. Notice that if one would correct for the overestimation of the height, some of the particles are located inside the oxide film. This is likely related to oxidation of some of the very small particles. When sufficiently oxidized, MoO_x particles typically display a bandgap³⁴. This may decrease their observed height. Indeed, the XPS spectra indicate a small amount of oxidized Mo (see Supporting Information). This oxidation could result from either transfer of

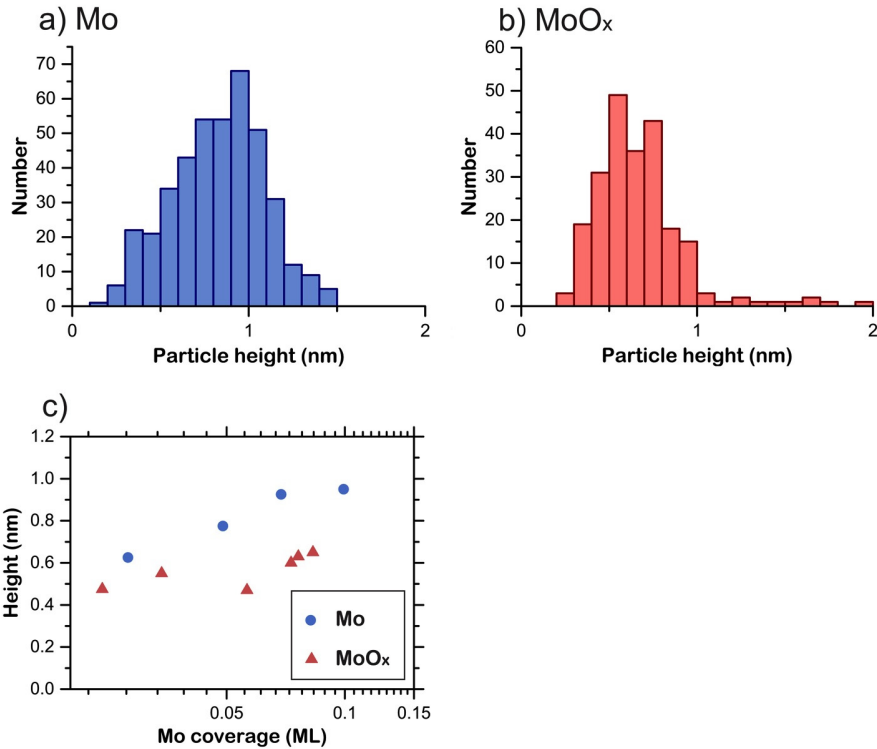


Figure 2.2: Particle height data of 0.069 ML Mo (deposited at 1.1×10^{-2} ML/min) and 0.076 ML MoO_x (deposited at 1.5×10^{-3} ML/min) from STM images recorded at -2 V. a,b) Observed height distributions, c) Peak positions of the height distributions as a function of coverage

electron density to the oxygen atoms of the alumina film, or from oxidation by the residual gas background in the UHV system.

When interpreting the data from the MoO_x deposition in Figure 2.2b, one has to take into account that both the alumina film and the MoO_x particles themselves have a semiconducting character [34]. The true particle height is therefore not immediately clear. Indeed, when decreasing the sample bias to -1V, many particles ‘disappear’ from the STM image. Nonetheless, the height information can be used to establish the growth mode of MoO_x. The width of the height distribution in Figure 2.2b can either be caused by particles of varying height, or by particles bound in different ways to the support, resulting in different semiconducting character. If the latter were correct, one may expect that the observed particle height decreases with increasing coverage. The reason for this is that the band gap of MoO_x typically increases when its coordination number increases [34]. This can be expected to occur when the particles grow. From Figure 2.2c it is clear that the observed particle height increases rather than decreases. Hence, MoO_x also shows Volmer-Weber growth.

Based on literature ^{13,35-37}, we expect that no mixing occurs between the MoO_x particles and the alumina film. First, MoO_x/alumina catalysts are often heated in the chemical industry, but the formation of mixed Mo-alumina oxides is not observed ³⁵. Second, Al₂O₃/NiAl(110) appears less prone to the formation of mixed oxides than other forms of alumina. Cobalt aluminates are commonly observed in the chemical industry ³⁵, but no compound formation was observed upon Co deposition on Al₂O₃/NiAl(110) ^{13,36}, even at elevated temperatures and in an oxygen environment. Similarly, a theoretical study on vanadia deposition on Al₂O₃/NiAl(110) concluded that extreme conditions would be required for mixing reactions to occur ³⁷.

In Figure 2.3a, the particle density of metallic Mo and MoO_x is depicted as a function of Mo coverage. The higher slope of MoO_x can be explained by its stronger support interaction. Such increased support interaction leads to a higher monomer occupation of the point defects in the film, thus increasing the odds of forming a new nucleus with respect to attaching to a pre-existing one. Again, the observed differences between metallic and oxidic Mo may be decreased by the higher flux used for metallic Mo.

Figure 2.3b shows literature data of nucleation studies with V [10], VO_x [12] and NbO_x [14] on Al₂O₃/NiAl(110). For easy comparison to literature, we have chosen to express all coverages in terms of monolayers of each metal's (110) plane. The densities of atoms per cm² can be obtained simply by multiplying the coverages by the atomic densities of the corresponding (110) surfaces (1.43x10¹⁵ cm⁻² for Mo(110), 1.54x10¹⁵ cm⁻² for V(110) and 1.84x10¹⁵ cm⁻² for Nb(110)).

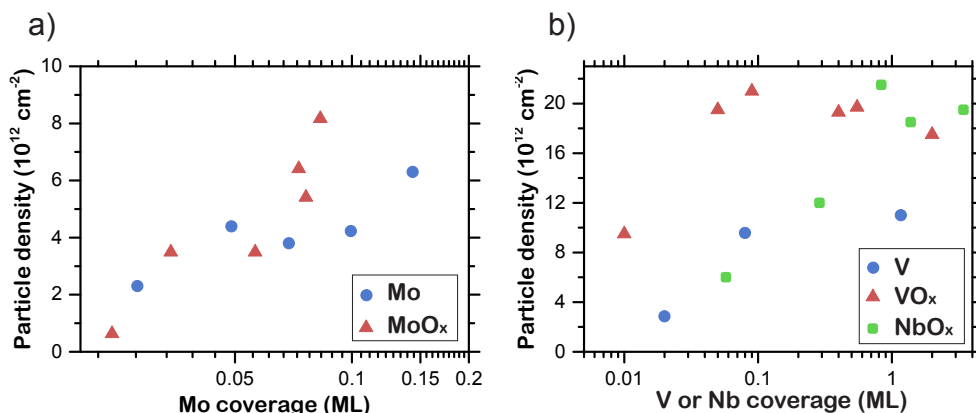


Figure 2.3: Coverage dependence of the particle density. a) Metallic Mo deposited at 1.1×10^{-2} to 1.5×10^{-2} ML/min and MoO_x deposited at 1.0×10^{-3} to 1.5×10^{-3} ML/min. b) Literature data for metallic V deposited at ± 0.35 ML/min [10], VO_x deposited at 0.36 ML/min [12] and NbO_x deposited at 2.8×10^{-2} ML/min [14]. All coverages are expressed in terms of the metal's (110) plane. All depositions were performed with the sample at room temperature.

When comparing to VO_x, MoO_x has a lower particle density, which leads to the conclusion that the support-MoO_x interaction is not strong enough to create a full

coverage of MoO_x monomers on the point defects during deposition. This means that the nucleation density of MoO_x will be deposition flux dependent at room temperature. As the flux in our experiments was roughly two orders of magnitude lower than in the case of VO_x, the observed differences in nucleation density may be larger than in the case of equal flux. NbO_x, which was deposited roughly one order of magnitude faster than MoO_x, behaves similar to MoO_x. One can therefore expect that the MoO_x density on pristine Al₂O₃/NiAl(110) should reach a plateau value at 2x10¹³ per cm², similar to the cases of NbO_x and VO_x. Due to particle-catalyzed film growth during O₂ exposure, which was also observed for other metals^{12,14,36}, we could not obtain data of sufficient quality at higher coverages to establish this.

Note that the plateau value of 2x10¹³ nuclei per cm² is higher than the literature value of 1x10¹³ point defects per cm². This could be explained either by the existence of point defects of a type that has thus far not been probed, or by partial homogeneous nucleation. Since VO_x and NbO_x reach the same plateau level, it can be expected that the former is the more likely explanation.

2.4.2 Preparation of MoO_x via Mo

Based on the understanding of the nucleation properties of Mo and MoO_x, we can study the dispersion of MoO_x prepared via deposition of metallic Mo in an O₂ background (on-surface oxidation). Figure 2.4 shows the result of this procedure at a coverage of 0.21ML. Clearly, the step edges are strongly decorated, similar to the case of Mo nucleation in the absence of an O₂ background. Notice also, particularly in the top-right side of the image, that lines of particles are visible on the terraces, indicating decoration of the domain boundaries. Again, this strongly resembles the behavior of metallic Mo.

The resemblance between the nucleation behavior of metallic Mo and MoO_x prepared via metallic Mo also extends to the particle density. At 0.21 ML, we found a density of 6.9x10¹² per cm², which clearly fits in the trend of metallic Mo, but is roughly half of the value expected for MoO_x nucleation.

The observations above can be explained by the timing of the on-surface oxidation of molybdenum. When the newly arrived Mo atoms become oxidized only after diffusing over the surface and attaching to a stable nucleus, their nucleation behavior will reflect that of metallic Mo atoms. Indeed, the XPS spectra show that MoO_x particles prepared via Mo are less strongly oxidized than those prepared via MoO_x evaporation (see supporting information), thus showing that the process of Mo oxidation is kinetically hindered at room temperature. When 0.10 ML of metallic Mo is deposited onto the substrate without O₂ background and subsequently exposed to oxygen, very little oxidation occurs. Therefore, oxidation and particle growth must occur hand in hand. Each newly arriving Mo atom is oxidized before its number of Mo neighbors increases to such an extent that oxidation becomes kinetically inhibited.

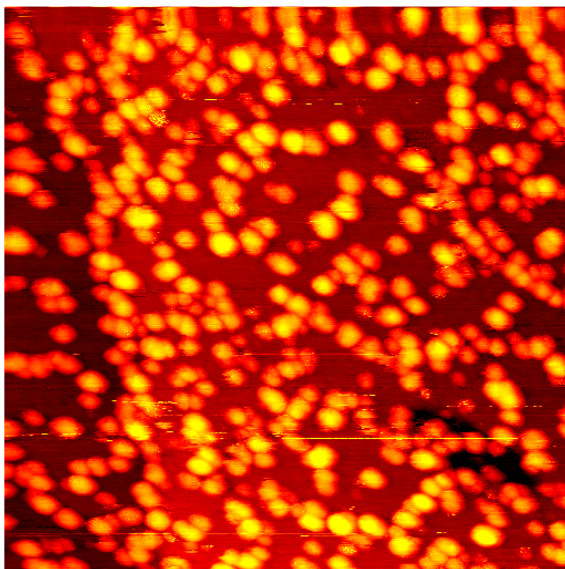


Figure 2.4: STM image of 0.21 ML MoO_x prepared by deposition of metallic Mo at 1.2×10^{-2} ML/min in 5×10^{-7} mbar O_2 . Size: 80 nm x 80 nm, sample bias -2 V, tunneling current 50 pA

It should be noted at this point that the VO_x [12] and NbO_x [14] catalysts we have been comparing to were prepared by depositing metallic V and Nb in an oxygen background. The vanadium data (see Figure 2.3b) show a clear difference in the nucleation behavior of metal [10] and oxide, hence the vanadium atoms arriving on the surface in an O_2 background were oxidized before attaching to a stable nucleus. The difference in the behavior of Mo and V can be explained by the higher reactivity towards oxygen of vanadium [33]. This results in a slower diffusion of vanadium on the support, and possibly also in a higher sticking probability of oxygen. The higher particle density of metallic vanadium versus metallic molybdenum (see Figure 2.3) indeed seems to support such slower diffusion, but the difference in deposition flux makes it inappropriate to compare these observations fully quantitatively.

Our results show that the timing of the oxidation during metal oxide particle growth has a large influence on the resulting model catalyst. The origin of this is that isolated metal oxide units often have a very different interaction with the support than metal atoms. In the case of Mo, the interaction is clearly stronger for the oxide units than for the metal atoms. In order to obtain small particles, one therefore should choose to deposit MoO_x directly onto the support. For large particles, one should rather deposit metallic Mo in an oxygen background. Although not explored here, changing the O_2 pressure should allow one to continuously change the ratio of metallic Mo atoms and isolated MoO_x units diffusing on the surface, thus providing a more continuous control over the particle size.

2.5 Conclusion

We have studied the nucleation behavior of metallic Mo and MoO_x prepared either via direct deposition of MoO_x or via deposition of metallic Mo in an O₂ background. We find that metallic molybdenum behaves similar to other reactive metals, showing three-dimensional particles nucleating at the oxide film's point defects as well as on its domain boundaries and steps. The average particle size and nucleation density fit well with the trends for other metals, based on their heat of highest oxide formation.

When MoO_x is prepared by direct deposition of in situ generated MoO_x, we find a much stronger support interaction than in the case of metallic Mo, resulting in a higher particle density and a domination of point defect nucleation. Nonetheless, we observe that the particles grow in a three-dimensional mode.

When MoO_x is prepared by deposition of metallic Mo in a 5×10^{-7} mbar O₂ background, the nucleation behavior clearly reflects the behavior of the metal rather than the oxide. This is explained by the timing of the oxidation of the molybdenum on the surface. It is found that the Mo atoms arriving on the surface are typically oxidized only after attaching to a stable nucleus.

We have thus established that the choice of evaporating material is a useful parameter to tune model mixed metal oxide catalyst properties. As an outlook, we may expect that changing the O₂ pressure should allow one to continuously change the ratio of metallic Mo atoms and isolated MoO_x units diffusing on the surface, thus providing a continuous control over the particle size.

References

- [1] J.L.G. Fierro, *Metal Oxides: Chemistry and Applications*, CRC Press, 2006.
- [2] C. Bamroongwongdee, M. Bowker, A.F. Carley, P.R. Davies, R.J. Davies, D. Edwards, *Fabrication of complex model oxide catalysts: Mo oxide supported on Fe₃O₄(111)*, *Faraday Discuss.* 162 (2013) 201–212.
- [3] O. Bondarchuk, X. Huang, J. Kim, B.D. Kay, L.-S. Wang, J.M. White, Z. Dohnálek, *Formation of monodisperse (WO₃)₃ clusters on TiO₂(110)*, *Angew. Chemie - Int. Ed.* 45 (2006) 4786–4789.
- [4] A. Desikusumastuti, M. Laurin, M. Happel, Z. Qin, S. Shaikhutdinov, J. Libuda, *Strong Size Effects in Supported Ionic Nanoparticles: Tailoring the Stability of NO_x Storage Catalysts*, *Catal. Letters.* 121 (2008) 311–318.
- [5] R.P. Galhenage, H. Yan, S.A. Tenney, N. Park, G. Henkelman, P. Albrecht, D.R. Mullins, D.A. Chen, *Understanding the Nucleation and Growth of Metals on TiO₂: Co Compared to Au, Ni, and Pt*, *J. Phys. Chem. C.* 117 (2013) 7191–7201.
- [6] O. Karşlıoğlu, X. Song, H. Kuhlenbeck, H. Freund, *Mo+TiO₂(110) Mixed Oxide Layer: Structure and Reactivity*, *Top. Catal.* 56 (2013) 1389–1403.
- [7] H.Y. Kim, H.M. Lee, R.G.S. Pala, H. Metiu, *Oxidative Dehydrogenation of Methanol to Formaldehyde by Isolated Vanadium, Molybdenum, and Chromium Oxide Clusters Supported on Rutile TiO₂(110)*, *J. Phys. Chem. C.* (2009) 16083–16093.
- [8] J.B. Park, J. Graciani, J. Evans, D. Stacchiola, S. Ma, P. Liu, A. Nambu, J.F. Sanz, J. Hrbek, J.A. Rodriguez, *High catalytic activity of Au/CeO_x/TiO₂(110) controlled by the nature of the mixed-metal oxide at the nanometer level*, *Proc. Natl. Acad. Sci. U. S. A.* 106 (2009) 4975–80.
- [9] J.A. Rodriguez, D. Stacchiola, *Catalysis and the nature of mixed-metal oxides at the nanometer level: special properties of MO_x/TiO₂(110) {M= V, W, Ce} surfaces*, *Phys. Chem. Chem. Phys.* 12 (2010) 9557–9565.
- [10] M. Bäumer, J. Biener, R.J. Madix, *Growth, electronic properties and reactivity of vanadium deposited onto a thin alumina film*, *Surf. Sci.* 432 (1999) 189–198.
- [11] A. Desikusumastuti, Z. Qin, T. Staudt, M. Happel, Y. Lykhach, M. Laurin, S. Shaikhutdinov, J. Libuda, *Controlling metal/oxide interactions in bifunctional nanostructured model catalysts: Pd and BaO on Al₂O₃/NiAl(110)*, *Surf. Sci.* 603 (2008) L9–L13.
- [12] N. Magg, J.B. Giorgi, T. Schroeder, M. Bäumer, H.-J. Freund, *Model catalyst studies on vanadia particles deposited onto a thin-film alumina support - 1. Structural characterization*, *J. Phys. Chem. B.* 106 (2002) 8756–8761.
- [13] E. Napetschnig, M. Schmid, P. Varga, *Pd, Co and Co-Pd clusters on the ordered alumina film on NiAl(110): Contact angle, surface structure and composition*, *Surf. Sci.* 601 (2007) 3233–3245.
- [14] A. Uhl, J. Sainio, J. Lahtinen, S. Shaikhutdinov, H.-J. Freund, *Preparation and structure of alumina supported niobia model catalysts*, *Surf. Sci.* 601 (2007) 5605–5610.
- [15] J.A. Venables, J.H. Harding, *Nucleation and Growth of Supported Metal Clusters at Defect Sites on oxide and halide(001) surfaces*, *J. Cryst. Growth.* 211 (2000) 27–33.

- [16] T. Michely, J. Krug, *Islands, Mounds and Atoms: Patterns and Processes in Crystal Growth Far from Equilibrium*, Springer, 2004.
- [17] M. Bäumer, M. Frank, M. Heemeier, R. Kühnemuth, S. Stempel, H.-J. Freund, Nucleation and growth of transition metals on a thin alumina film, *Surf. Sci.* 456 (2000) 957–962.
- [18] M. Bäumer, H.-J. Freund, Metal deposits on well-ordered oxide films, *Prog. Surf. Sci.* 61 (1999) 127–198.
- [19] J. V. Naidich, The Wettability of Solids by Liquid Metals, *Prog. Surf. Membr. Sci.* 14 (1981) 353–484.
- [20] J. Julin, I. Napari, J. Merikanto, H. Vehkamäki, A Thermodynamically Consistent Determination of Surface Tension of Small Lennard-Jones Clusters from Simulation and Theory, *J. Chem. Phys.* 133 (2010) 044704.
- [21] C.T. Herbschleb, P.C. van der Tuijn, S.B. Roobol, V. Navarro, J.W. Bakker, Q. Liu, D. Stoltz, M.E. Cañas-Ventura, G. Verdoes, M.A. van Spronsen, M. Bergman, L. Crama, I. Taminiau, A. Ofitserov, G.J.C. van Baarle, J.W.M. Frenken, The ReactorSTM: atomically resolved scanning tunneling microscopy under high-pressure, high-temperature catalytic reaction conditions., *Rev. Sci. Instrum.* 85 (2014) 083703.
- [22] N. Fairley, CasaXPS 2.3, (1999). www.casaxps.com.
- [23] P.A. Spevack, N.S. McIntyre, A Raman and XPS Investigation of supported molybdenum oxide thin films. 2. Reactions with Hydrogen Sulfide, *J. Phys. Chem.* 97 (1993) 11031–11036.
- [24] Surface Preparation Laboratory, (n.d.). www.spl.eu.
- [25] R.M. Jaeger, H. Kuhlenbeck, H. Freund, M. Wuttig, W. Hofmann, R. Franchy, H. Ibach, Formation of a well-ordered aluminium oxide overlayer by oxidation of NiAl (110), *Surf. Sci.* 259 (1991) 235–252.
- [26] C.B. Alcock, V.B. Itkin, M.K. Horrigan, Vapor-pressure equations for the metallic elements - 298-2500 K, *Can. Metall. Q.* 23 (1984) 309.
- [27] R. Rousseau, D.A. Dixon, B.D. Kay, Z. Dohnálek, Dehydration, dehydrogenation, and condensation of alcohols on supported oxide catalysts based on cyclic (WO₃)₃ and (MoO₃)₃ clusters, *Chem. Soc. Rev.* 43 (2014) 7664–7680.
- [28] D. Nečas, P. Klapetek, Gwyddion: an open-source software for SPM data analysis, *Cent. Eur. J. Phys.* 10 (2012) 181–188.
- [29] M. Adelt, S. Nepijko, W. Drachsel, H.-J. Freund, Size-dependent luminescence of small palladium particles, *Chem. Phys. Lett.* 291 (1998) 425–432.
- [30] M. Frank, M. Bäumer, From atoms to crystallites: adsorption on oxide-supported metal particles, *Phys. Chem. Chem. Phys.* 2 (2000) 3723–3737.
- [31] T. Worren, K. Højrup Hansen, E. Lægsgaard, F. Besenbacher, I. Stensgaard, Copper clusters on Al₂O₃/NiAl(110) studied with STM, *Surf. Sci.* 477 (2001) 8–16.
- [32] S. Wendt, R. Schaub, J. Matthesen, E.K. Vestergaard, E. Wahlström, M.D. Rasmussen, P. Thostrup, L.M. Molina, E. Lægsgaard, I. Stensgaard, B. Hammer, F. Besenbacher, Oxygen vacancies on TiO₂(1 1 0) and their interaction with H₂O and O₂: A combined high-resolution STM and DFT study, *Surf. Sci.* 598 (2005) 226–245.

- [33] M.W. Chase, NIST-JANAF tables 4th edition, NIST, 1998.
- [34] L. Mosqueira, S.A. Gómez, G.A. Fuentes, Characterization of MoO_x species on γ - Al_2O_3 , Y and ZSM-5 zeolites during thermally activated solid–solid synthesis, *J. Phys. Condens. Matter.* 16 (2004) S2319–S2327.
- [35] T. Nowitzki, A.F. Carlsson, O. Martyanov, M. Naschitzki, V. Zielasek, T. Risse, M. Schmal, H.-J. Freund, M. Bäumer, Oxidation of Alumina-Supported Co and Co - Pd Model Catalysts for the Fischer - Tropsch Reaction, *J. Phys. Chem. C.* 111 (2007) 8566–8572.

Chapter 2 – Supporting information

Tuning the Properties of Molybdenum Oxide on $\text{Al}_2\text{O}_3/\text{NiAl}(110)$: Metal Versus Oxide Deposition

2.6 Mo coverage from STM images

To determine the Mo coverage in the STM images, we need to consider the overestimation of both the height and lateral dimensions of the particles. For the height overestimation we have used literature values (Ref. 13 in the main text), which should be valid for all metallic particles. However, we have noted in the main text that the small Mo particles are likely oxidized. The overestimation of the height of these particles may therefore be smaller. The error made by this is small however, since the oxidized particles are small and not very abundant, and therefore they contribute little to the total volume.

For the estimation of the lateral overestimation we used two simple geometrical models, depicted in Figure 2.5. In both cases a Mo particle is represented by a sphere on top of the substrate. This represents a wetting angle of 180° , which is larger than can be expected for a particle with some interaction with the substrate. Measurements on Co and Pd particles revealed wetting angles between 110° - 120° (Ref. 13 in the main text). We have nonetheless chosen 180° in our model as it compensates for the height overestimation observed in STM.

The model in Figure 2.5a depicts the tip as a cone, which is representative of a very sharp STM tip. The minimal reasonable value of the tip cone angle α is 30° , when the tip consists of a pyramid of close-packed layers. Assuming this, the particle will be imaged with the profile:

$$d_{measured} = r + \sqrt{r^2 - r'^2} \text{ from } r' = 0 \text{ to } r' = \frac{1}{2}\sqrt{3}r \quad (2.1)$$

$$d_{measured} = 3r - \sqrt{3}r' \text{ from } r' = \frac{1}{2}\sqrt{3}r \text{ to } r' = \sqrt{3}r \text{ and} \quad (2.2)$$

With r and r' as indicated in S1a. The measured volume of the particle thus becomes:

$$V_{measured} = \frac{17}{6}\pi r^3 \quad (2.3)$$

And hence the lower bound of the volume overestimation is a factor $51/24$ (≈ 2.1).

The model in Figure 2.5b depicts the tip as a sphere, which is representative of a more realistic or even blunt tip. In this case, the particle will be imaged with the profile:

$$d_{measured} = \sqrt{(R + r)^2 - r'^2} + r - R \quad (2.4)$$

With R , r and r' as indicated in S1b. The measured particle volume is calculated by

$$V_{measured} = \frac{4}{3}\pi r^2(r + 3R) \quad (2.5)$$

Hence, the volume is overestimated by a factor $1+3R/r$, meaning that it depends on the ratio of the tip radius with respect to the particle radius. To get an estimate for the maximum volume overestimation, we note that the particle height/radius ratio is

unlikely to be larger than 2. Mo particles of average size had a measured radius of 1.4 nm and a corresponding measured height of 0.9 nm. Taking into account the maximum height/radius ratio and the height overestimation of 0.3 nm, these particles had a minimal real radius of 0.3 nm. Thus, the maximal radial overestimation is 4.7x. Using $r'/r = 2 \sqrt{Rr}/r$, this implies a tip radius of 1.6 nm and hence a volume overestimation of 17x.

In the considerations above we have not taken into account the decrease of the overestimation due to the detection threshold that we put at 0.3 nm versus the substrate. This means that we will be closer to the minimal overestimation than the maximal one. For this reason, we assume the tip radius to be identical to the average particle radius, such that the volume overestimation is 4x. Using this definition, we have determined the Mo coverage from the STM images and compared this to the Mo 3d / (Al 2p + Ni 3p) ratio obtained from the XPS measurements, as shown in Figure 2.6. The linear fit of the graph was used for obtaining coverages based on XPS data for the MoO_x particles.

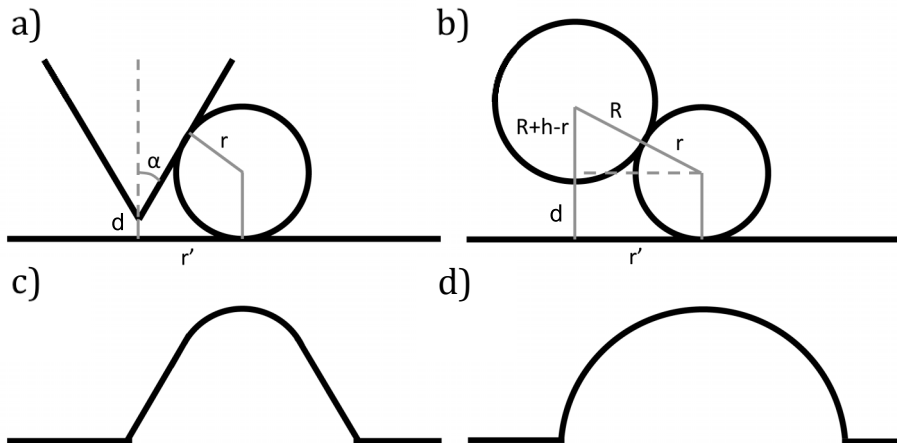


Figure 2.5: Models for the calculation of the STM height profile of a nanoparticle using a) a conical tip apex or b) a spherical tip apex. c) Resulting height profile of a), d) resulting height profile of b).

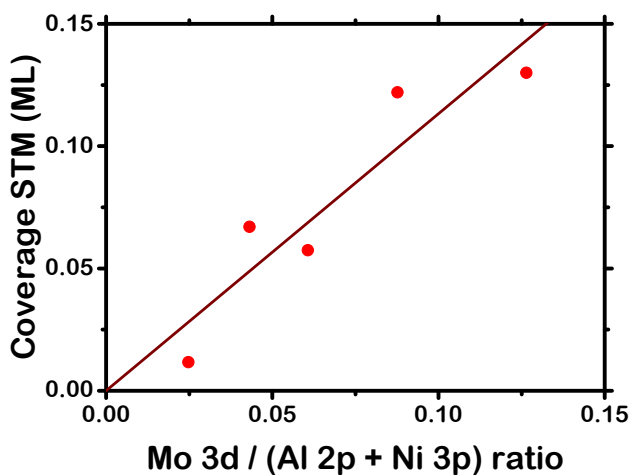


Figure 2.6: Calibration of the XPS Mo 3d / (Al 2p + Ni 3p) ratio versus the Mo coverage obtained from STM. Dots represent the data, the straight line is a linear fit constrained with a 0 intercept.

2.7 XPS analysis

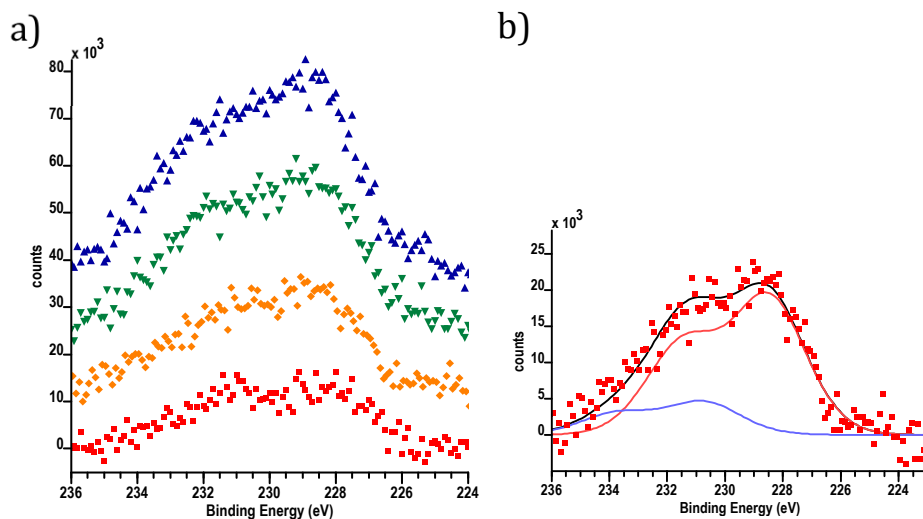


Figure 2.7: Mo 3d spectra of Mo deposited on Al₂O₃/NiAl(110) at room temperature. a) Deposition series with 0.028 ML (red), 0.049 ML (orange), 0.069 ML (green) and 0.10 ML Mo (blue) b) Spectral decomposition of 0.049 ML Mo, showing a contribution of oxidized Mo.

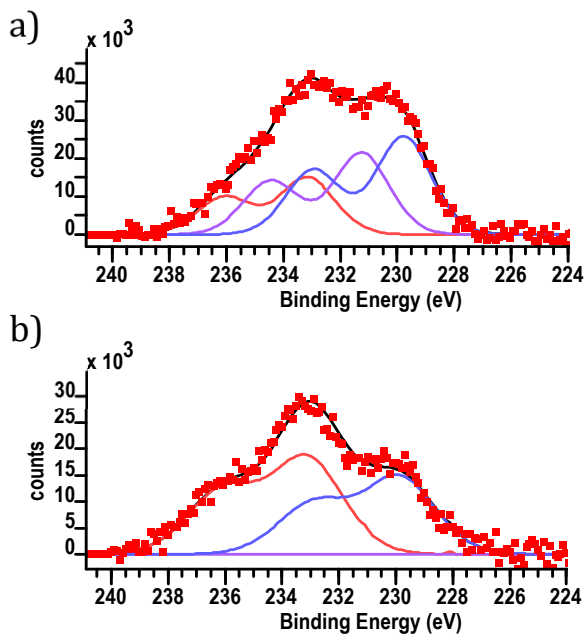


Figure 2.8: Mo 3d spectra of 0.21 ML MoO_x prepared via deposition of Mo in 5×10^{-7} mbar O_2 at room temperature. a) As deposited particles b) After annealing for 15 minutes in 1×10^{-6} mbar O_2 at 500K. Spectral decomposition: Mo^{4+} (blue), Mo^{5+} (purple), Mo^{6+} (red).

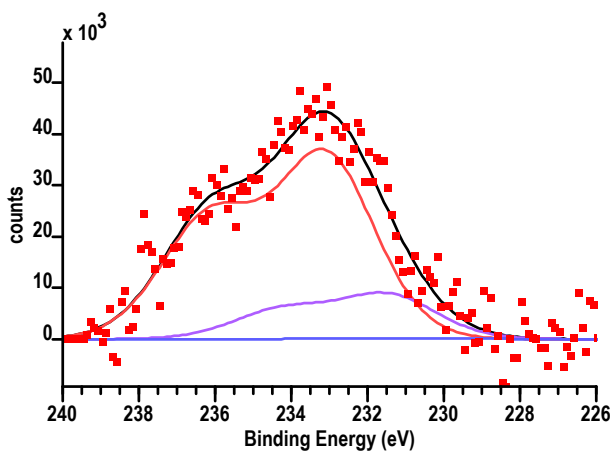


Figure 2.9: Mo 3d spectrum of 0.082 ML MoO_x prepared via deposition of MoO_x (generated on a Mo evaporation source held at approximately 1200 K in 5×10^{-6} mbar O_2) at room temperature. Spectral decomposition: Mo^{4+} (blue), Mo^{5+} (purple), Mo^{6+} (red).

Chapter 3

In situ observations of an active MoS₂ hydrodesulfurization model catalyst

The hydrodesulfurization process is used to remove harmful sulfur from oil to produce clean hydrocarbons. Using high-pressure scanning tunneling microscopy, we provide the first direct observations of a MoS₂ hydrodesulfurization catalyst under reaction conditions. We show that the active edge sites of the catalyst nanoislands adapt their sulfur, hydrogen, and hydrocarbon coverages depending on the gas environment. By comparing these observations to density functional theory calculations, we propose that the dominant edge structure during the desulfurization of CH₃SH contains a mixture of adsorbed sulfur and CH₃SH. Counterintuitively, the edge sulfur content is reduced by the presence of CH₃SH. In contrast, our theoretical analysis shows that a subtle lowering of the C-S bond-breaking barrier would result in sulfur deposition that is able to push the edge sulfur coverage far above its equilibrium value.

3.1 Introduction

The hydrodesulfurization (HDS) process is used to remove environmentally harmful sulfur from ~2.500 million tons of oil annually[1]. Thus, it is an essential step in the production of clean fuels. To accomplish the removal of sulfur, the oil is mixed with hydrogen at a pressure between 5 bar and 160 bar, with the temperature between 533 K and 653 K, producing H₂S and clean hydrocarbons[2].

MoS₂-based catalysts are widely used to drive the HDS reaction owing to their high activity, stability and low cost[2]. While research into these catalysts started as early as the 1920's[3], the atomic-scale mechanism of the reaction is still under debate. Ex situ microscopy data showed that MoS₂ is present as nanoislands that consist of one or more layers of an S-Mo-S sandwich[4–10]. The edges of the islands serve as active sites during catalysis[11–14]. Hence, mechanistic understanding of the HDS process requires detailed knowledge of the properties of the edge sites.

In most cases, the MoS₂ islands exhibit a high degree of crystallinity, resulting in island shapes close to the thermodynamically favored truncated triangle[4–8,15,16]. Consequently, two types of edge termination are mainly observed, usually referred to as the Mo edge and the S edge, with the Mo edge being dominant. *Ab initio* thermodynamics calculations predict that the sulfur coverage on both edge structures depends on the gas environment[15,17–19]. The essential element is the balance between the chemical potentials of hydrogen and sulfur atoms in the gas phase. In a sulfur-rich feed, two S edge atoms per Mo edge atom (100% coverage) are predicted. Excess hydrogen can lower this number, in the limit of pure H₂ even to zero (0% coverage).

Experimental studies in several gas environments confirmed that the edge sulfur coverage varies, depending on the balance between hydrogen and sulfur containing species in the feed[15,20,21]. However, it remains extremely challenging to study a minority species such as edge atoms under *operando* conditions. As a result, a conclusive determination of the active site structure during HDS has so far not been achieved.

Here, we present the first direct observations of the active MoS₂ edge structure under reaction conditions. Using a special-purpose high-pressure scanning tunneling microscope (STM), we have obtained atomically resolved images evidencing a mixed hydrocarbon-sulfur edge structure during the desulfurization of CH₃SH on a model catalyst. We explain the observations by comparing the STM images with density functional theory (DFT) calculations, also taking into account the role of the reaction kinetics in determining the active site structure.

3.2 Results and discussion

The combination of high pressures of corrosive gases and high temperature provides a challenging environment for STM experiments. To meet this challenge, we have used the ReactorSTM previously developed in our group[22]. At the heart of this system is a 0.5 ml flow reactor containing the STM tip. The reactor walls are defined by a cap placed inside the scan piezo, the catalyst sample, the STM body, and polymer seals in between these elements. Gas capillaries drilled in the STM body provide a connection to a gas supply system that controls the composition, flow, and pressure of the gases in the flow reactor.

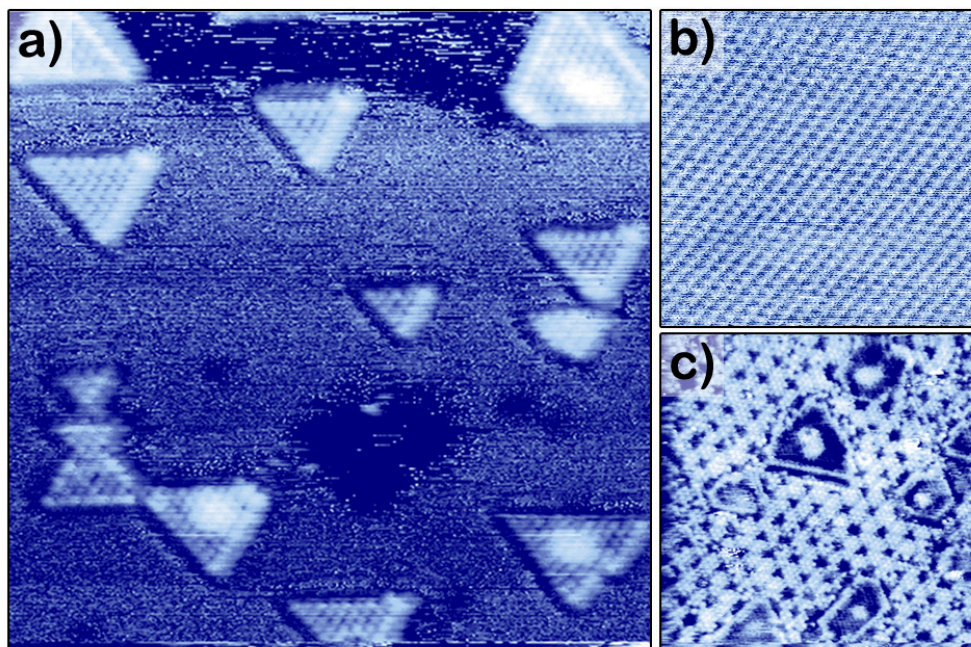


Figure 3.1: STM images of a MoS₂/Au(111) model catalyst and its stability under desulfurization conditions. a) Catalyst after preparation in UHV. 16 x 16 nm², U_{bias} = -0.3 V, I_t = 320 pA. b) Clean Au surface imaged in 1 bar CH₃SH at 523 K, showing the (1x1) Au lattice. 6 x 6 nm², U_{bias} = -0.3 V, I_t = 550 pA. c) MoS₂/Au(111) after 1 day in 1 bar of a 1:9 CH₃SH/H₂ mixture, showing a sulfur overlayer on the Au(111) substrate. 20 x 20 nm², U_{bias} = -0.3 V, I_t = 645 pA.

To mimic realistic industrial conditions, the pressure can be raised up to 1 bar, while the sample is heated up to 573 K using a filament located on the backside of the sample. A key element in the design is that the scan piezo is not in contact with the gases in the reactor. This geometry, in combination with a careful choice of chemically resistant materials, allows for the use of highly corrosive gases such as H₂S at elevated temperatures. The use of PtIr tips prevents tip degradation during the measurements, albeit that frequent changes in imaging quality cannot be avoided. To combine the

high-pressure experiments with more traditional ultrahigh vacuum (UHV) surface preparation and characterization techniques, the flow reactor can be opened and closed inside a UHV system, which contains a.o. an ion gun, an evaporation source, and an X-ray photoelectron spectroscopy apparatus.

As a first step, we established a suitable model catalyst; one that is conductive to allow for STM measurements and stable under HDS conditions. Following the successful recipe of the Århus group[4,15], we synthesized MoS₂ particles on a Au(111) substrate (see Methods section), yielding crystalline islands with a predominantly triangular shape (see Figure 3.1a). These islands were shown to nearly exclusively expose the Mo edge[15], which we will focus on hereafter.

The stability of the model catalyst during HDS depends on the chosen conditions. To allow for unambiguous identification of edge structures in STM, we chose the simple CH₃SH molecule as our organosulfur compound to be desulfurized. Like all thiols, CH₃SH readily adsorbs on gold surfaces[23]. However, at the temperature of our catalytic experiments (523 K), only the (1x1) Au lattice is imaged, even in 1 bar CH₃SH (see Figure 3.1b). Over time, a sulfur overlayer is formed, resulting from decomposition of CH₃SH or H₂S. As long as H₂S is not added to the reactor feed, this process requires hours, making it too slow to interfere with the HDS catalysis on the MoS₂ particles through sulfur spillover. However, the ‘encapsulation’ of the MoS₂ particles by the sulfur overlayer on the Au substrate, depicted in Figure 3.1c, could limit the accessibility of the active edge sites. To prevent this, we restricted the duration of our HDS experiments to a few hours, after which a fresh model catalyst was prepared.

As a next step, we characterized the appearance of the fully sulfided MoS₂ edge structure obtained after preparation of the MoS₂ particles in 2x10⁻⁶ mbar pure H₂S. Using DFT calculations, Lauritsen *et al.* [15] identified the resulting edge structure as the 100%S edge, which contains an S dimer on every Mo edge atom. Its appearance in STM images is characterized by a periodicity of one lattice spacing along the edge and by a registry shift of half a lattice spacing in the apparent position of the edge atoms with respect to those on the basal plane. This shift is highlighted by the yellow line in Figure 3.2a. Note from the ball model in Figure 3.2a that the apparent position of the edge atoms in STM deviates from their geometrical position. This is a result of the fact that the electronic states around the Fermi level, which are probed by STM, are mostly located in between the edge atoms (see Figure 3.6a in the Supporting Information).

Our first step towards reaction conditions is to image the model catalyst in high H₂ pressure and at high temperatures. Under these conditions, the appearance of the edge sites changes (see Figure 3.2b), indicating that the edge sites have been reduced. The registry shift of the “edge atoms” with respect to the basal plane atoms that was apparent for the 100%S edge has been removed, while maintaining the periodicity along the edge of one lattice spacing. The structure in Figure 3.2b was not dependent on temperature within the range from 323 K to 523 K probed here. It should be noted

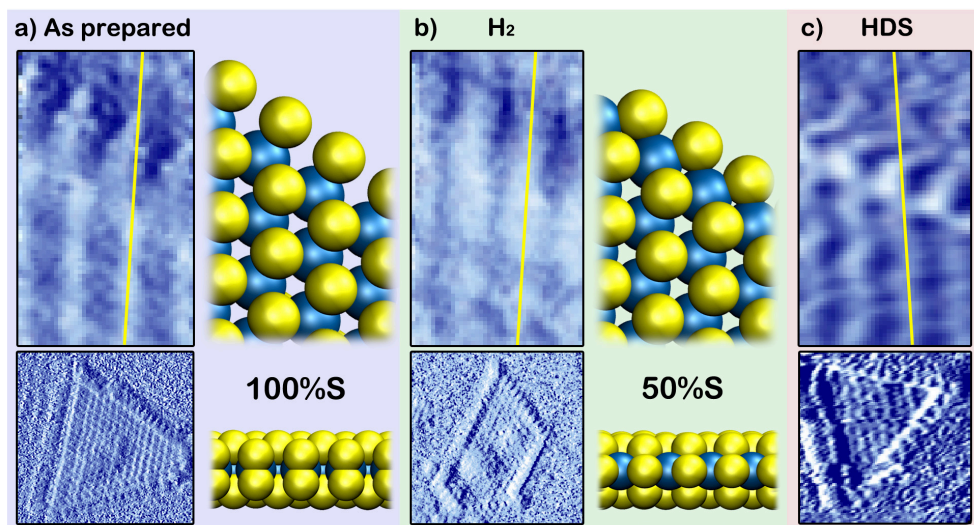


Figure 3.2: MoS₂ edge structure in various gas environments. The bottom panels show the original images, which were differentiated to highlight the atomic contrast. The top panels depict the averaged edge unit cell obtained from the bottom images. For a) and b), the ball models represent the structures that could directly be identified from comparison to simulated STM images (see Figure 3.6 in the Supporting Information). Blue: Mo, yellow: S. a) Catalyst after preparation in 2×10^{-6} mbar H₂S at 723 K, imaged in UHV at room temperature. 6.6×6.6 nm², $U_{\text{bias}} = -0.3$ V, $I_t = 560$ pA. b) Catalyst imaged in 1 bar H₂ at 323 K. 6.6×6.6 nm², $U_{\text{bias}} = -0.3$ V, $I_t = 630$ pA. c) Catalyst during the desulfurization of CH₃SH in 1 bar 1:9 CH₃SH/H₂ at 523 K. 3.8×3.8 nm², $U_{\text{bias}} = -0.3$ V, $I_t = 400$ pA.

however that at elevated temperatures STM may probe a time-averaged structure, which could obscure diffusing S vacancies or adsorbed S and H atoms.

The edge structure without registry shift in Figure 3.2b was also observed after deposition of Mo in H₂S/H₂ mixtures[15] or dimethylsulfide[24]. It was interpreted as the 50%S structure by comparison to simulated STM images. Our STM simulations corroborate this assignment, although hydrogen adsorption cannot be excluded (see Section 3.5 in the Supporting Information). We note that Bruix *et al.* did not find the registry shift between the 100%S and the 50%S edge structures for MoS₂/Au(111) in their STM simulations[21]. However, none of the structures described in their work matches the experimental observations of the reduced edge structure.

Having established our ability to observe changes in the MoS₂ edge structure under high-pressure, high-temperature conditions, we are ready to study our model catalyst in its active form during the desulfurization of CH₃SH. Figure 3.2c shows the structure observed in a 1 bar 1:9 CH₃SH/H₂ mixture at 523 K. Before imaging, the flow reactor was allowed to stabilize for more than 2 hours to ensure a steady state situation. Figure 3.2c shows that the edge structure under hydrodesulfurization conditions has

clearly changed with respect to the structure in pure hydrogen. Based on the apparent registry of the edge atoms, one could assign the structure to an (almost) 100%S-covered edge. An alternative explanation is the formation of CH₃SH adsorption structures.

To enable an unambiguous assignment of the edge structure observed during the hydrodesulfurization of CH₃SH, we consider the thermodynamic and kinetic aspects of the catalytic process using DFT calculations. First, we assess the thermodynamic stability of various edge structures in a gas environment that only consists of H₂ and H₂S. Figure 3.3 depicts the most stable edge structure for Au-supported MoS₂ as a function of $\Delta\mu_S$ and $\Delta\mu_H$. These quantities are directly related to the temperature, the H₂S pressure, and the H₂ pressure through Equations 3.5 and 3.6 in the Methods section. The phase diagram in Figure 3.3 corroborates the observation that the MoS₂ edge structure depends on the gas environment, showing large variations in both S and H coverage. A quantitative comparison to earlier work shows an agreement to within 0.15 eV for the relative stability of the 50%S and 100%S structures[15,18,19] (see Table 3.1 in the Supporting Information). Remarkably however, we find a preference for low-symmetry structures such as 38%S-x%H and 63%S-x%H over a wide range of conditions. These structures were not taken into account in earlier studies and therefore did not show up in the predicted phase diagrams.

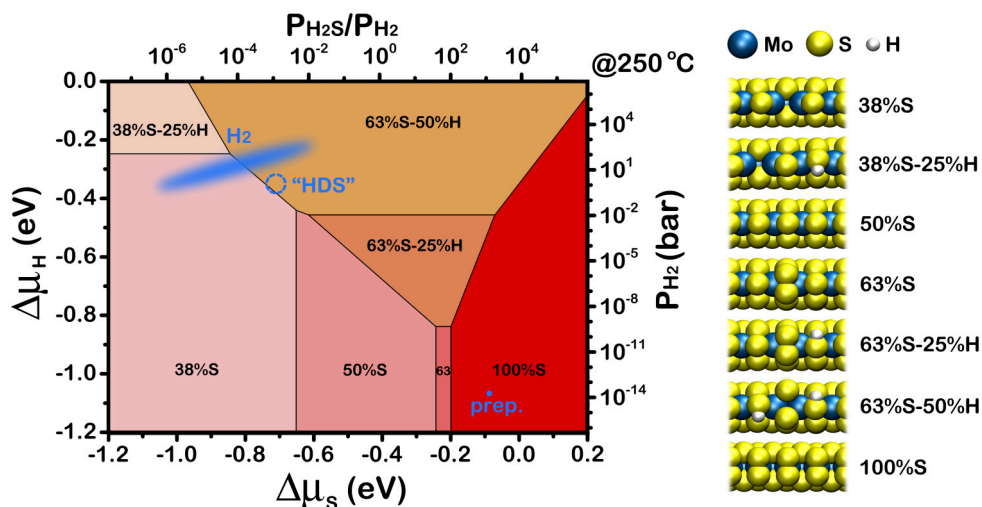


Figure 3.3: *Ab initio* thermodynamics phase diagram of the MoS₂ edge structures in H₂/H₂S mixtures for Au-supported MoS₂. On the axes, $\Delta\mu_S$ and $\Delta\mu_H$ designate the entropic parts of the chemical potentials of S and H atoms in the gas phase, respectively. These are directly related to the temperature, the H₂S pressure, and the H₂ pressure (see Methods section). The experimental conditions during catalyst preparation, in 1 bar hydrogen (assuming 1 ppm H₂S contamination), and during HDS (naïve approximation) are indicated in blue. The ball models represent side views of the structures present in the phase diagram. Note that the edges are periodic in the left-right direction.

The trends of the sulfur and hydrogen coverages in various gas environments can be understood based on the variation in adsorption strength per H or S atom of the various structures. Generally, one expects the adsorption strength per S or H atom to decrease at higher S or H coverage. Hence, higher-coverage structures require a higher chemical potential in order to form. This trend is indeed observed in the phase diagram. However, the 75%S and 88%S structures do not appear. In this coverage range, the registry of the S edge atoms changes with respect to the S atoms on the basal plane, leading to unstable structures with strained bonds. For the hydrogenated phases, 63%S-x%H shows a remarkably large range of stability. An explanation for this comes from the comparison of the 50%S and 63%S structures in Figures 3.2b and 3.3. For the 50%S case, hydrogen adsorption induces buckling of the edge S atoms, implying the presence of compressive stress. The buckling disappears upon the adsorption of a sulfur atom (yielding the 63%S-50%H structure), implying a stabilizing stress relief. For the small particles used in HDS, corner sites may provide similar stress relief. It is therefore not a priori clear whether the 63%S-x%H structures are similarly stable in such more realistic catalysts.

Using equations 3.5 and 3.6 (see Methods section), we have placed the experimental conditions in the phase diagram of Au-supported MoS₂. For the freshly prepared particles, we have used an H₂S pressure of 2×10^{-6} mbar H₂S and a temperature of 573 K for the calculation, even though imaging was performed in vacuum at room temperature. We chose these conditions because the edge structure is not capable of changing in vacuum at temperatures below 573 K[15,21]. As expected, the phase diagram indicates the observed 100%S structure to be the most stable under these conditions. For the reduction in 1 bar H₂, we assumed an H₂S contamination level of 1 ppm. Depending on the temperature, the phase diagram indicates an edge coverage of 38%S to 63%S, with hydrogen adsorption on most structures. Again, this is in good agreement with the time-averaged 50%S-50%H structure observed with STM.

To represent the hydrodesulfurization experiment in the phase diagram, we need to assume that the gas environment can be described solely in terms of H₂S and H₂ chemical potentials. This would be the case if the adsorption of hydrocarbons, e.g. CH₃SH, is ignored and the overall HDS reaction is either completely equilibrated or slow with respect to the reactions of H₂ and H₂S with the MoS₂ edges. From mass spectroscopic product analysis, we know that in our case the conversion of CH₃SH is low due to the extremely low number of active sites on our planar model catalyst. Even at an extremely high turnover frequency of 1000 s⁻¹ per site, only approximately 1 mbar H₂S would be generated. If we assume this upper limit and ignore CH₃SH adsorption, the chemical potential of sulfur in our HDS experiment is determined by the temperature (523 K), the H₂S pressure (~0.001 bar) and the H₂ pressure (0.9 bar), as indicated in Figure 3.3. This would lead to a 63%S-50%H structure, which has a slightly higher S coverage than the 50%S-50%H structure predicted in earlier studies for these conditions[15,18]. It should be clear however that the 100%S structure is not a likely candidate for the structure we observe in STM under reaction conditions.

To investigate the possibility of CH_3SH adsorption structures, we calculated the CH_3SH adsorption energy for several edge S and H coverages on Au-supported MoS_2 (see Table 3.2 in the Supporting Information). While CH_3SH can bind in all cases, only the 38%S-25% CH_3SH structure in Figure 3.4 is thermodynamically more stable ($\Delta G_{\text{form}} = -0.08$ eV) than the clean 63%S-50%H structure under our reaction conditions ($P_{\text{CH}_3\text{SH}} = 0.1$ bar, $P_{\text{H}_2\text{S}} = \sim 0.001$ bar, $P_{\text{H}_2} = 0.9$ bar, 523 K). Hence, if H_2 , H_2S , and CH_3SH would equilibrate with our model catalyst, i.e. if the HDS reaction would be slow enough not to affect this thermodynamic equilibrium, the 38%S-25% CH_3SH structure should prevail. For H_2S pressures lower than the upper limit of 1 mbar we, the preference for the 38%S-25% CH_3SH is further increased. Figure 3.4b shows an STM simulation of the 38%S-25% CH_3SH structure. Clearly, the edge atoms appear out of registry with the basal plane S atoms, in agreement with the experimental observations. The irregular appearance in Figure 3.4b will be time-averaged in the STM images at 523 K, because of the fast adsorption/desorption kinetics of CH_3SH (free energy barriers of 0.51 eV and 0.87 eV, respectively).

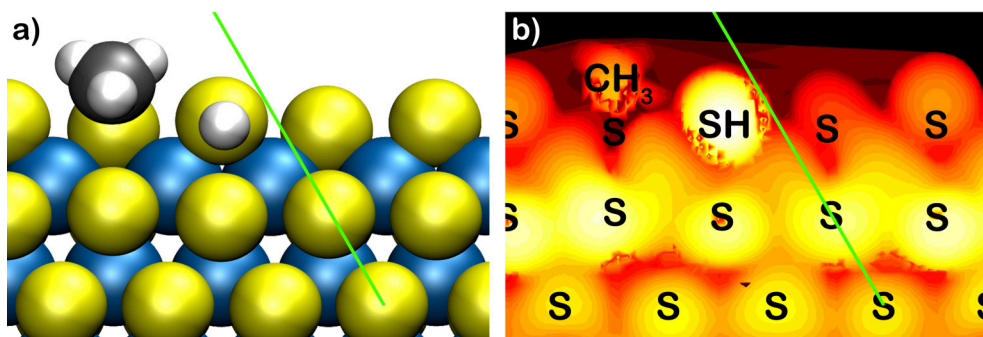
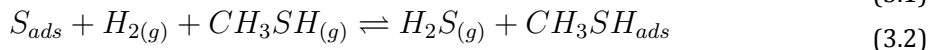


Figure 3.4: Thermodynamically preferred structure under the experimental desulfurization conditions ($P_{\text{CH}_3\text{SH}} = 0.1$ bar, $P_{\text{H}_2\text{S}} = \sim 0.001$ bar, $P_{\text{H}_2} = 0.9$ bar, 523 K). The green lines highlight the registry shift of the edge atoms with respect to the basal plane S atoms, which was also observed in the experiment. a) Ball model. b) Simulated STM image for $U_s = -0.3$ V, using an electron density contour value of 1×10^{-5} AU.

Since we have come close to industrial conditions in our HDS experiment, we expect conversion of CH_3SH to CH_4 . Hence, the reaction should be in a steady state rather than in the static equilibrium discussed in the previous paragraph. To model how this affects the prevalent edge structure, we computed a reaction network linking a set of reaction intermediates on Au-supported MoS_2 (see Figure 3.5). The catalytic cycles in the network consist of three stages: the conversion of CH_3SH to CH_4 , leaving behind a sulfur atom on the MoS_2 edge, the desorption of this sulfur atom as H_2S , and the adsorption of hydrogen. From Figure 3.5, it is clear that the conversion of CH_3SH is essentially a one-way reaction due to its high energy gain. In contrast, the adsorption/desorption steps of H_2 , H_2S , and CH_3SH are all reversible.

Putting this in a simple steady state rate equation model we obtain:



$$\frac{[S_{ads}]}{[CH_3SH_{ads}]} = \frac{k_1 + k_{-2}P_{H_2S}}{k_2P_{H_2}P_{CH_3SH}} \quad (3.3)$$

Although highly simplified, this model provides some insight into the effect of CH_3SH conversion on the MoS_2 edge structure. When the conversion faces a high barrier, rate constant k_1 will be low. In such a case, the edge structure should be close to the equilibrium of Equation 3.2. In contrast, when the barrier for CH_3SH conversion would be lower than the H_2/H_2S adsorption/desorption barriers, one should expect that adsorbed CH_3SH would be largely replaced by sulfur atoms.

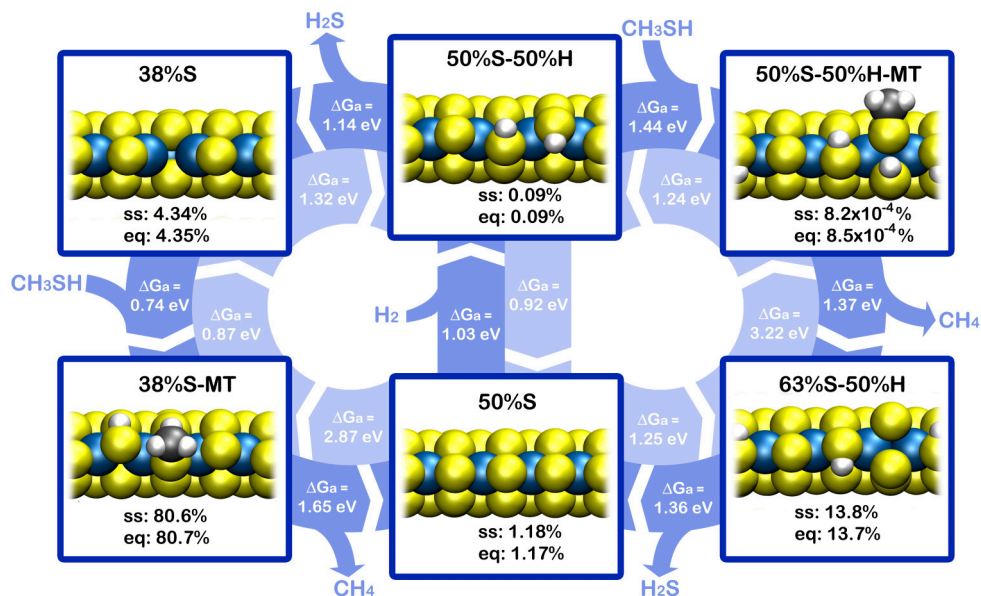


Figure 3.5: Reaction network for CH_3SH desulfurization on $MoS_2/Au(111)$. The activation free energy barriers (ΔG_a) indicated in the arrows were calculated based on the experimental conditions ($P_{CH_3SH} = 0.1$ bar, $P_{H_2S} = \sim 0.001$ bar, $P_{H_2} = 0.9$ bar, 523 K). The abundances of intermediates in steady state conditions and in an equilibrium where the C-S bond breaking step is disabled are designated by ss and eq, respectively. The steady state concentrations were derived using transition state theory and rate equation modeling (see Methods section). “MT” corresponds to methane thiol.

Figure 3.5 shows that the C-S bond breaking barriers are slightly higher than the H_2S desorption barriers. Because the rate constants have an exponential dependence on the energy barrier, this translates into orders of magnitude difference in rate. Indeed,

when we quantify the abundances of all reaction intermediates (see Methods section), we still find an 80.6% abundance of the 38%S-CH₃SH edge state, compared to 80.7% under equilibrium conditions. Hence it appears that the structure observed in our HDS experiment is the 38%S-CH₃SH edge state.

In a more general view, our theoretical analysis identifies two mechanisms that can steer the MoS₂ edge structure away from its equilibrium with H₂ and H₂S during the HDS reaction. First, the adsorption of organic molecules may favor different edge S and H coverages. In our experiments, this leads to the counterintuitive observation that the edge S content is reduced due to CH₃SH adsorption: the 67%S-50%H structure is favored in the absence of CH₃SH adsorption, whereas the 38%S-25%CH₃SH structure is the most stable one when we do take CH₃SH adsorption into account. This effect is likely also present for industrially important reaction intermediates such as reduced thiophenes, which adsorb strongly[25]. A second mechanism is the deposition of sulfur via C-S bond scission. Although this appears to have only a minor effect in our experiment, subtle changes in the barrier for C-S bond breaking can have major consequences for the average edge structure. For instance, if the C-S barrier in the network in Figure 3.4 were lowered by 0.3 eV, the 63%S-50%H structure would become dominant. Hence, support effects, the presence of defects such as corner sites, and the nature of the hydrocarbons that are desulfurized can all cause large variations in the average structure of MoS₂ under reaction conditions.

3.3 Conclusion

Using a dedicated high-pressure scanning tunneling microscope, we have studied the catalytically active edge structure of MoS₂ nanoparticles on Au(111) in mixtures of H₂, H₂S, and CH₃SH at temperatures up to 523 K. In hydrogen, trace amounts of sulfur in the feed are sufficient to maintain a sulfur coverage of 1 edge S atom per edge Mo atom. Surprisingly, the edge is reduced during the hydrodesulfurization of CH₃SH to accommodate CH₃SH adsorption. Due to the slow C-S bond scission on our model catalyst, the system remains close to an equilibrium state. However, our theoretical analysis indicates that small changes in the reaction rate or the reaction mechanism, which could originate from support effects or from the presence of different hydrocarbons, can have a major influence on the average MoS₂ edge structure. In particular, for highly active MoS₂ catalysts one may expect that sulfur deposition by the conversion of organosulfur compounds increases the edge S coverage under hydrodesulfurization conditions, rather than to decrease it, as was found here. Hence, we conclude that the prevalent structure of the active sites during hydrodesulfurization catalysis on MoS₂ likely depends both on the precise type of catalyst and the nature of the feedstock.

3.4 Methods

3.4.1 Model catalyst preparation

Clean, atomically smooth Au(111) was prepared by cycles of 1 keV Ar⁺ bombardment and annealing at 900 K. MoS₂ particles were deposited by evaporation of Mo in 1x10⁻⁶ mbar H₂S, with the Au substrate at 423 K, followed by annealing at 723 K in 2x10⁻⁶ mbar H₂S.

3.4.2 High-pressure experiments.

All gas lines were flushed with argon for at least 30 minutes prior to each experiment. To start the high-pressure exposure, the reactor was slowly pressurized in H₂ and subsequently heated to the desired temperature. For the HDS experiments, CH₃SH was mixed in the reactor feed only after reaching 523 K. In order to minimize the thermal drift in the microscope, the system was allowed an equilibration period of approximately 90 minutes. To cope with the remaining drift, image acquisition times of around 20 seconds per image were employed. As the noise level increased under high-pressure, high-temperature conditions, a 3x3 pixel averaging was applied for clarity.

3.4.3 Theoretical analysis.

All DFT calculations were carried out with the BAND program package[26–30], using the PBE density functional[31], Grimme van der Waals corrections[32], and scalar relativistic corrections. A triple- ζ plus polarization basis set was used for the valence orbitals, while the core orbitals were kept frozen in the same state as in the free atoms. In general, default settings of the BAND program were used. The Self-Consistent Field convergence criterion was set at 10⁻⁶ Hartree atomic units, while the geometrical optimization criterion was set at 10⁻² Hartree per nanometer.

A (4x4) MoS₂ unit cell was employed, in the form of a stripe with periodicity in one direction. The stripe contains both an S-type edge and an Mo-type edge. The S-type edge was kept fully covered in all calculations (2 S edge atoms per Mo edge atom). The length of the unit cell was kept at the value optimized for 50%S coverage: 1.248 nm. For the calculations where the gold support was included, the Au(111) surface was modeled by a 2 layer slab with a lattice parameter commensurate with the MoS₂ stripe. The S-Mo-S-Au-Au stacking was chosen as A-B-A-B-C, with a S-Au layer spacing of 0.442 nm. The number of k points chosen for sampling the Brillouin zone was 3 throughout.

Transition states were located as follows: for a chosen reaction coordinate (usually an interatomic distance) total energies were computed for a range of fixed values (while optimizing all other degrees of freedom). For the structure of highest energy a partial hessian was calculated, including atoms at or close to the reaction site. The most negative eigenvalue of this partial hessian was used to locate the saddle point. In most cases the search had to be restarted several times by recomputing the partial hessian

on the structure with the smallest gradient found so far. It was checked that the partial hessian of the final structure had precisely one negative eigenvalue.

The reaction energies (ΔE_r) used in the computation of phase diagrams were calculated per unit cell as:

$$\Delta E_r = E_{MoS_2, S_x H_y} - E_{MoS_2} - x E_{H_2S} - \left(\frac{1}{2}y - x\right) E_{H_2} \quad (3.4)$$

In Equation 3.4, E_x denotes the total electronic energy obtained from DFT for the respective structure. In order to calculate the free energy of an edge structure, entropic corrections need to be applied:

$$\Delta \mu_S = RT \ln\left(\frac{P_{H_2S}}{P_{H_2}}\right) - T(S_{H_2S}^o - S_{H_2}^o) \quad (3.5)$$

$$\Delta \mu_H = \frac{1}{2}(RT \ln(P_{H_2}) - T S_{H_2}^o) \quad (3.6)$$

The standard entropies (S_x^o) in these equations were obtained from thermodynamic tables[33]. Using the entropic corrections, one can compute the free energy change involved in a reaction as:

$$\Delta G_r = \Delta E_r - x \Delta \mu_S - y \Delta \mu_H \quad (3.7)$$

The structure with the lowest free energy per unit cell at a particular combination of $\Delta \mu_S$ and $\Delta \mu_H$ values will be the phase present under those conditions. Note that with this definition of the free energy, we assume that all solid phases have zero entropy and that there is no change in heat capacity during the reaction.

To model the adsorption of CH_3SH , we first calculated the adsorption energy:

$$\Delta E_{ads} = E_{MoS_2, S_x H_y, MT_z} - E_{MoS_2, S_x H_y} - z E_{MT} \quad (3.8)$$

In Equation 3.8, MT corresponds to CH_3SH . The thermodynamic stability of the adsorbed CH_3SH structure was calculated as its formation free energy with respect to the most stable phase in the absence of CH_3SH adsorption:

$$\Delta G_f = \Delta E_{ads} - z \Delta \mu_{MT} + \Delta G_{r-MoS_2, S_x H_y} - \Delta G_{r-MoS_2, S_n H_m} \quad (3.9)$$

$$\Delta \mu_{MT} = RT \ln(P_{MT}) - T S_{MT}^o \quad (3.10)$$

In Equation 3.9, $MoS_2, S_n H_m$ is the most stable structure in the absence of CH_3SH adsorption.

Finally, we performed a kinetic analysis using the free energy barriers that link the reaction intermediates. Entropic corrections were again applied using equations 3.5, 3.6 and 3.10. Rate constants were calculated from the free energy barriers (ΔG_a) using transition state theory:

$$k = \frac{k_B T}{h} e^{\frac{-\Delta G_a}{k_B T}} \quad (3.11)$$

Here, we assume that there is no communication between adjacent unit cells. By incorporating the pressure effect on the free energy in the calculation of k , all rates take the form:

$$r_n = k_n \theta_n \quad (3.12)$$

When the reaction reaches steady state, all coverages will be fixed. Thus, we obtain a set of linear equations, shown here for the example of an intermediate with two links to other intermediates.

$$\frac{d\theta_n}{dt} = k_{n-1}\theta_{n-1} + k_{-n}\theta_{n+1} - (k_{-(n-1)} + k_n)\theta_n = 0 \quad (3.13)$$

By solving this set of equations, one obtains the steady state coverage of the various intermediates.

References

- [1] R.P. Silvy, Refining catalyst market begins to recover in 2010, *Oil Gas J.* 108 (2010) 40–43.
- [2] M.A. Fahim, T.A. Al-Sahhaf, A. Elkilani, *Fundamentals of Petroleum Refining*, Elsevier, Oxford, 2010.
- [3] I.G. Farbenindustrie A.G., British Patent 315439, 1928.
- [4] S. Helveg, J. Lauritsen, E. Lægsgaard, I. Stensgaard, J. Norskov, B. Clausen, H. Topsøe, F. Besenbacher, Atomic-scale structure of single-layer MoS₂ nanoclusters, *Phys. Rev. Lett.* 84 (2000) 951–4.
- [5] L.P. Hansen, Q.M. Ramasse, C. Kisielowski, M. Brorson, E. Johnson, H. Topsøe, S. Helveg, Atomic-scale edge structures on industrial-style MoS₂ nanocatalysts, *Angew. Chemie - Int. Ed.* 50 (2011) 10153–10156.
- [6] Y. Zhu, Q.M. Ramasse, M. Brorson, P.G. Moses, L.P. Hansen, C.F. Kisielowski, S. Helveg, Visualizing the stoichiometry of industrial-style Co-Mo-S catalysts with single-atom sensitivity, *Angew. Chemie - Int. Ed.* 53 (2014) 10723–10727.
- [7] J. Kibsgaard, J. V. Lauritsen, E. Lægsgaard, B.S. Clausen, H. Topsøe, F. Besenbacher, Cluster-support interactions and morphology of MoS₂ nanoclusters in a graphite-supported hydrotreating model catalyst, *J. Am. Chem. Soc.* 128 (2006) 13950–13958.
- [8] J. Kibsgaard, B.S. Clausen, H. Topsøe, E. Lægsgaard, J. V. Lauritsen, F. Besenbacher, Scanning tunneling microscopy studies of TiO₂-supported hydrotreating catalysts: Anisotropic particle shapes by edge-specific MoS₂-support bonding, *J. Catal.* 263 (2009) 98–103.
- [9] A. Tuxen, J. Kibsgaard, H. Gøbel, E. Lægsgaard, H. Topsøe, J. V. Lauritsen, F. Besenbacher, Size threshold in the dibenzothiophene adsorption on MoS₂ nanoclusters, *ACS Nano.* 4 (2010) 4677–4682.
- [10] M. Brorson, A. Carlsson, H. Topsøe, The morphology of MoS₂, WS₂, Co-Mo-S, Ni-Mo-S and Ni-W-S nanoclusters in hydrodesulfurization catalysts revealed by HAADF-STEM, *Catal. Today.* 123 (2007) 31–36.
- [11] J. V. Lauritsen, M. Nyberg, J.K. Nørskov, B.S. Clausen, H. Topsøe, E. Lægsgaard, F. Besenbacher, Hydrodesulfurization reaction pathways on MoS₂ nanoclusters revealed by scanning tunneling microscopy, *J. Catal.* 224 (2004) 94–106.
- [12] A.K. Tuxen, H.G. Führtbauer, B. Temel, B. Hinnemann, H. Topsøe, K.G. Knudsen, F. Besenbacher, J. V. Lauritsen, Atomic-scale insight into adsorption of sterically hindered dibenzothiophenes on MoS₂ and Co-Mo-S hydrotreating catalysts, *J. Catal.* 295 (2012) 146–154.
- [13] P.G. Moses, B. Hinnemann, H. Topsøe, J.K. Nørskov, The hydrogenation and direct desulfurization reaction pathway in thiophene hydrodesulfurization over MoS₂ catalysts at realistic conditions: A density functional study, *J. Catal.* 248 (2007) 188–203.
- [14] P.G. Moses, B. Hinnemann, H. Topsøe, J.K. Nørskov, The effect of Co-promotion on MoS₂ catalysts for hydrodesulfurization of thiophene: A density functional study, *J. Catal.* 268 (2009) 201–208.
- [15] J. V. Lauritsen, M. V. Bollinger, E. Lægsgaard, K.W. Jacobsen, J.K. Nørskov, B.S.

- Clausen, H. Topsøe, F. Besenbacher, Atomic-scale insight into structure and morphology changes of MoS₂ nanoclusters in hydrotreating catalysts, *J. Catal.* 221 (2004) 510–522.
- [16] B. Baubet, M. Girleanu, A.S. Gay, A.L. Taleb, M. Moreaud, F. Wahl, V. Delattre, E. Devers, A. Hugon, O. Ersen, P. Afanasiev, P. Raybaud, Quantitative Two-Dimensional (2D) Morphology-Selectivity Relationship of CoMoS Nanolayers: A Combined High-Resolution High-Angle Annular Dark Field Scanning Transmission Electron Microscopy (HR HAADF-STEM) and Density Functional Theory (DFT) Study, *ACS Catal.* 6 (2016) 1081–1092.
- [17] M. V. Bollinger, K.W. Jacobsen, J.K. Nørskov, Atomic and electronic structure of MoS₂ nanoparticles, *Phys. Rev. B.* 67 (2003) 085410.
- [18] P.Y. Prodhomme, P. Raybaud, H. Toulhoat, Free-energy profiles along reduction pathways of MoS₂ M-edge and S-edge by dihydrogen: A first-principles study, *J. Catal.* 280 (2011) 178–195.
- [19] S. Cristol, J.F. Paul, E. Payen, D. Bougeard, S. Clémendot, F. Hutschka, Theoretical Study of the MoS₂(100) Surface: A Chemical Potential Analysis of Sulfur and Hydrogen Coverage, *J. Phys. Chem. B.* 106 (2002) 5659–5667.
- [20] N. Dinter, M. Rusanen, P. Raybaud, S. Kasztelan, H. Toulhoat, Temperature-programmed reduction of unpromoted MoS₂-based hydrodesulfurization catalysts : Experiments and kinetic modeling from first principles, *J. Catal.* 267 (2009) 67–77.
- [21] A. Bruix, H.G. Führtbauer, A.K. Tuxen, A.S. Walton, M. Andersen, S. Porsgaard, F. Besenbacher, B. Hammer, J. V Lauritsen, In Situ Detection of Active Edge Sites in Single-Layer MoS₂ Catalysts, *ACS Nano.* 9 (2015) 9322–9330.
- [22] C.T. Herbschleb, P.C. van der Tuijn, S.B. Roobol, V. Navarro, J.W. Bakker, Q. Liu, D. Stoltz, M.E. Cañas-Ventura, G. Verdoes, M.A. van Spronsen, M. Bergman, L. Crama, I. Taminiau, A. Ofitserov, G.J.C. van Baarle, J.W.M. Frenken, The ReactorSTM: atomically resolved scanning tunneling microscopy under high-pressure, high-temperature catalytic reaction conditions., *Rev. Sci. Instrum.* 85 (2014) 083703.
- [23] H. Häkkinen, The gold–sulfur interface at the nanoscale, *Nat. Chem.* 4 (2012) 443–455.
- [24] H.G. Führtbauer, A.K. Tuxen, Z. Li, H. Topsøe, J. V. Lauritsen, F. Besenbacher, Morphology and atomic-scale structure of MoS₂ nanoclusters synthesized with different sulfiding agents, *Top. Catal.* 57 (2014) 207–214.
- [25] Y. V. Joshi, P. Ghosh, P.S. Venkataraman, W.N. Delgass, K.T. Thomson, Electronic descriptors for the adsorption energies of sulfur-containing molecules on co/mos₂, using dft calculations, *J. Phys. Chem. C.* 113 (2009) 9698–9709.
- [26] BAND2014, (2014). <http://scm.com>.
- [27] G. Te Velde, E.J. Baerends, Precise density-functional method for periodic structures, *Phys. Rev. B.* 44 (1991) 7888–7903.
- [28] G. Wiesenekker, E.J. Baerends, Quadratic integration over the three-dimensional Brillouin zone, *J. Phys. Condens. Matter.* 3 (1991) 6721–6742.
- [29] M. Franchini, P.H.T. Philipsen, L. Visscher, The becke fuzzy cells integration scheme in the amsterdam density functional program suite, *J. Comput. Chem.*

- 34 (2013) 1819–1827.
- [30] M. Franchini, P.H.T. Philipsen, E. Van Lenthe, L. Visscher, Accurate Coulomb potentials for periodic and molecular systems through density fitting, *J. Chem. Theory Comput.* 10 (2014) 1994–2004.
- [31] J.P. Perdew, K. Burke, M. Ernzerhof, Generalized Gradient Approximation Made Simple, *Phys. Rev. Lett.* 77 (1996) 3865–3868.
- [32] S. Grimme, S. Ehrlich, L. Goerigk, Effect of damping function in dispersion corrected Density Functional Theory, *J. Comput. Chem.* 32 (2010) 1456–1465.
- [33] NIST, Computational Chemistry Comparison and Benchmark Database, (2016). <http://cccbdb.nist.gov/>.

Chapter 3 - Supporting information

In situ observations of an active MoS₂ hydrodesulfurization model catalyst

3.5 Appearance of MoS₂ edge structures in scanning tunneling microscopy

The electrons that make up the tunneling current in scanning tunneling microscopy (STM) originate from states close to the Fermi level. As the local density of these states is usually not evenly distributed over the atoms of the sample, the appearance of structures in STM often does not directly reflect the atomic structure. The edges of MoS₂ islands present a particularly pronounced case of such a discrepancy. Hence, in order to interpret the STM images properly, it is necessary to compare them to calculations of the local density of states using density functional theory (DFT). STM images are usually modeled as contours of equal values of the local density of states (LDOS) around the Fermi level. The LDOS around the Fermi level is typically obtained by summation over all LDOS contributions at and around the Fermi level with a Gaussian weighting (Tersoff-Hamann method [1,2]). Because the width of the Gaussian is somewhat arbitrary, we have chosen instead to sum over the LDOS from the Fermi level to the applied sample bias (-0.3 V), which does not require any other parameters. The additional benefit of this method is that the states further from the Fermi level are taken into account more appropriately.

Figure 3.6 shows simulated STM images of the 100%S, 50%S and 50%S-50%H structures. From Figure 3.6a, it is clear that the LDOS at the edge of the particle strongly deviates from the atomic arrangement for the 100%S structure. Hence, in the STM images for this structure the edge S atoms will appear not to follow the lattice of the particles' basal plane, even though in reality they do. The 50%S structure shows a similar discrepancy between atomic structure and LDOS (see Figure 3.6b). However, a small fraction of the LDOS remains located around the S edge atoms, resulting in the red protrusions in the image. For a tip with a finite size however, the bright protrusions will dominate the image. Hence, the edge atoms will appear to be in registry with the basal plane S atoms.

For the case of the 50%S-50%H structure in Figure 3.6c, the situation is less clear. Some of the protrusions on the edge are in registry with the basal plane, while others are not. At elevated temperatures, the H-atoms on the edge will diffuse at high rates, because the diffusion barrier is only 0.56 eV (obtained for unsupported MoS₂). Therefore, a time average of Figure 3.6c would be observed in STM. In such a time average, the brightest protrusion will typically dominate the observed structure due to the exponential character of the tunneling current as a function of tip-surface distance. In the case of the 50%S-50%H structure, the brightest protrusion appears in registry with the basal plane. Therefore, the 50%S-50%H structure will appear similar to the 50%S structure, although with significantly less corrugation along the edge.

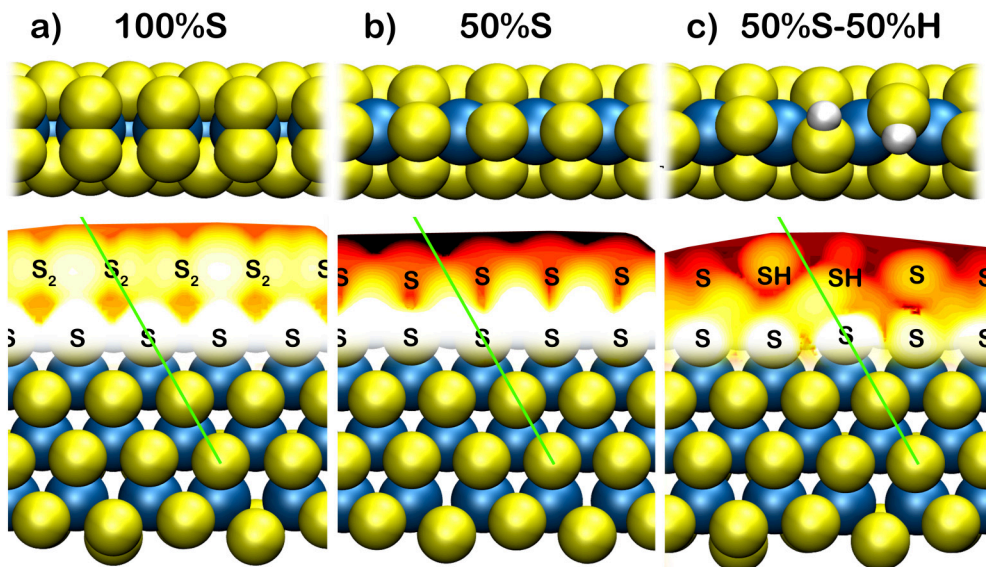


Figure 3.6: Simulated STM images of a) the 100%S structure, b) the 50%S structure and c) the 50%S-50%H structure, for $U_s = -0.3$ V and at a countour value of 1×10^{-5} AU. The green lines facilitate comparison of the registry of the edge protrusions with respect to the basal plane S atoms.

As noted in the main text, Bruix *et al.* obtained a different result for the appearance of the 50%S edge[3]. We identify two possible explanations. First, they used the Tersoff-Hamann method for the calculation of the LDOS around the Fermi level. As pointed out by Bollinger *et al.*, who found a result in agreement with ours, the choice of the Gaussian width is very sensitive in the particular case of MoS₂ due to its semiconducting properties[2]. Hence, the discrepancy between the different authors may be explained due to a different choice for this parameter. A second explanation may be a different placement of MoS₂ on the Au support. If we remove the gold in our calculations, the registry shift in the 50%S structure vanishes. Hence, the details of the MoS₂-Au interaction may be decisive in the obtained results.

3.6 Effect of the Au support on the relative stability of MoS₂ edge structures

To assess the influence of the Au(111) support on the relative stability of MoS₂ edge structures, phase diagrams were computed with and without Au(111) support, as shown in Figure 3.7. Clearly, gold-supported MoS₂ favors higher edge sulfur coverage than its unsupported counterpart. Nonetheless, Au(111) is considered a weakly interacting support[4] since it does not significantly change the edge structures. In contrast, oxide supports like TiO₂ and Al₂O₃ are thought to make oxygen linkages at the particle edges[4-6].

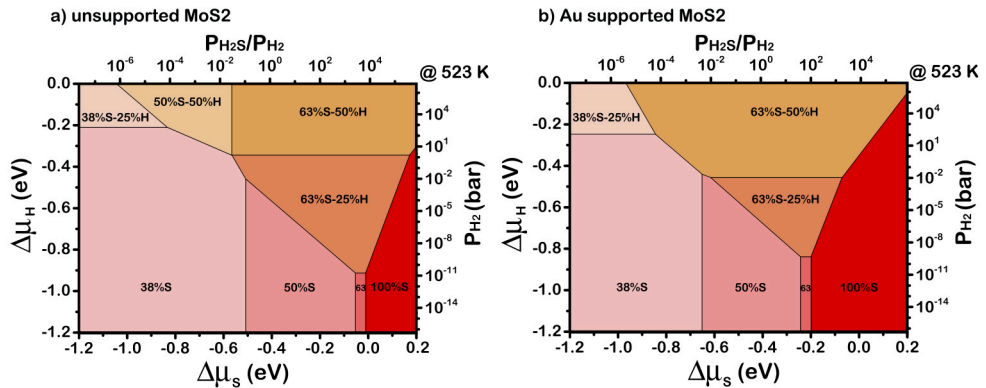


Figure 3.7: *Ab initio* thermodynamics phase diagrams of the MoS₂ edge structure in H₂/H₂S mixtures. a) Unsupported MoS₂. b) Au-supported MoS₂.

3.7 Comparison of the calculations to literature

To establish the validity of our calculations, we compared our results to those reported in the literature. We note that in all previously published phase diagrams, the sulfur chemical potential was referenced against various sulfur structures. This leads to a somewhat arbitrary offset with respect to our chemical potential. Based on the conversion to pressure (ratio) at specific temperatures mentioned in the respective articles, we estimate this offset to be -0.1 eV for Bollinger *et al.*[2] and Lauritsen *et al.*[7], -0.23 eV for Prodhomme *et al.*[8], and -4.15 eV for Cristol *et al.*[9]. Using these offsets, we constructed the comparison in Table 3.1. From these results, it is clear that the relative energies of various edge structures are reproduced relatively well, independent of the differences in methods or unit cell.

Table 3.1: Relative stability of 50%S and 100%S structures

Authors	$\Delta\mu_{\text{H-50S}_{\text{unsupported}}_{\text{50S-50H}}}$	$\Delta\mu_{\text{H-50S}_{\text{Au supported}}_{\text{50S-50H}}}$	$\Delta\mu_{\text{S-50S}_{\text{unsupported}}_{\text{100S}}}$	$\Delta\mu_{\text{S-50S}_{\text{Au supported}}_{\text{100S}}}$
Present	-0.37 eV	-0.30 eV	-0.02 eV	-0.21 eV
Bollinger <i>et al.</i> [2]	-0.30 eV		-0.11 eV	
Lauritsen <i>et al.</i> [7]		-0.30 eV		-0.33 eV
Prodhomme <i>et al.</i> [8]	-0.35 eV			
Cristol <i>et al.</i> [9]			0.01 eV	

3.8 CH₃SH adsorption on MoS₂

The adsorption energy of CH₃SH on Au-supported MoS₂ was calculated for a coverage of 1 molecule per 4 Mo edge atoms. For the calculation of the free energy of adsorption, entropic contributions were included using the reaction conditions in the

STM experiment ($P_{\text{CH}_3\text{SH}} = 0.1$ bar, $P_{\text{H}_2\text{S}} = \sim 0.001$ bar, $P_{\text{H}_2} = 0.9$ bar, 523 K). The formation energy of the adsorption structures was referenced against the most stable structure in the absence of CH_3SH , namely 63%S-50%H.

Table 3.2: Energetics of CH_3SH adsorption on MoS_2

Structure	E_{ads}	ΔG_{ads}	ΔG_{form}
37%S	-1.62 eV	-0.13 eV	-0.08 eV
50%S-50%H	-1.28 eV	0.21 eV	0.44 eV
87%S	-0.46 eV	1.03 eV	2.90 eV

References

- [1] J. Tersoff, D.R. Hamann, Theory of the scanning tunneling microscope, *Phys. Rev. B.* 31 (1985) 805–813.
- [2] M. V. Bollinger, K.W. Jacobsen, J.K. Nørskov, Atomic and electronic structure of MoS_2 nanoparticles, *Phys. Rev. B.* 67 (2003) 085410.
- [3] A. Bruix, H.G. Führtbauer, A.K. Tuxen, A.S. Walton, M. Andersen, S. Porsgaard, F. Besenbacher, B. Hammer, J. V Lauritsen, In Situ Detection of Active Edge Sites in Single-Layer MoS_2 Catalysts, *ACS Nano.* 9 (2015) 9322–9330.
- [4] A.S. Walton, J. V. Lauritsen, H. Topsøe, F. Besenbacher, MoS_2 nanoparticle morphologies in hydrodesulfurization catalysis studied by scanning tunneling microscopy, *J. Catal.* 308 (2013) 306–318. doi:10.1016/j.jcat.2013.08.017.
- [5] B. Hinnemann, J.K. Nørskov, H. Topsøe, A density functional study of the chemical differences between Type I and Type II MoS_2 -based structures in hydrotreating catalysts., *J. Phys. Chem. B.* 109 (2005) 2245–53.
- [6] N. Topsøe, H. Topsøe, FTIR studies of $\text{Mo}/\text{Al}_2\text{O}_3$ based catalysis. I.Morphology and Structure of Calcined and Sulfided Catalysts, *J. Catal.* 139 (1993) 631 – 640.
- [7] J. V. Lauritsen, M. V. Bollinger, E. Lægsgaard, K.W. Jacobsen, J.K. Nørskov, B.S. Clausen, H. Topsøe, F. Besenbacher, Atomic-scale insight into structure and morphology changes of MoS_2 nanoclusters in hydrotreating catalysts, *J. Catal.* 221 (2004) 510–522.
- [8] P.Y. Prodhomme, P. Raybaud, H. Toulhoat, Free-energy profiles along reduction pathways of MoS_2 M-edge and S-edge by dihydrogen: A first-principles study, *J. Catal.* 280 (2011) 178–195.
- [9] S. Cristol, J.F. Paul, E. Payen, D. Bougeard, S. Clémendot, F. Hutschka, Theoretical Study of the $\text{MoS}_2(100)$ Surface: A Chemical Potential Analysis of Sulfur and Hydrogen Coverage, *J. Phys. Chem. B.* 106 (2002) 5659–5667.

Chapter 4

The growth and stability of Au surface oxides on $\text{WO}_3/\text{Au}(111)$ and $\text{ReO}_3/\text{Au}(111)$ inverse model catalysts

Oxide-supported gold catalysts enable oxidation reactions at mild temperatures, providing a unique set of pathways for green chemistry. To investigate whether Au surface oxides may play a role in the catalysis, we studied their autocatalytic formation and stability on $\text{WO}_3/\text{Au}(111)$ and $\text{ReO}_3/\text{Au}(111)$ inverse model catalysts. We find that Au surface oxides are thermodynamically stable over a wide range of catalytically relevant conditions. The formation of the surface oxides requires initial seeds of AuO_x on our model catalysts, but proceeds autocatalytically from there on, with an O_2 dissociation barrier that is mainly entropic.

4.1 Introduction

Despite its reputation as an inert metal, oxide-supported gold has the unparalleled ability to catalyze oxidation reactions at room temperature[1]. This gives Au-based catalysts great potential for applications in a.o. automotive catalysis[1], the pharmaceutical industry[2], and biorefineries[3]. Nonetheless, commercialization of Au catalysts has proven difficult due to their high cost and poor stability[4]. It is vital therefore to capture the essence of the current-day Au catalysts as a design parameter in future development.

The search for the essential features that give oxide-supported Au its tremendous activity has shown that many factors can play a role, depending on the type of catalyst and the employed conditions. Examples include the Au particle size[5–9], the presence of cationic Au[10–15], the particle-support interaction[9,10,16], and the water concentration in the feed[9,17,18].

To unravel the underlying principles that determine the importance of these factors, a vast number of mechanistic studies has emerged, predominantly focused on the oxidation of CO. It is generally agreed that CO adsorbs on the Au particles[5,12,13,19,20]. Oxygen activation is often modeled as adsorption at the gold-support perimeter in the form of molecular[21–24] or support lattice oxygen[25,26], which subsequently reacts with CO. Such models are supported by the observation that the CO oxidation activity scales linearly with the number of perimeter sites[17,26].

However, there is increasing evidence suggesting that gold can play a more extensive role in storing and dissociating oxygen. Fujitani *et al.*[17] showed that the linear scaling with perimeter sites breaks down at slightly elevated temperatures for Au/TiO₂ catalysts. Instead, the observed reactivity scaled with the total number of Au surface sites, suggesting that oxygen is distributed over the entire surface of the Au particles. Indeed, density functional theory (DFT) calculations indicate that the formation of Au surface oxides on both the Au-gas[27–30] and Au-support interface[12,13,31] are thermodynamically favorable in an oxygen atmosphere. Furthermore, it was shown that Au surface oxides catalyze oxygen dissociation[32]. Spectroscopic studies confirm the existence of oxidized Au species in supported Au catalysts[10,11,14,33,34], yet leave their nature and catalytic role unclear. Specifically, it is unclear whether Au oxides are formed at the gas-Au interface or only at the Au-support interface, where they may reside as mere spectator species.

Here, we investigate the autocatalytic formation and thermodynamic stability of Au surface oxides at the gas-Au interface on WO₃/Au(111) and ReO₃/Au(111) inverse model catalysts. In contrast to practical catalysts, these inverted models have the oxides present in nanoparticle form and gold as the support. This allows us to specifically study surface oxides on the dominant surface orientation of Au

nanoparticles, (111), and their interaction with oxide materials. Using scanning tunneling microscopy (STM) and X-ray photoelectron spectroscopy (XPS), we studied Au oxide formation in O₂ pressures of 10⁻⁵ mbar to 500 mbar at temperatures up to 423 K. We find that WO₃ and ReO₃ have a minor effect on the behavior of AuO_x. The stability and reaction kinetics of the surface oxides are analyzed in terms of simple thermodynamic considerations.

4.2 Methods

To study the WO₃/Au(111) and ReO₃/Au(111) catalysts both in ultrahigh vacuum (UHV) and at elevated pressures, we used the ReactorSTM[35] developed in our group. With its high-pressure flow cell inside a UHV system, it allows us to prepare and characterize model catalysts in vacuum and subsequently expose the surface to a controlled high-pressure environment without air exposure. When the reactor seal is removed, the STM can be operated in UHV for vacuum studies. The system is also equipped with a commercial photoelectron spectrometer (SPECS Phoibos) for XPS analysis.

4.2.1 Model catalyst preparation

Clean, atomically smooth Au(111) was prepared by cycles of 1 keV Ar⁺ bombardment and annealing at 900 K. The cleanliness of the surface was confirmed by STM and XPS. The WO₃ and ReO₃ were deposited on the support by reactive evaporation using an e-beam evaporator (Oxford Applied Research). To accomplish this, a rod of the respective metal was held at approximately 1100 K during exposure to 1x10⁻⁵ mbar O₂, creating volatile oxides (see Ref. [36] for more details on this method).

4.2.2 Generation of Au oxide precoverage

While O₂ dissociation faces large energy barriers on Au(111)[37], Au surface oxides readily form when strong oxidizing agents are used, such as electron stimulated NO₂[38] and ozone[39]. We chose to generate small amounts of atomic oxygen using a thoriated iridium filament in 1x10⁻⁵ mbar O₂. At its working temperature of approximately 1750 K, thoriated iridium provides a very low O₂ dissociation rate, thus allowing for a controlled experiment where the vast majority of the surface oxide is formed via O₂ dissociation on AuO_x seeds.

4.2.3 XPS analysis

XPS measurements were carried out in UHV with the X-ray incidence angle at 54° off normal and electron collection along the surface normal. After a Tougaard background subtraction, the Re 4f and O 1s spectra were fitted with the Gaussian/Lorentzian curves implemented in the CasaXPS[40] software package. A Shirley background subtraction was used for the Au 4f spectra. Re and O coverages, expressed in monolayers with the packing

density of Au(111), were calculated based on the Re 4f/Au 4f and O 1s/Au 4f intensity ratios using:

$$\theta_{Re} = \frac{I_{Re}}{I_{Au}} \cdot \frac{RSF_{Au-4f}}{RSF_{Re-4f}} \cdot \frac{1}{1 - e^{-d_{111}/\lambda}} \quad (4.1)$$

$$\theta_O = \frac{I_O}{I_{Au}} \cdot \frac{RSF_{Au-4f}}{RSF_{O-1s}} \cdot \frac{1}{1 - e^{-d_{111}/\lambda}} \quad (4.2)$$

In equations 4.1 and 4.2, I_x is the measured XPS intensity of the respective element, RSF_x the relative sensitivity factor of the probed transition[40], d_{111} the Au(111) layer spacing, and λ the attenuation length of Au 4f photoelectrons in Au[41]. To establish the equations, we have assumed that the Re and O atoms on the surface do not attenuate the Au 4f signal. The last term in equations 4.1 and 4.2 gives the effective number of Au monolayers that is probed in the Au 4f spectrum, thus compensating for the fact that XPS probes deeper than the first layer of the Au(111) surface.

4.3 Results and discussion

We first investigated the structure of WO_3 and ReO_3 on a clean Au(111) sample. After deposition at room temperature, WO_3 adopts an amorphous island structure (see Figure 4.1a). Depending on the state of the STM tip, the apparent height of the islands can be both positive and negative. ReO_3 adopts the same structure as WO_3 (not shown), which is not surprising in view of their chemical similarity. The persistence of the herringbone reconstruction of the Au(111) substrate[42] during WO_3 and ReO_3 deposition, which is performed in 1×10^{-5} mbar O_2 , shows that neither of these oxides is able to catalyze the formation of Au oxides. As both WO_3 and ReO_3 are well-known oxidation catalysts, this is likely due to their inability to transfer oxygen atoms from the oxide to the Au surface rather than to ineffective O_2 dissociation.

When the WO_3 /Au(111) sample is annealed at 527 K, the oxide islands crystallize (see Figure 4.1b). The structure consists of paired rows with a periodicity of 1.6 nm, indicating a large unit cell. This is likely the result of a lattice mismatch between the tungsten oxide and the Au(111) substrate. The amount of oxide on the surface was strongly reduced during the annealing. Meanwhile dark stains appeared in the Au terraces, indicating surface alloying (see Figure 4.1b and Figure 4.7 in the Supporting Information). This highlights the reducible nature of WO_3 when in contact with gold.

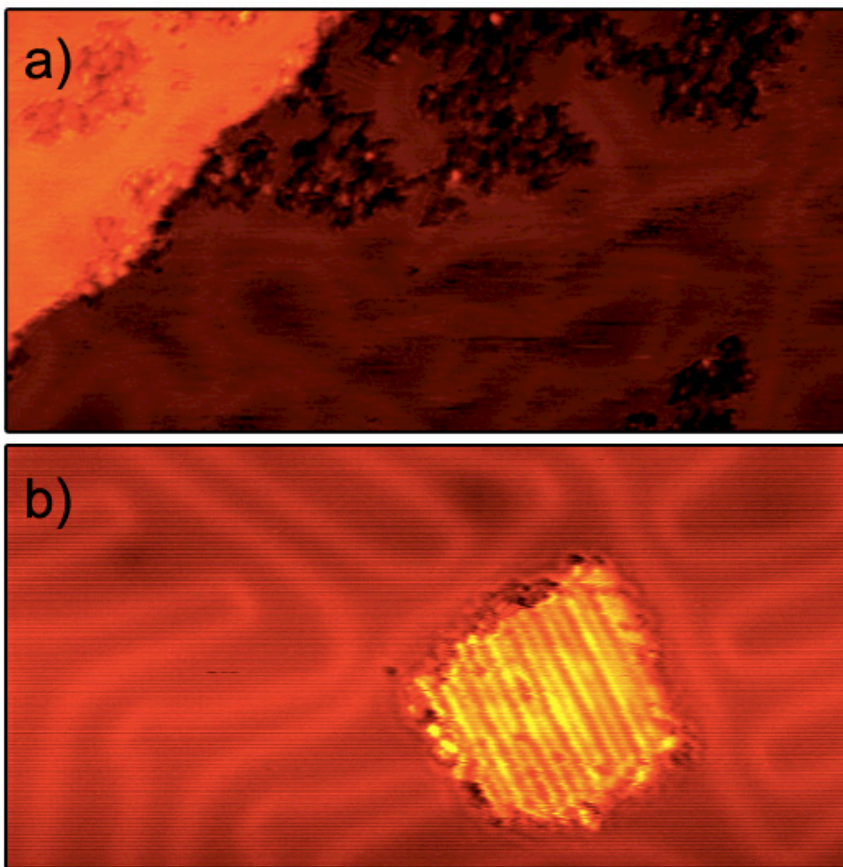


Figure 4.1: WO_3 deposited on Au(111). a) As deposited at room temperature. 70 nm x 35 nm, $U_s = 1.5$ V, $I_t = -120$ pA. b) After annealing at 567 K. Notice the vague dark stains in the herringbone reconstruction at the top of the image, which indicate surface alloying. 40 nm x 20 nm, $U_s = 2$ V, $I_t = -95$ pA.

4.3.1 Disordered surface oxide

At room temperature, exposing $\text{WO}_3/\text{Au}(111)$ and $\text{ReO}_3/\text{Au}(111)$ to a 1×10^{-5} mbar $\text{O}_2/\text{atomic O}$ mixture generates disordered structures (see Figure 4.2). After 15 minutes of exposure, XPS indicates an oxygen coverage of 0.23 ML on a 0.012 ML $\text{ReO}_3/\text{Au}(111)$ sample. This should be considered as a lower bound due to X-ray induced desorption (see Figure 4.8 in the Supporting Information). Similar to observations after NO_2 or O_3 dosing[38,39], the STM images in Figure 4.2 indicate a highly corroded Au surface, implying that Au adatoms were recruited from the terraces to be incorporated into a surface oxide. Both WO_3 and ReO_3 dissolve into the surface oxide, without clearly affecting its structure. This is corroborated by the position of the O 1s peak (529.7 eV), which is unchanged with respect to pure O/Au(111) prepared at room temperature[38].

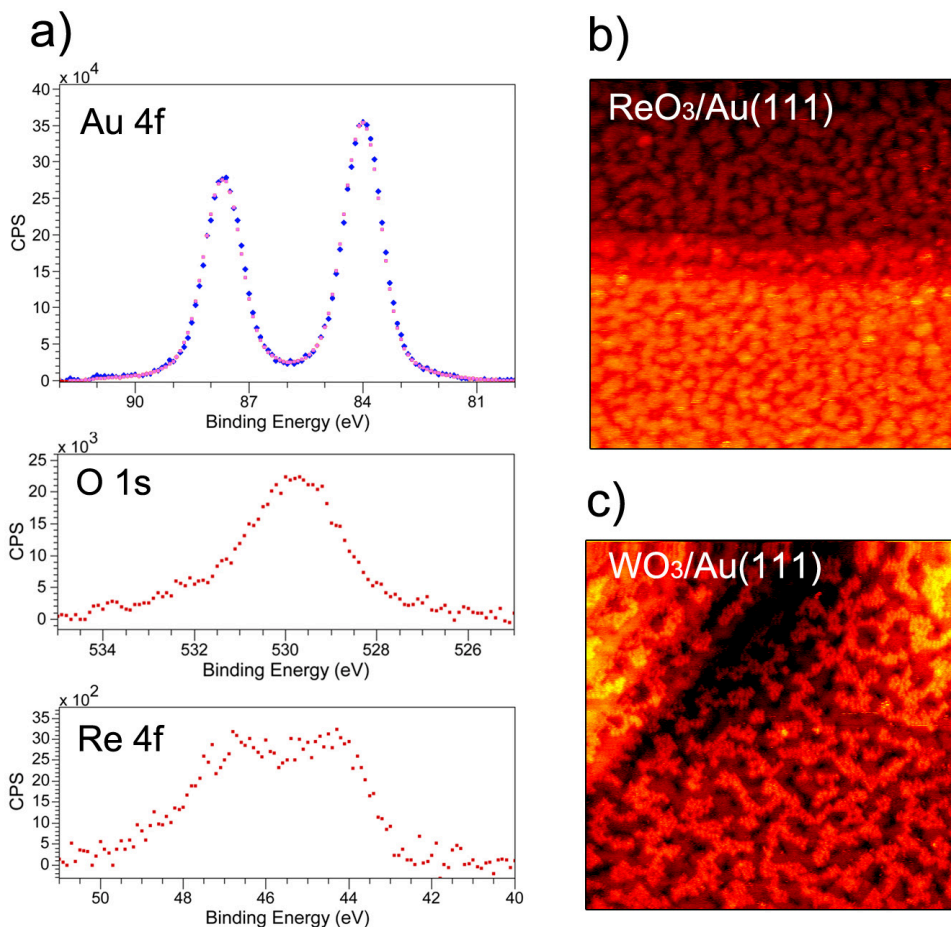


Figure 4.2: XPS and STM data of ReO₃/Au(111) and WO₃/Au(111) after exposure to 1×10^{-5} mbar O₂/O at room temperature. a) Background-subtracted XPS spectra of ReO₃/Au(111) (red) and clean Au(111) (blue). The intensities of the Au 4f spectra of clean Au(111) and ReO₃/Au(111) where set equal at the 4f_{7/2} peak. b) STM image of ReO₃/Au(111) 80 nm x 80 nm, U_s = -1V, I_t = 35 pA. c) STM image of WO₃/Au(111) 80 nm x 80 nm, U_s = -1V, I_t = 35 pA.

The Au 4f spectrum in 4.2 shows no sign of oxidized Au, which would appear as a small shoulder on the higher binding energy side of the metallic Au peak. This is similar to the case of sulfur adsorption on Au(111), where Au adatom incorporation also leaves the Au oxidation state unchanged[38,43]. Hence, whether one assigns the observed structure to a surface oxide or to an oxygen-induced reconstruction is a matter of definition. It should however be clear that the structure observed in Figure 4.2 is distinctly different from the weak chemisorption of oxygen on the perfect Au(111) surface[5,29].

The observation that surface oxides at the Au-gas interface need not contain detectably oxidized Au has important consequences for the interpretation of spectroscopic data of Au catalysts. XPS or X-ray absorption spectra on Au transitions alone may not tell the full story. Furthermore, the beam damage after exposure to weak lab source X-rays suggests that the surface oxides may decompose abruptly under synchrotron X-ray irradiation. For vibrational spectroscopy, it is also uncertain whether the Au surface oxide has a sufficiently distinct chemical nature with respect to bare Au to allow for resolved CO vibration peaks. These considerations highlight the importance of direct observations on well-defined CO oxidation catalysts that allow for unambiguous assignment of catalytic intermediates.

4.3.2 Surface oxide in 500 mbar O₂

To investigate the behavior of the gold surface oxides under catalytically relevant pressures, we exposed WO₃/Au(111) and ReO₃/Au(111) catalysts with a small initial Au oxide coverage to oxygen pressures up to 500 mbar. Figure 4.3a shows ReO₃/Au(111) during exposure to 500 mbar O₂. The streaky appearance of the surface indicates fast surface dynamics. This implies that there is no densely packed crystalline surface oxide phase on the Au terraces, but rather disordered Au oxide structures that can assemble and disassemble with high rates.

Over time, islands with rod shapes appear on the surface (see Figures 3 and S3 in the Supporting Information), showing that the high-pressure conditions facilitate the formation of a new phase with respect to the vacuum situation described in the previous section. The islands crystallize further when left in vacuum after the high-pressure exposure. Figures 3b and c show the resulting structure, which appears to be identical to the one observed on Au(111) after ozone treatment at 400K[39]. At room temperature, such an ozone treatment yields a disordered structure similar to Figures 2b and c. Hence, the main effect induced by high pressure is the increase in mobility of oxygen-containing species.

The preparation process of the initial AuO_x seeds prior to the high-pressure experiment created vacancy islands in the Au terraces. These vacancy islands remain when the surface is left in vacuum for 24 hours. However, during the high-pressure exposure the density of vacancy islands clearly decreases within 2 hours (see Figures 4.9 and 4.10 in the Supporting Information). Meanwhile, the total area of the vacancy islands appears to remain constant, although this was difficult to quantify due to the streaky character of the images (standard deviation: ±37%). We conclude that the high-pressure conditions induce accelerated ripening.

The observation of a constant total vacancy island area suggests that the dynamic species on the Au terraces do not contain Au adatoms. This is corroborated by the observation that no new vacancy islands are formed, which did occur at lower O₂ pressure at room temperature (see previous section). Since the rod shaped Au oxide islands can only communicate with the vacancy islands and step edges via the

dynamic species on the terraces, we conclude that the Au oxide islands also do not contain Au adatoms.

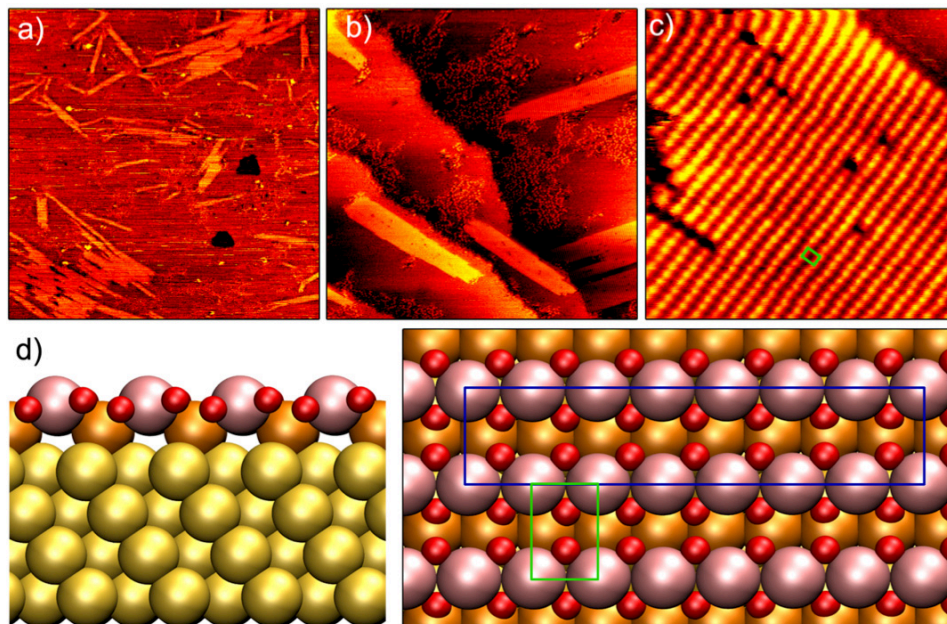


Figure 4.3: Au surface oxide formed on $\text{ReO}_3/\text{Au}(111)$ in 500 mbar O_2 at room temperature. a) *In situ* image, 160 nm x 160 nm, $U_s = 2$ V, $I_t = -120$ pA. b) Image after crystallization in UHV for 17 hours, 80 nm x 80 nm, $U_s = 1$ V, $I_t = -100$ pA. c) High-resolution image of the structure in panel b, 10 nm x 10 nm, $U_s = 0.42$ V, $I_t = -200$ pA. The green rectangle indicates the observed unit cell d) Proposed structure of the Au surface oxide. Left: cross sectional view, parallel to the lifted Au rows. Right: top view, in which the lifted Au rows run from left to right. The unit cell is indicated in blue, while green indicates the local unit cell that is primarily observed in the experiment. Bulk Au, interface Au, oxidic Au, and O atoms are colored gold, orange, pink, and red, respectively.

The Au oxide islands shown in Figure 4.3 have a 0.49 ± 0.02 nm x 0.33 ± 0.007 nm rectangular unit cell with its short axis lying along the close-packed direction of the Au surface. While the long axis of the unit cell fits well with the Au lattice, the short axis is 14% larger than the Au nearest neighbor distance. Due to this mismatch with the Au(111) lattice, one may expect a buckling in the AuO_x islands. On the large-scale image in Figure 4.3b, no such buckling is observed. At the atomic scale in Figure 4.3c however, it is clear that small sideways deviations from the perfect regular lattice occur. The displacements do not appear to follow a completely regular pattern, which could indicate that defects and island edges impose long-range stress in the islands. The measured height of the islands was 0.14 nm, independent of the applied tip-sample bias. This is well below the Au(111) step height of 0.23 nm, which is consistent with the earlier indication that the surface oxide does not contain Au adatoms.

Based on the geometrical arguments above, the Au surface oxide structures proposed in the literature[27,30], and the similarity to the case of Pt(111)[44–47], we propose the structure depicted in Figure 4.3d for the Au oxide islands. In this structure Au atoms are lifted out of the terrace by 4 oxygen atoms, as was also observed in *ab initio* molecular dynamics simulations[27]. Thus, oxide rows are formed, similar to those predicted[44] and observed[46,47] on Pt(111). DFT calculations on a similar structure on Pt(110) showed that the dense packing of oxygen atoms in the oxide rows creates compressive stress, driving the rows to expand along the row direction[48]. This can explain the lattice mismatch of 14% along the row direction observed in our experiments.

The expansion of the Au oxide rows necessitates the expulsion of Au atoms. Based on the observed island coverage, this would amount to 0.5-1% of a monolayer, which is approximately half the vacancy island coverage. One may expect that part of the adatoms are used to fill the vacancy islands, while the rest attaches to step edges. We suggest that the decrease in vacancy island coverage lies within the 37% standard deviation of the measurement.

4.3.3 Low coverage needle oxide

To test the stability of the Au surface oxide, we performed experiments at various temperatures. At 423 K, a crystalline “needle”-shaped Au oxide with a modest coverage is formed during the 1×10^{-5} mbar O_2/O exposure (see Figure 4.4). This result was independent of the exposure time (see Section 4.8 in the Supporting Information), from which we conclude that the needle phase is an equilibrium structure. The WO_3 and ReO_3 islands in Figure 4.4 were deposited at 500 K, resulting in a partially crystalline island structure with a bright appearance.

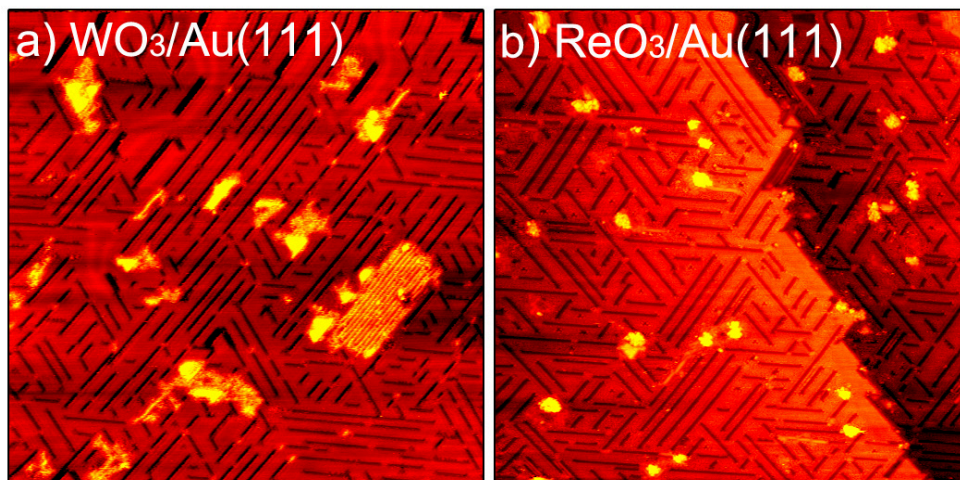


Figure 4.4: $WO_3/Au(111)$ and $ReO_3/Au(111)$ after exposure to 1×10^{-5} mbar O_2 mbar at 423 K. a) $WO_3/Au(111)$ 80 nm x 80 nm, $U_s = 1V$, $I_t = -125$ pA. b) $ReO_3/Au(111)$ 80 nm x 80 nm, $U_s = 2V$, $I_t = -130$ pA.

When left in vacuum at room temperature, the needle phase disappears within approximately 24 hours (see Figure 4.5). This disappearance is not observed for the disordered Au oxide, nor for the Au oxide islands. Hence, the barrier for desorption must be lower for the needle structure, indicating that it is either less stable, or more active in catalyzing O_2 adsorption/desorption.

The needles shown in Figure 4.4 follow the close-packed directions of the Au(111) lattice and occur as single or double oxide rows. Similarly, for Pt(111) it was shown that at intermediate coverage the oxide rows form a honeycomb network of single to triple rows[46]. Their proposed structure was almost identical to those in the Au oxide island structure. Therefore, it is tempting to interpret the needles as isolated or paired rows of the island oxide structure. In this case however, there must be a stabilizing force that prevents the oxide rows from assembling into islands. A possible candidate for this would be stress relaxation in the Au surface. Figures 4.4 and 4.5 show that the herringbone reconstruction is lifted in the close vicinity of the oxide needles, but remains elsewhere. Hence, it appears that the oxide needles can relieve compressive stress in the Au surface, similar to the herringbone reconstruction[42]. As a result, there is a driving force for the needles to remain isolated up to the coverage where the herringbone reconstruction is fully lifted.

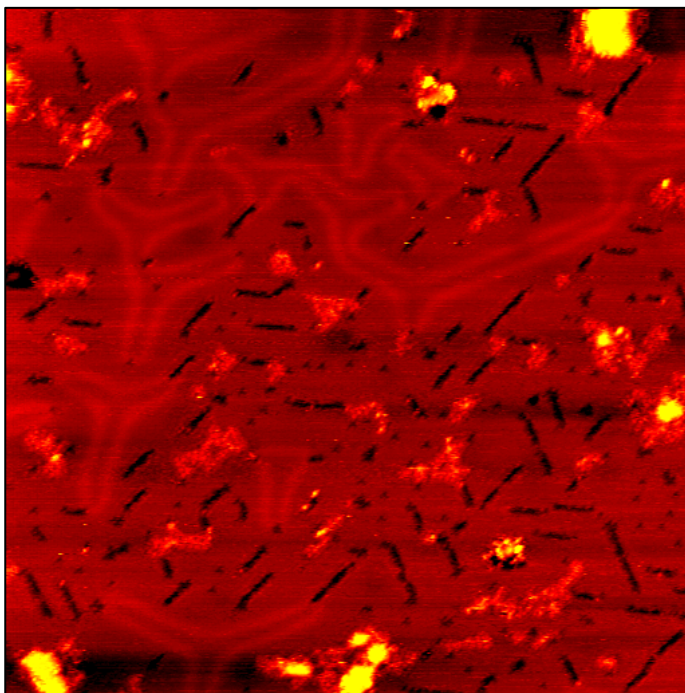


Figure 4.5: Low coverage AuO_x on $WO_3/Au(111)$ after exposure to 1×10^{-5} mbar O_2 mbar at 423 K and 18.5 h in vacuum, 80 nm x 80 nm, $U_s = 2$ V, $I_t = -95$ pA

In Figure 4.4, it appears as if WO_3 and ReO_3 have little effect on the Au needle oxide other than disturbing its long-range order. At low AuO_x coverage however, it becomes clear that the Au surface oxide is stabilized in the vicinity of WO_3 . Figure 4.5 shows that the locations of the two oxides correlate. The correlation is not perfect however, indicating that the stabilization is subtle. Nonetheless, this result suggests that Au oxides may form preferably on the Au-support perimeter in industrial Au catalysts, as was also found in a DFT study on Au nanoparticles on TiO_2 [13].

4.3.4 Energetics of Au surface oxide

O_2/O exposure at temperatures higher than 423 K did not result in oxide growth. Under the assumption that the atomic oxygen did not significantly influence the equilibrium oxygen coverage, one can use this transition temperature between formation and absence of formation of the oxide to estimate the oxide formation enthalpy. At the transition temperature, the free energy of formation is zero. This means that the contributions of the enthalpy (ΔH_{ads}) and entropy ($T\Delta S_{\text{ads}}$) of formation cancel (see Figure 4.6a). Assuming that oxygen loses all entropy upon adsorption, $-\Delta S_{\text{ads}}$ equals the gas phase entropy of oxygen ($S_{\text{O}_2(\text{g})}$). With this assumption, $T\Delta S_{\text{ads}} = -1.6$ eV per O_2 molecule under the applied conditions[49]. Hence, we find a formation enthalpy of the oxide of -1.6 eV per O_2 molecule. This value is corroborated by experiments from Deng *et al.*[32], who showed that oxygen can be adsorbed up to 0.4 ML on O-precovered Au(111) in 1×10^{-7} mbar O_2 at 400 K, which implies the same -1.6 eV formation enthalpy when analyzed using the above arguments. This validates our assumption that the atomic oxygen present in the gas phase during our experiment did not significantly affect the stability range of the Au surface oxide.

The formation enthalpy derived above can be used to determine the stability of surface oxides as a function of temperature and pressure. The Au oxide coverage (θ) can be obtained as a function of temperature (T) and pressure (P) through a Langmuir model[50]:

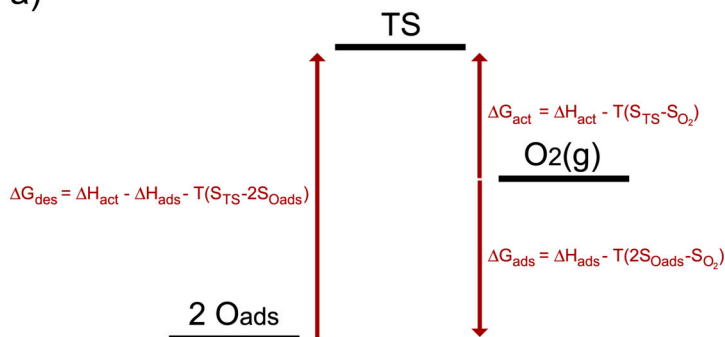
$$\frac{\theta}{\theta_{max}} = \frac{\sqrt{KP}}{\sqrt{KP} + 1} \quad (4.3)$$

$$K = e^{-(\Delta H_{ads} + TS_{\text{O}_2(\text{g})}^0)/k_B T} \quad (4.4)$$

$S_{\text{O}_2(\text{g})}^0$ designates the standard entropy of gaseous O_2 , given at standard pressure (P^0 , 1 bar). Note that we have included the temperature dependence of the standard entropy of gas phase oxygen[49]. We have again assumed that oxygen loses all entropy upon adsorption. Furthermore, we assume that the reaction enthalpy is independent of temperature and coverage.) Figure 4.6b shows the resulting stability diagram. The extrapolation of our vacuum results to catalytically relevant pressures shows that the needle phase should be stable up to around 560 K for 1 mbar O_2 and even to 690 K in 1 bar. Hence, from the thermodynamic point of view Au surface oxides can be expected over the whole range of relevant temperatures for Au-based oxidation catalysis. However, reaction kinetics may play a vital role in determining the actual

oxide coverage under catalytic conditions. Hence, our predictions should serve as a starting point for further investigation.

a)



b)

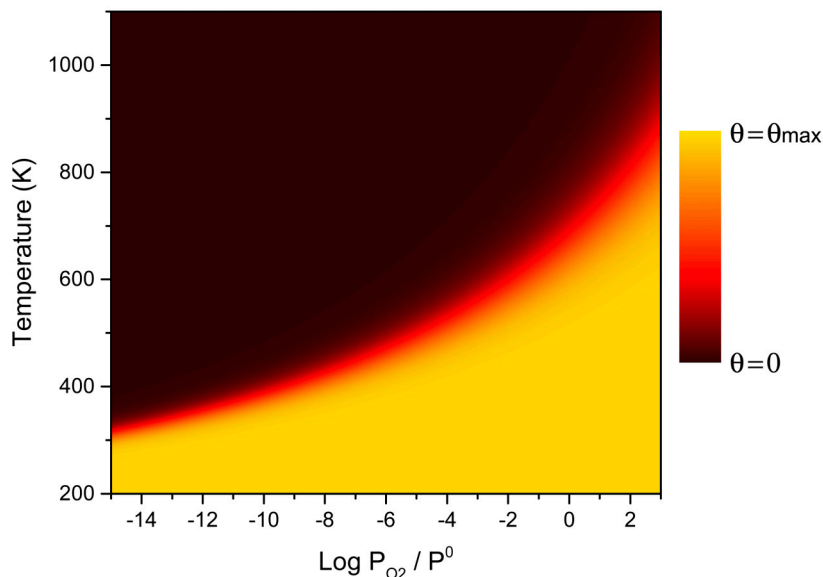


Figure 4.6: a) Components of the free energy of adsorption/desorption. “TS” designates the transition state. b) Stability diagram for the needle type Au surface oxide, based on equations 4.3, 4.4 and the experimentally derived adsorption enthalpy of -1.6 eV/O₂ molecule.

We should stress that the yellow regime in the diagram of Figure 4.6b presents a conservative estimate for the range of thermodynamic stability of surface oxides on Au(111). For the calculation of the reaction enthalpy, we have assumed that the system was in equilibrium. Since the oxygen in the gas phase is at room temperature, whereas the oxygen on the surface is at 423 K, we are actually underestimating the

stability of the oxide somewhat. Furthermore, some oxygen may have been lost during the cooling down of the crystal in vacuum. Moreover, if the assumption of negligible entropy of the adsorbed oxygen was incorrect, one may expect the stability at temperatures above 423 K to be improved, (while at lower temperatures the stability is reduced). Finally, we should point out that there may be Au surface oxide phases that are more stable than those reported here, but that would require the combination of high temperature and high pressure to overcome the kinetic limitations of their formation. Indeed, surface oxides with full coverage have been reported following preparation at 1073 K in 1 bar O₂[51]. As can be seen in Figure 4.6b, the needle phase is not stable under those conditions. This signifies the need to perform high-pressure, high-temperature experiments to further expand our understanding of the stability of Au surface oxides.

The activation barrier for oxygen adsorption via gold oxide can be estimated from a comparison between the oxide formation enthalpy and the desorption free energy barrier (see Figure 4.6a). A value of 1.43 eV was obtained for the latter from temperature programmed desorption (TPD) of oxygen, using the same assumptions we employed above[32]. The desorption temperature in the TPD experiments is not affected by pre-annealing up to 420 K[52], showing that the surface structure is close to equilibrium during the TPD runs. Hence, the desorption barrier found in TPD and the adsorption energy found in the present work relate to the same (equilibrated) state. We can insert the values for the desorption barrier (ΔG_{des}), the adsorption energy (ΔH_{ads}), and the desorption temperature (TPD peak at 550 K) in the following equation (see also Figure 4.6a):

$$\Delta G_{des} = \Delta H_{act} - \Delta H_{ads} - T(S_{TS} - 2S_{Oads}) \quad (4.5)$$

From this, it follows that the enthalpy barrier for adsorption (ΔH_{act}), is calculated as:

$$\Delta H_{act} = 550(S_{TS} - 2S_{Oads}) - 0.17 \quad (4.6)$$

Again, we assume that $S_{Oads} = 0$. Thus, ΔH_{act} only depends on the transition state entropy (S_{TS}). The first order kinetics observed in the TPD experiments[32,52] seem to indicate that the transition state does not correspond to the associative desorption of two oxygen atoms, but rather to the transition of an oxygen atom from the surface oxide to another adsorption state. For such a bound state, one may expect a small entropy (S_{TS}). Since S_{TS} is small, we conclude from Equation 4.6 that the enthalpy barrier for adsorption is also small or negligible. Hence, the free energy barrier for adsorption is mainly entropic. As a result, O₂ adsorption will be very efficient at mild temperatures and elevated pressures.

Although it is clear that Au surface oxides exhibit a strongly autocatalytic growth, one may wonder if a seed can be created on Au-reducible oxide catalysts under industrial conditions. Oxide-supported Au catalysts efficiently dissociate O₂ on the oxide support

or the Au-support perimeter, providing a source of atomic oxygen. It is unclear, however, whether the atomic oxygen can be transferred to the Au particle. For Ca contaminations in Au(111) this does appear to be possible, facilitating the formation of AuO_x using UHV O₂ exposure[53]. Similarly, traces of Ag are thought to aid in the oxidation of Au in nanoporous gold catalysts[54,55]. On the other hand, the present work shows that WO₃ and ReO₃ do not have the required properties to oxidize Au(111), even though they are well-known oxidation catalysts. Biener *et al.* also did not observe AuO_x on a TiO_x/Au(111) catalyst after O₂ exposure[56]. Thus, it seems that specific atomic arrangements are necessary to enable Au surface oxide formation.

Finally, we discuss how the presence of Au surface oxides could affect the overall reaction mechanism for Au-based oxidation catalysis. First, Au oxide provides an alternative pathway for O₂ dissociation besides dissociation on the support or at the Au-support perimeter. Whether or not this new pathway will be dominant, will depend on the amount of Au oxide present and the activity of the other pathways, which varies per type of catalyst. In the case where O₂ dissociation on Au oxide is not the dominant pathway, or when Au oxide is more stable at the Au-support perimeter[13], Au oxide will be predominantly located at the Au-support perimeter. Under such conditions, the reactivity will scale with the number of perimeter sites as was observed in several experiments[17,26]. Au oxide may also provide new sites for the adsorption of CO, which is rather weak on clean gold[19]. Finally, the Au oxide provides a low-energy[39] Mars van Krevelen type pathway for the reaction of CO with oxygen atoms.

4.4 Conclusion

Our results provide new evidence that Au surface oxides at the gas-surface interface of Au oxidation catalysts should be considered as a feasible reaction intermediate in a wide range of relevant temperatures and pressures. The experimentally derived formation enthalpy of -1.6 eV/O₂ molecule implies that surface oxides on Au(111) are thermodynamically stable up to approximately 560 K in 1 mbar O₂ and even up to 690 K in 1 bar. The presence of WO₃ and ReO₃ particles on the Au(111) substrate has little effect on the Au surface oxide structure, although a small attractive interaction was found.

While the Au surface oxides are stable even in low oxygen pressures, we find that WO₃ and ReO₃ are not able to facilitate their initial formation. When AuO_x seeds are provided however, Au surface oxide formation is facile. By comparison to literature temperature programmed desorption results we find that the barrier for O₂ dissociation on Au oxides is modest and predominantly determined by entropic contributions, implying that adsorption will be efficient at mild temperatures and elevated pressures.

Several types of surface oxide can be formed, depending on the employed conditions. In vacuum at room temperature our O_2/O mixture yields a disordered, rough surface. A similar exposure at 423 K yields a one-dimensional needle-type oxide. Experiments at a catalytically relevant pressure of 500 mbar O_2 revealed a highly dynamic surface where islands of a densely packed oxide develop. For the structure of this densely packed phase, we propose a model containing parallel Au oxide chains, analogous to those observed on Pt(111). The variety of observed Au oxide structures highlights their flexible bonding nature, which implies that Au surface oxides are likely not only stable on the (111) surface orientation, but also on other orientations present on Au nanoparticles.

References

- [1] B.K. Min, C.M. Friend, Heterogeneous gold-based catalysis for green chemistry: Low-temperature CO oxidation and propene oxidation, *Chem. Rev.* 107 (2007) 2709–2724.
- [2] M.D. Hughes, Y.J. Xu, P. Jenkins, P. McMorn, P. Landon, D.I. Enache, A.F. Carley, G.A. Attard, G.J. Hutchings, F. King, others, Tunable gold catalysts for selective hydrocarbon oxidation under mild conditions, *Nature.* 437 (2005) 1132–1135.
- [3] C. Della Pina, E. Falletta, M. Rossi, Update on selective oxidation using gold, *Chem. Soc. Rev.* 41 (2012) 350–369.
- [4] R. Ciriminna, E. Falletta, C. Della Pina, H. Teles, M. Pagliaro, Industrial Applications of Gold Catalysis, *Angew. Chemie - Int. Ed.* 55 (2016) 14210–17.
- [5] N. Lopez, J.K. Nørskov, Catalytic CO oxidation by a gold nanoparticle: A density functional study, *J. Am. Chem. Soc.* 124 (2002) 11262–11263.
- [6] G. Mills, M.S. Gordon, H. Metiu, Oxygen adsorption on Au clusters and a rough Au(111) surface: The role of surface flatness, electron confinement, excess electrons, and band gap, *J. Chem. Phys.* 118 (2003) 4198–4205.
- [7] B. Yoon, H. Häkkinen, U. Landman, Interaction of O₂ with Gold Clusters: Molecular and Dissociative Adsorption, *J. Phys. Chem. A.* 107 (2003) 4066–4071.
- [8] M. Valden, S. Pak, X. Lai, D.W. Goodman, Structure sensitivity of CO oxidation over model Au/TiO₂ catalysts, *Catal. Letters.* 56 (1998) 7–10.
- [9] M. Haruta, Spiers Memorial Lecture : Role of perimeter interfaces in catalysis by gold nanoparticles, *Faraday Discuss.* 152 (2011) 11–32.
- [10] A.Y. Klyushin, M.T. Greiner, X. Huang, T. Lunkenbein, X. Li, O. Timpe, M. Friedrich, M. Hävecker, A. Knop-Gericke, R. Schlögl, Is Nanostructuring Sufficient to Get Catalytically Active Au?, *ACS Catal.* 6 (2016) 3372–3380.
- [11] J.C. Fierro-Gonzalez, B.C. Gates, Catalysis by gold dispersed on supports: the importance of cationic gold., *Chem. Soc. Rev.* 37 (2008) 2127–34.
- [12] L.B. Vilhelmsen, Identification of the Catalytic Site at the Interface Perimeter of Au Clusters on Rutile TiO₂(110), *ACS Catal.* 4 (2014) 1626–1631.
- [13] L.B. Vilhelmsen, B. Hammer, Interfacial oxygen under TiO₂ supported Au clusters revealed by a genetic algorithm search, *J. Chem. Phys.* 139 (2013) 204701.
- [14] J.T. Miller, A.J. Kropf, Y. Zha, J.R. Regalbuto, L. Delannoy, C. Louis, E. Bus, J.A. van Bokhoven, The effect of gold particle size on Au{single bond}Au bond length and reactivity toward oxygen in supported catalysts, *J. Catal.* 240 (2006) 222–234.
- [15] S. Minicò, S. Scirè, C. Crisafulli, A.M. Visco, S. Galvagno, FT-IR study of Au/Fe₂O₃ catalysts for CO oxidation at low temperature, *Catal. Letters.* 47 (1997) 273–276.
- [16] M.S. Chen, D.W. Goodman, The structure of catalytically active Au on titania, *Science* 306 (2004) 252–255.
- [17] T. Fujitani, I. Nakamura, Mechanism and active sites of the oxidation of CO over Au/TiO₂, *Angew. Chemie - Int. Ed.* 50 (2011) 10144–10147.
- [18] L.M. Liu, B. Mcallister, H.Q. Ye, P. Hu, Identifying an O₂ Supply Pathway in CO

- Oxidation on Au/TiO₂(110): A Density Functional Theory Study on the Intrinsic Role of Water, *J. Am. Chem. Soc.* 128 (2006) 4017–4022.
- [19] Z. Zeng, J. Greeley, Theoretical study of CO adsorption on Au catalysts under environmental catalytic conditions, *Catal. Commun.* 52 (2014) 78–83.
- [20] H. Hartshorn, C.J. Pursell, B.D. Chandler, Adsorption of CO on Supported Gold Nanoparticle Catalysts: A Comparative Study, *J. Phys. Chem. C.* 113 (2009) 10718–10725.
- [21] T. Yan, D.W. Redman, W.-Y. Yu, D.W. Flaherty, J. a. Rodriguez, C.B. Mullins, CO oxidation on inverse Fe₂O₃/Au(111) model catalysts, *J. Catal.* 294 (2012) 216–222.
- [22] M.M. Schubert, S. Hackenberg, A.C. van Veen, M. Muhler, V. Plzak, R.J. Behm, CO Oxidation over Supported Gold Catalysts—“Inert” and “Active” Support Materials and Their Role for the Oxygen Supply during Reaction, *J. Catal.* 197 (2001) 113–122.
- [23] Y. Chen, P. Crawford, P. Hu, Recent advances in understanding CO oxidation on gold nanoparticles using density functional theory, *Catal. Letters.* 119 (2007) 21–28.
- [24] H. Koga, K. Tada, M. Okumura, Chemical Physics Letters DFT study of CO oxidation over Au/TiO₂(110): The extent of the reactive perimeter zone, *Chem. Phys. Lett.* 610–611 (2014) 76–81.
- [25] G.C. Bond, D.T. Thompson, Gold-Catalysed Oxidation of Carbon Monoxide, *Gold Bull.* 33 (2000) 41–50.
- [26] M. Kotobuki, R. Leppelt, D.A. Hansgen, D. Widmann, R.J. Behm, Reactive oxygen on a Au/TiO₂ supported catalyst, *J. Catal.* 264 (2009) 67–76.
- [27] T.A. Baker, B. Xu, X. Liu, E. Kaxiras, C.M. Friend, Nature of Oxidation of the Au (111) Surface : Experimental and Theoretical Investigation, *J. Phys. Chem. C Lett.* 113 (2009) 16561–16564.
- [28] T.A. Baker, C.M. Friend, E. Kaxiras, Effects of chlorine and oxygen coverage on the structure of the Au(111) surface, *J. Chem. Phys.* 130 (2009) 084701.
- [29] H. Shi, C. Stampfl, First-principles investigations of the structure and stability of oxygen adsorption and surface oxide formation at Au(111), *Phys. Rev. B.* 76 (2007) 075327.
- [30] K. Sun, M. Kohyama, S. Tanaka, S. Takeda, Structures and stabilities of gold oxide films on gold surfaces in O₂ atmosphere, *Surf. Sci.* 628 (2014) 41–49.
- [31] Z. Duan, G. Henkelman, CO oxidation at the Au/TiO₂ boundary: The role of the Au/Ti5c site, *ACS Catal.* 5 (2015) 1589–95.
- [32] X. Deng, B.K. Min, A. Guloy, C.M. Friend, Enhancement of O₂ Dissociation on Au (111) by Adsorbed Oxygen : Implications for Oxidation Catalysis, *J. Am. Chem. Soc.* 127 (2005) 9267–9270.
- [33] V. Schwartz, D.R. Mullins, W. Yan, B. Chen, S. Dai, S.H. Overbury, XAS Study of Au Supported on TiO₂ : Influence of Oxidation State and Particle Size on the Catalytic Activity, *J. Phys. Chem. B.* 108 (2004) 15782–15790.
- [34] P. Jiang, S. Porsgaard, F. Borondics, M. Kober, A. Caballero, H. Bluhm, F. Besenbacher, M. Salmero, Room-temperature reaction of oxygen with gold: An in situ ambient-pressure x-ray photoelectron spectroscopy investigation, *J.*

- Am. Chem. Soc. 132 (2010) 2858–2859.
- [35] C.T. Herbschleb, P.C. van der Tuijn, S.B. Roobol, V. Navarro, J.W. Bakker, Q. Liu, D. Stoltz, M.E. Cañas-Ventura, G. Verdoes, M.A. van Spronsen, M. Bergman, L. Crama, I. Taminiou, A. Ofitserov, G.J.C. van Baarle, J.W.M. Frenken, The ReactorSTM: atomically resolved scanning tunneling microscopy under high-pressure, high-temperature catalytic reaction conditions., *Rev. Sci. Instrum.* 85 (2014) 083703.
- [36] R. V. Mom, M.J. Rost, J.W.M. Frenken, I.M.N. Groot, Tuning the Properties of Molybdenum Oxide on Al₂O₃/NiAl(110): Metal versus Oxide Deposition, *J. Phys. Chem. C.* 120 (2016) 19737–19743.
- [37] Z.P. Liu, P. Hu, A. Alavi, Catalytic role of gold in gold-based catalysts: A density functional theory study on the CO oxidation on gold, *J. Am. Chem. Soc.* 124 (2002) 14770–14779.
- [38] B.K. Min, A.R. Alemozafar, M.M. Biener, J. Biener, C.M. Friend, Reaction of Au(111) with Sulfur and Oxygen: Scanning Tunneling Microscopic Study, *Top. Catal.* 36 (2005) 77–90.
- [39] B.K. Min, A.R. Alemozafar, D. Pinnaduwege, X. Deng, C.M. Friend, Efficient CO Oxidation at Low Temperature on Au(111), *J. Phys. Chem. B.* 110 (2006) 19833–19838.
- [40] N. Fairley, CasaXPS 2.3, (1999). www.casaxps.com.
- [41] P.J. Cumpson, M.P. Seah, Elastic Scattering Corrections in AES and XPS. II. Estimating Attenuation Lengths and Conditions Required for their Valid Use in Overlayer/Substrate Experiments, *Surf. Interface Anal.* 25 (1997) 430–446.
- [42] J.V. V. Barth, H. Brune, G. Ertl, R.J. Behm, Scanning tunneling microscopy observations on the reconstructed Au(111) surface: atomic structure, long-range superstructure, rotational domains, and surface defects, *Phys. Rev. B.* 42 (1990) 9307–9318.
- [43] P.G. Lusteinberg, C. Vericat, G.A. Benitez, M.E. Vela, N. Tognalli, A. Fainstein, M.L. Martiarena, R.C. Salvarezza, Spontaneously formed sulfur adlayers on gold in electrolyte solutions: Adsorbed sulfur or gold sulfide?, *J. Phys. Chem. C.* 112 (2008) 11394–11402.
- [44] J.M. Hawkins, J.F. Weaver, A. Asthagiri, Density functional theory study of the initial oxidation of the Pt(111) surface, *Phys. Rev. B.* 79 (2009) 125434.
- [45] D.J. Miller, H. Øberg, S. Kaya, H. Sanchez Casalongue, D. Friebe, T. Anniyev, H. Ogasawara, H. Bluhm, L.G.M. Pettersson, A. Nilsson, Oxidation of Pt(111) under near-ambient conditions, *Phys. Rev. Lett.* 107 (2011) 195502.
- [46] S.P. Devarajan, J.A. Hinojosa, J.F. Weaver, STM study of high-coverage structures of atomic oxygen on Pt(111): p(2x1) and Pt oxide chain structures, *Surf. Sci.* 602 (2008) 3116–3124.
- [47] M.A. van Spronsen, Oxidation catalysis on Pt and Au, Leiden University, 2016.
- [48] T.M. Pedersen, W. Xue Li, B. Hammer, Structure and activity of oxidized Pt(110) and alpha-PtO₂, *Phys. Chem. Chem. Phys.* 8 (2006) 1566–74.
- [49] NIST, Computational Chemistry Comparison and Benchmark Database, (2016). <http://cccbdb.nist.gov/>.
- [50] H. Ibach, *Physics of Surfaces and Interfaces*, Springer, Berlin, 2006.

- [51] L. Huang, P. Zeppenfeld, J. Chevrier, G. Comsa, Surface morphology of Au(111) after exposure to oxygen at high temperature and pressure, *Surf. Sci.* 352-354 (1996) 285–289.
- [52] R.A. Ojifinni, J. Gong, D.W. Flaherty, T.S. Kim, C.B. Mullins, Annealing effect on reactivity of Oxygen-Covered Au(111), *J. Phys. Chem. C.* 113 (2009) 9820–9825.
- [53] M. E. Schrader, Chemisorption of oxygen to gold: AES study of catalytic effect of calcium, *Surf. Sci.* 78 (1978) L227–L232.
- [54] J. Biener, M.M. Biener, R.J. Madix, C.M. Friend, Nanoporous Gold: Understanding the Origin of the Reactivity of a 21st Century Catalyst Made by Pre-Columbian Technology, *ACS Catal.* 5 (2015) 6263–6270.
- [55] L. V. Moskaleva, T. Weiss, T. Klüner, M. Bäumer, Chemisorbed Oxygen on the Au(321) Surface Alloyed with Silver: A First-Principles Investigation, *J. Phys. Chem. C.* 119 (2015) 9215–9226.
- [56] J. Biener, E. Farfan-Arribas, M. Biener, C.M. Friend, R.J. Madix, Synthesis of TiO₂ nanoparticles on the Au(111) surface., *J. Chem. Phys.* 123 (2005) 094705.

Chapter 4 – Supporting information

The growth and stability of Au surface oxides on $\text{WO}_3/\text{Au}(111)$ and $\text{ReO}_3/\text{Au}(111)$ inverse model catalysts

4.5 Reduction and surface alloying of WO_3 at elevated temperature

To study the stability of WO_3 on the Au(111) surface, we conducted a series of experiments at elevated temperatures. Figure 4.7a and b show 0.03 ML $\text{WO}_3/\text{Au}(111)$ before and after annealing to 567 K in vacuum. Before annealing, we associate the bright features with WO_3 and the dark lines with the needle type Au surface oxide, similar to Figure 4.4 in the main text. After annealing, only 0.008 ML WO_x is visible in

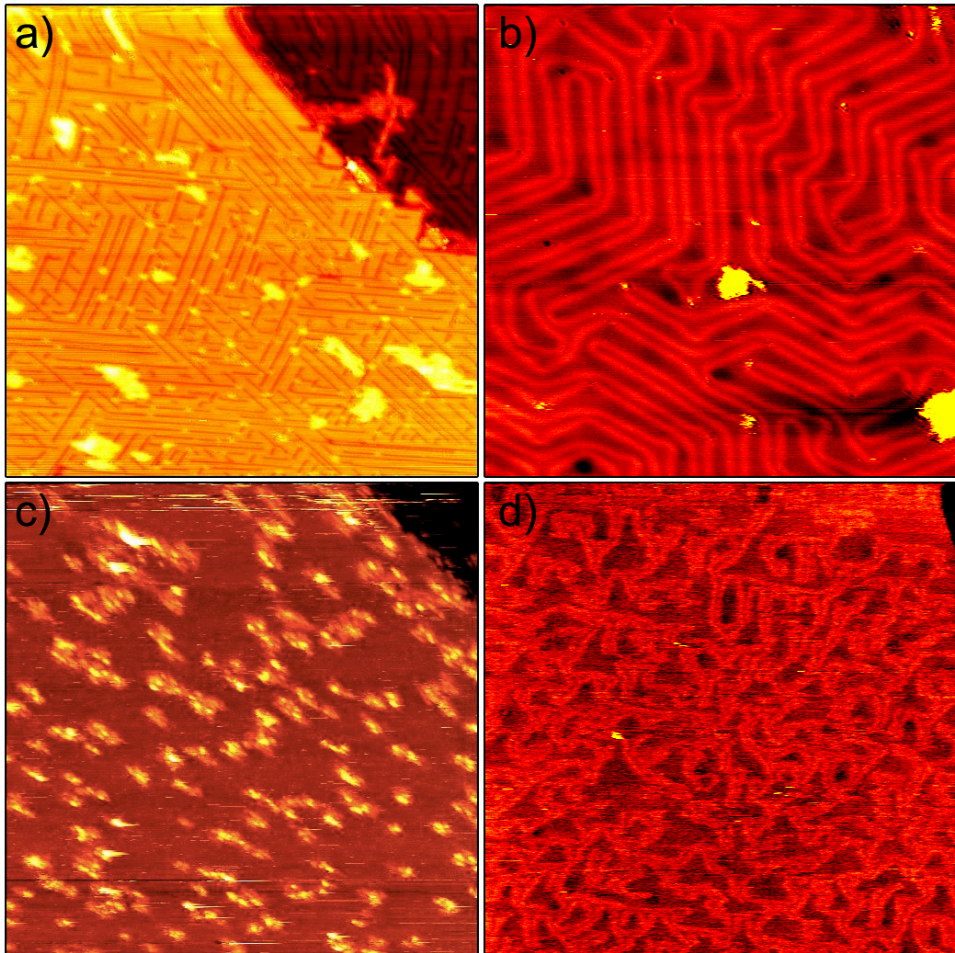


Figure 4.7: Surface alloying of $\text{WO}_3/\text{Au}(111)$ at elevated temperature. a) 0.03 ML $\text{WO}_3/\text{Au}(111)$ prepared by WO_3 deposition at 567 K in 1×10^{-5} mbar O_2 and cooling to 400 K in O_2 , 80 nm x 80 nm, $U_s = 2$ V, $I_t = -135$ pA. b) Sample in a) after annealing at 567 K in vacuum, 80 nm x 80 nm, $U_s = 2$ V, $I_t = -110$ pA. c) 0.2 ML $\text{WO}_3/\text{Au}(111)$ prepared by W deposition at room temperature, followed by annealing in 1 bar O_2 for 1 hour, 80 nm x 80 nm, $U_s = 2$ V, $I_t = -90$ pA. d) same as c), after annealing at 653 K in 5×10^{-6} mbar O_2 , 160 nm x 160 nm, $U_s = -1$ V, $I_t = 30$ pA

the STM images (see Figure 4.7 b), even though sublimation is not expected at the mild annealing temperature employed here. Alternatively, surface alloying of W with the gold may have occurred. The dark stains in the fcc areas of the herringbone reconstruction in Figure 4.7b suggest that a W-Au alloy is indeed formed. The surface alloying process is even more pronounced in experiments with a higher WO_3 coverage, as shown in Figures 4.7c and d. The sample for this experiment was prepared via the deposition of approximately 0.2 ML W metal and subsequent oxidation in 1 bar O_2 at 523 K for 1 hour. This results in the structure shown in Figure 4.7c. After annealing to 653 K in 5×10^{-6} mbar O_2 , no particles are visible on the surface and the herringbone reconstruction is strongly modified (see Figure 4.71d). Again, this points at the formation of a surface alloy. The larger amount of tungsten present on the surface allows for a stronger modification of the herringbone reconstruction. The observation that the surface alloying even occurs in the presence of oxygen shows that the tungsten oxide is not only kinetically instable at high temperature in vacuum, but also thermodynamically unstable at modest oxygen chemical potential ($\mu_{\text{O}} = -2.46$ eV under the applied conditions).

4.6 X-ray beam induced desorption of surface oxides

Damage to adsorption structures due to (photo)electrons is a well-known phenomenon in surface science. However, due to its comparatively low electron flux, lab source X-ray photoelectron spectroscopy (XPS) is usually less prone to beam damage effects. In our case, the X-ray beam spot on the sample had a diameter of approximately 4 mm, inducing a sample current of 1.1 nA. Thus, in the 2.5 hours of X-ray exposure that we needed for the experiment, only 0.35 photoelectron per Au surface atom left the surface.

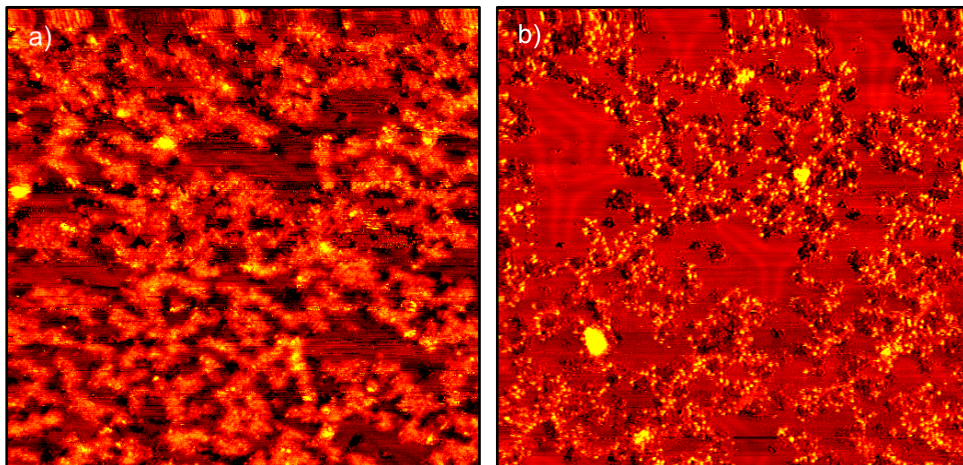


Figure 4.8: 0.012 ML $\text{ReO}_3/\text{Au}(111)$ before (a) and after (b) XPS measurements. a) 80 nm x 80 nm, $U_s = -1\text{V}$, $I_t = 50$ pA. b) 80 nm x 80 nm, $U_s = -1$ V, $I_t = 50$ pA

Figure 4.8 shows that even under this very mild radiation load, substantial beam-induced oxygen desorption occurs. This indicates that synchrotron measurements, which employ a beam flux that is several orders of magnitude larger, need to be performed with the greatest of care. In our case, the O 1s spectrum was recorded within the first 45 minutes of the measurement. Nonetheless, one may expect that the measured signal intensity was affected by the beam-induced desorption.

4.7 Evolution of $\text{WO}_3/\text{Au}(111)$ during pressure ramp to 500 mbar O_2

The starting structure for the high-pressure experiment shown in this section was formed by exposure of a $\text{WO}_3/\text{Au}(111)$ sample to 1×10^{-5} mbar O_2/O at room temperature, followed by annealing at 500 K to partially smoothen the surface. The oxygen atmosphere was maintained until the sample temperature was back below 423K. The resulting surface structure contains modest amounts of AuO_x , which we associate with the bright features in Figure 4.9a. Furthermore, vacancy islands are apparent.

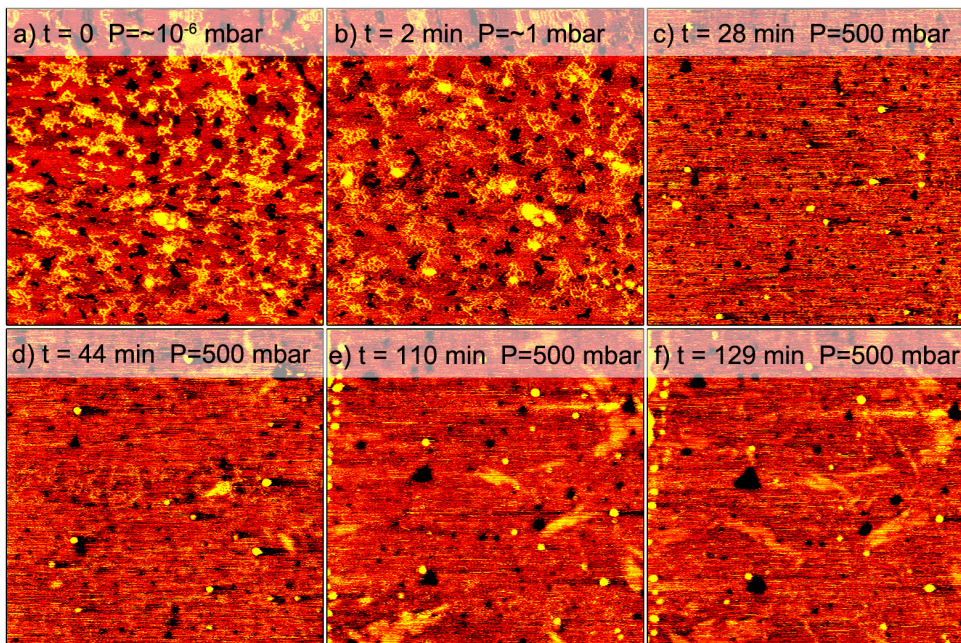


Figure 4.9: Structural evolution of $\text{WO}_3/\text{Au}(111)$ during high-pressure oxygen exposure at room temperature. Panels a) and b): 80 nm x 80 nm, other panels: 160 nm x 160 nm. All frames are recorded at $U_s = 2$ V and $I_t = -170$ pA. All indicated pressures refer to oxygen.

Following the preparation, the surface was imaged at room temperature while the O_2 pressure was increased from 10^{-6} mbar to 500 mbar. The lower bound, 10^{-6} mbar, is an estimate that corresponds to the situation where the reactor is only connected to the UHV chamber via thin gas lines. Under these conditions, there is a poorly defined vacuum inside the reactor. When the gas lines are switched from the mode in which they connect to the UHV system to the mode in which they connect to the high-pressure gas supply, the pressure jumps to approximately 1 mbar. Figure 4.9b shows that the bright species from Figure 4.9a become less apparent after this pressure increase. The surface morphology is maintained. While we further increased the pressure, the images became streaky (see Figure 4.9c), indicating that there are dynamic species present on the surface. The bright species disappear nearly completely, which we interpret as their dissolution in the dynamic phase on the terraces. Subsequently, islands with highly anisotropic shapes emerge, which we associate with AuO_x . The nucleation of these islands seems to occur at random locations on the surface, without preference for steps or vacancy islands. Note that the number of islands formed and the rate of their formation may have been affected by the STM tip. The row of particles on the left-hand side in Figures 4.9e and 4.9f indicate that atoms have been moved to the side of the imaging area. In other high-pressure experiments, we noted that instabilities in the tunneling caused the formation of vacancy islands. This again signifies the dynamic nature of the Au surface when adsorbed oxygen is present. Images recorded immediately after moving to previously unimaged areas ensured that the formation of the surface oxide islands occurs everywhere on the surface. The images obtained in UHV after the high-pressure exposure, described in the main text, corroborate this.

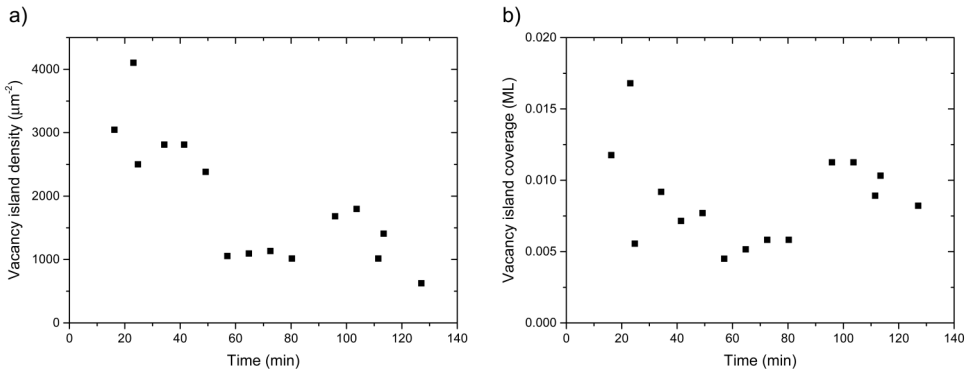


Figure 4.10: Evolution of vacancy islands during the high-pressure experiment shown in Figure 4.9.

During the high-pressure experiment, it is clear that some vacancy islands grow in size. Meanwhile, the number of vacancy islands clearly decreases, as shown in Figure 4.10a. Since the “center of mass” of the vacancy islands remains constant, we conclude that Ostwald ripening occurs. In vacuum, the vacancy islands were stable. Hence, the adsorbed oxygen at high-pressures must induce an increased mobility of vacancies

over the terraces. Figure 4.10b shows that the total vacancy island area remains constant during the experiment, although the measured values scatter around the average with a standard deviation of 37%. This large scatter results from the streakiness of the images, which hampers proper quantification. As noted in the main text, a constant vacancy island density implies that gold adatoms are not part of the dynamic phase on the terraces, because these would have filled the vacancies. In the experiment shown in Figure 4.9, we did not observe the formation of new vacancy islands, which indicates that no Au adatoms are required for the formation of the AuO_x islands.

4.8 Influence of the preparation conditions on the structure and coverage of the needle phase Au oxide

The needle type oxide was generated via two methods. In the first, WO_3 or ReO_3 was deposited at 567 K in 1×10^{-5} mbar O_2 , after which the sample was allowed to cool down over the course of several minutes to 423 K in 1×10^{-5} mbar O_2/O . Figure 4.4 in the main text shows the result of this procedure. We note however that the coverage obtained is sensitive to the exact preparation conditions, as is evidenced by Figure 4.11a. The surface was prepared using the same procedure as in Figure 4.4 in the main text, yet the observed Au oxide needle coverage is clearly lower. One may wonder therefore whether the surface truly equilibrates during the cooling down to 400 K. To resolve this, we prepared the needle phase via a second procedure. WO_3 was

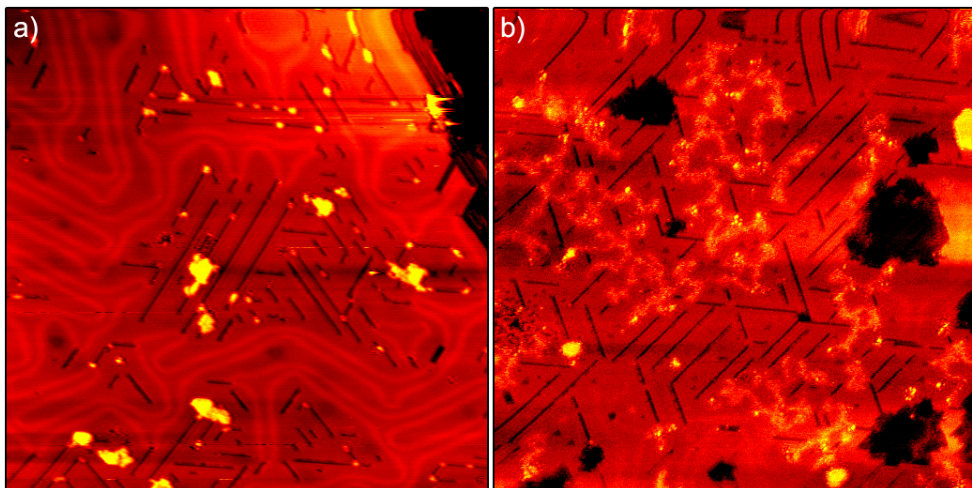


Figure 4.11: Influence of the preparation conditions on the Au needle oxide coverage. a) $\text{WO}_3/\text{Au}(111)$ prepared through WO_3 deposition at 567 K, followed by cooling to 423 K in 1×10^{-5} mbar O_2/O . 80 nm x 80 nm, $U_s = 2$ V, $I_t = -95$ pA. b) $\text{WO}_3/\text{Au}(111)$ prepared through WO_3 deposition at room temperature, followed by 15 minutes 1×10^{-5} mbar O_2/O exposure, 15 minutes annealing to 423 K in vacuum, and 15 minutes 1×10^{-5} mbar O_2/O exposure at 423 K. 80 nm x 80 nm, $U_s = 1.5$ V, $I_t = -160$ pA.

deposited at room temperature in 1×10^{-5} mbar O_2 , followed by 15 minutes of 1×10^{-5} mbar O_2/O exposure. After this, the surface was annealed at 423 K in vacuum for 15 minutes to smoothen the surface, followed by 15 minutes of 1×10^{-5} mbar O_2/O exposure at 423 K to generate an equilibrium coverage of Au oxide needles. As can be seen in Figure 4.11b, this results in an oxide needle coverage similar to that in Figure 4.4. Thus, we conclude that the surface in Figure 4.4 was equilibrated with the conditions at 423 K. A possible explanation why we do not always reach equilibrium, such as in Figure 4.11a, could be a variation in the distance between the filament and the sample. The flux of atomic oxygen to the surface depends quadratically on the filament-sample distance. Hence, variations in this distance may generate strong variations in the amount of AuO_x nuclei that are generated. As a result, the time required to reach equilibrium will fluctuate. Another source of variation is the cooling rate, which was not actively controlled in the experiments.

Chapter 5

Simultaneous scanning tunneling microscopy and synchrotron X-ray measurements in a gas environment

A combined X-ray and scanning tunneling microscopy (STM) instrument is presented that enables the local detection of X-ray absorption on surfaces in a gas environment. To suppress the collection of ion currents generated in the gas phase, coaxially shielded STM tips were used. The conductive outer shield of the coaxial tips can be biased to deflect ions away from the tip core. In tunneling contact, the X-ray-induced current is separated from the regular topographic tunneling current using a novel high-speed separation scheme. We demonstrate the capabilities of the instrument by measuring the local X-ray-induced current on Au(111) in 800 mbar Ar.

5.1 Introduction

The synchrotron-based techniques developed over the last decades provide a powerful toolbox for the study of interface phenomena. The weak interaction of X-rays with matter makes these methods particularly suitable for *operando* studies, which are indispensable in research areas such as catalysis [1], environmental science [2], and film growth [3]. However, most X-ray techniques make use of a large beam spot compared to the features studied, thereby averaging out possibly important structural and chemical variations. For techniques that use a highly focused beam on the other hand, finding the feature of interest can be a tedious process as searching based on reciprocal-space images or absorption features is non-trivial.

Scanning probe microscopy can supplement X-ray measurements by providing local structural information in real space. Inspired by this potential, several atomic force microscopes (AFM) [4–9] and scanning tunneling microscopes (STM) [10–14] have been installed on beamline end stations. In the AFM studies, it was shown that the AFM tip can be used to align the X-ray beam with features of interest [6]. Once aligned, the tip can be used for nano-manipulation or the application of local stress [15,16].

Using the combination of STM and X-rays, it was shown that the current collected by the STM tip can be used to measure local X-ray absorption, with a spatial resolution as small as 2 nm [11,17–19]. Thus, local chemical information can be obtained and coupled to the local structure. This combination is highly desirable for the understanding and design of materials and chemical processes.

So far, all synchrotron X-ray assisted STM (SXSTM) studies have been performed in vacuum. Under these conditions, the signal collected by the tip consists of three principal components: the photo-electron current, the regular topographic tunneling current, and an X-ray-induced increase of the tunneling current. While both the photo-electron current and the X-ray-induced increase of the tunneling current are related to X-ray absorption, only the latter provides local information [11,17–19]. To improve the ratio between this local signal and the photo-electron current, most SXSTM experiments employ insulator-coated STM tips, leaving only the tip apex uncoated [17,20–23]. This effectively reduces the number of photo-electrons that the tip collects. Besides this background reduction, the X-ray-induced part of the tunneling current needs to be separated from the regular tunneling current. Several experimental schemes employing a beam chopper and lock-in amplification have been developed for this purpose [11,24].

To use SXSTM in *operando* studies at elevated pressures, two challenges need to be addressed: i) Inhibitively large ion currents are generated in the gas phase. We show that insulator-coated tips are inadequate to suppress these. ii) Most interesting systems for *operando* studies require elevated temperatures and have some degree of roughness in their morphology. To cope with thermal drift and to follow the surface morphology accurately, fast response in the height feedback is necessary. However,

the current separation schemes for the regular and the X-ray-induced tunneling current limit the height feedback in the STM to response frequencies below roughly 1 kHz.

Here, we describe an instrument that can perform SXSTM measurements in a gas environment using hard X-rays, overcoming the barriers for performing *operando* studies. Our methodology provides several novelties: i) A quick method for aligning tip and beam with micrometer precision. ii) An electronics scheme to separate X-ray-induced current and regular tunneling current that enables fast height feedback at frequencies up to the chopper frequency. iii) A coaxially shielded STM tip and mounting configuration that effectively suppresses the ion current background. As a proof of concept, we have collected the local, X-ray-induced tunneling current on a Au(111) sample at a gas pressure of 800 mbar.

5.2 Instrument design

5.2.1 High-pressure cell

The starting point for our experiments was the high-pressure scanning probe and surface X-ray scattering instrument developed earlier in collaboration between our group and the ID03 beamline staff at the ESRF [14], which we modified for the SXSTM measurements. In short, this system consists of an ultrahigh vacuum (UHV) chamber with a high-pressure cell on top (see Figure 5.1) [25]. The UHV chamber allows for surface preparation by ion bombardment, annealing, controlled gas exposure, and metal evaporation onto the sample. The high-pressure cell can be operated as a flow reactor, providing a controlled gas atmosphere at pressures up to 1.1 bar. The cell is exchangeable, allowing for a versatile combination of experiments.

In our recent work, we fitted a high-pressure scanning probe module on the system [14,26]. Similar to the design of the ReactorSTM and ReactorAFM [27,28], it uses a single piezo tube both for the coarse approach of the tip to the sample and for generating the scanning motion. The coarse approach is achieved by a stick-slip motion of the tip holder (slider) on two tracks. The piezo tube is separated from the gas environment by a polyimide cap and a viton seal, as depicted in Figure 5.1b. In our previous design, the reactor wall was a dome-shaped aluminum piece of 1 mm thickness, providing homogeneous and satisfactory X-ray transmission over a large range of angles at photon energies above 18 keV. While this made the system excellent for surface X-ray diffraction measurements, the X-ray transmission was insufficient in the lower energy range relevant to X-ray absorption spectroscopy.

To allow for measurements at energies down to 8 keV, we designed a new cell that uses four thin, exchangeable windows (see Figure 5.1) sealed on both sides by viton O-rings. In our first test measurements, we used a stack of three 75 μm thick Kapton sheets for each window. In the energy range from 10 keV to 12 keV, the Kapton stack provides an excellent X-ray transparency of 91% to 95% [29]. However, the

permeability of Kapton towards gases [30] limits the base pressure of the UHV chamber to the 10^{-6} mbar range. Aluminum foil windows provide a lower transmission (59% for 100 μm thick foil at 11 keV [29]), yet do not suffer from any gas permeability. Beryllium windows were not preferred here for safety reasons, as the reactor needs to be handled frequently for tip exchanges.

The reactor walls and the part of the microscope head that are exposed to gases are gold coated. This prevents undesirable side reactions from occurring on these surfaces. Furthermore, charge collected on the walls from photo-electrons and ions is immediately neutralized. Charging of the native oxide of materials such as aluminum and stainless steel may cause memory effects in the background signal of the SXSTM measurements. This could adversely affect the reproducibility of the data.

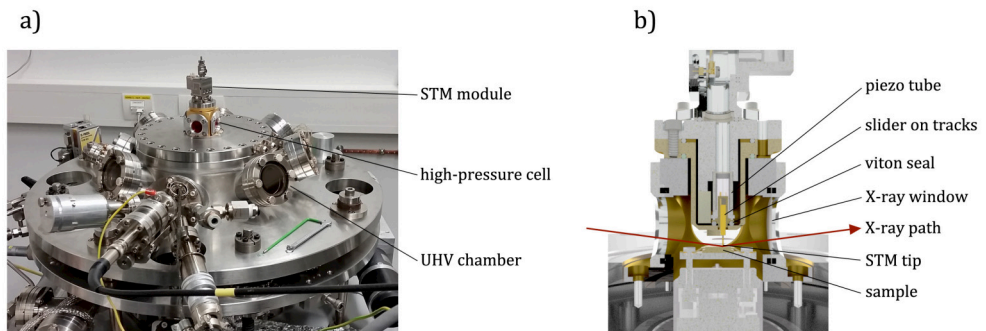


Figure 5.1: Overview of the set-up. a) Assembly of ID03's ReactorSXR chamber [25], our new high-pressure cell and the recently developed STM module [14]. b) Cross-section of the STM module and high-pressure cell.

5.2.2 Coaxial tips and mounting scheme

In a gas environment, the X-ray-induced current collected by the STM tip behaves differently as compared to the vacuum situation. Photo-electrons emerging from the sample cause a cascade of ionization processes in the gas. This effect is particularly pronounced for the high-energy Auger electrons produced during hard X-ray absorption [31,32]. Furthermore, the plasma created in the gas environment helps the charge transport to and from insulating surfaces [33–35]. Hence, when a beam chopper is employed, this may generate oscillating electric fields that can couple into the tunneling current. These effects cause a complex behavior of the background signal in SXSTM measurements, making reproducibility of experiments difficult. It is therefore essential to minimize the background current.

To achieve this reduction in background, we fabricated both insulator-coated and coaxially shielded STM tips. The latter consist of a conductive core, an insulating layer, and a conductive outer layer (shield), as shown in Figure 5.2. While the core is

used for measuring the tunneling current, the shield layer neutralizes ions. Tips are mounted such that the shield potential can be controlled independently with respect to the tip core and the sample, thus creating an electric field that deflects ions away from the tip core.

The insulator-coated tips were fabricated by a combination of SiO_2 sputter deposition and focused ion beam milling similar to that reported in literature [20,22,23]. The fabrication of coaxially shielded tips is less well established [17], hence we explored several preparation methods. As core material, we have used an electrochemically etched $\text{Pt}_{0.8}\text{Ir}_{0.2}$ wire (\varnothing 0.25mm, Goodfellow). Three different types of insulation layer were tested: i) 100 nm SiO_2 prepared by atomic layer deposition (ALD) through 1100 cycles of bis(diethylamido)silane (Sigma-Aldrich SIBDEA) exposure and an O_2 plasma as co-reactant at 200 °C. ii) 1000 nm SiO_2 prepared by plasma-enhanced chemical vapor deposition (PE-CVD) using a plasma of silane and O_2 at 300 °C. iii) Polymer coating prepared by pushing the tip through a droplet of polyethylene-vinylacetate-based glue gun wax at 80 °C, a method commonly used for electrochemical STM [36].

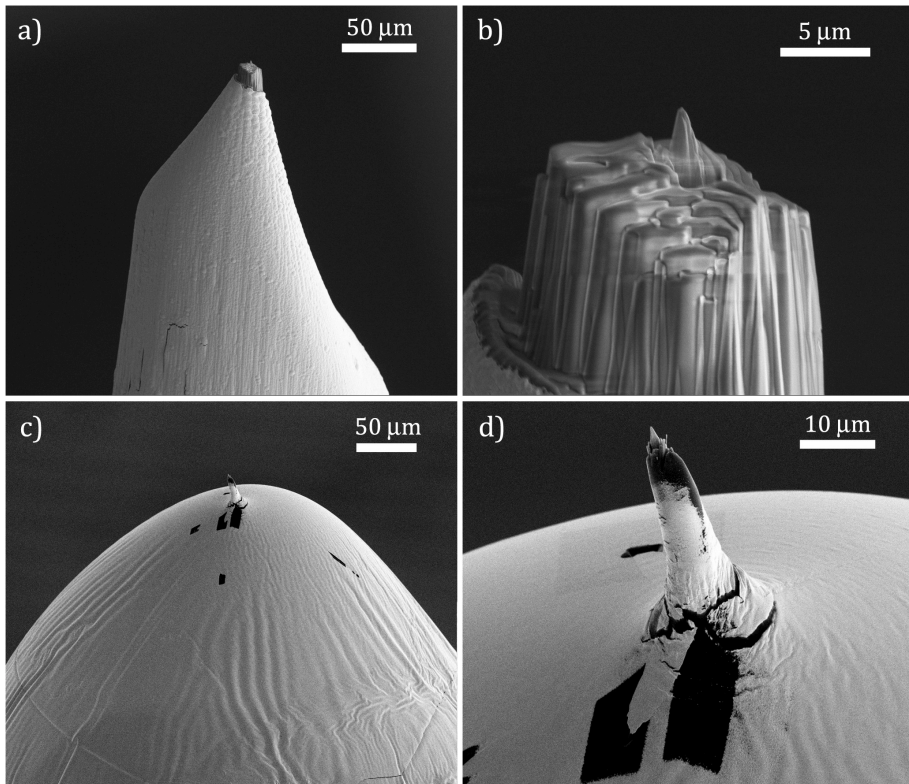


Figure 5.2: Scanning electron microscopy (SEM) images of coaxially shielded STM tips. a,b) $\text{Pt}_{0.8}\text{Ir}_{0.2}$ with SiO_2/Au coating. c,d) $\text{Pt}_{0.8}\text{Ir}_{0.2}$ with polymer/ Au coating.

In all three cases, $>2\text{ M}\Omega$ core-shield insulation was accomplished with a success rate of over 50%. For the ALD tips, the coating was very homogeneous but too fragile to survive further assembly. For the PE-CVD tips, the insulation thickness was not uniform over the tip due to inhomogeneities in the plasma that are common around conducting three-dimensional objects inserted into the plasma. As a result, the coating at the apex was $7.5\text{ }\mu\text{m}$ thick while the average was only $1\text{ }\mu\text{m}$. For the polymer-coated tips, the coating thickness decreased from $1\text{ }\mu\text{m}$ halfway the tip to a few hundred nanometer at the apex (see Figure 5.2).

The shield coating was applied by radiofrequency sputter deposition of a Ti seed layer followed by 500 nm Au for the ALD and PE-CVD tips and 100 nm Au for the polymer tips. Subsequently, the apex was shaped using focused ion beam milling. In this process, the original tip apex was first cut off, followed by a donut-shaped ion milling pattern around the new tip apex to remove the last $\sim 1\text{ }\mu\text{m}$ of the isolation and shield layers, so that the core protrudes (see Figure 5.2). Using a finer donut shape, the apex was sharpened.

The mounting configuration of the coaxial tips is depicted in Figure 5.3. Essential in the design is that the core and shield of the tip have separate electrical connections. Furthermore, the pick up of ion current by the tip holder needs to be minimized. To achieve this, a gold-coated Kapton foil was attached to the tip using non-conductive glue. Subsequently, the Au coating of the Kapton foil was connected to the shield of the coaxial tip using Agar silver paint. Similarly, a thin Au-coated tungsten wire was contacted to the Au coating of the Kapton through a puncture in the foil. This wire and the tip core were mounted on the tip holder (slider), which consists of two electrically isolated pieces of Au-coated machine steel. Each piece makes contact to one of the tracks on the piezo motor. Shielded wires provide connections from to the two tracks to outside of the reactor.

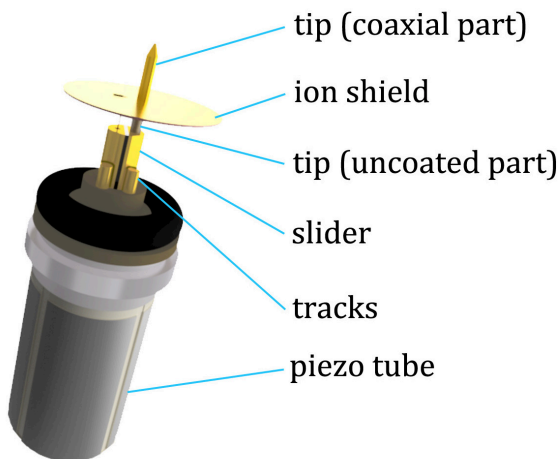


Figure 5.3: Mounting configuration of the coaxial tip.

After tip fabrication and mounting, a typical resistance of $2\text{ G}\Omega$ between tip core and shield could be achieved, allowing for a shield bias of several volt with respect to the core. Thus a strong electrical field between the tip shield and the sample can be applied, deflecting both positive and negative charges before they can reach the tip core.

5.2.3 Tip-beam alignment

All experiments were conducted at the ID03 beam line at the European Synchrotron Radiation Facility (ESRF). The beam was focused to $25\text{ }\mu\text{m} \times 25\text{ }\mu\text{m}$ using a toroidal mirror. In the energy window employed, 10 keV to 13 keV, a flux of 10^{13} photons/s was delivered to the sample in the reactor cell with Kapton windows. For the Al dome reactor developed in our previous work [14], the flux on the sample was around 10^{11} photons/s.

In order to align the STM tip with the X-ray beam, the chamber was placed on a hexapod, which in turn stands on a six-circle diffractometer. This allows translation in x (horizontal, perpendicular to the beam), y (parallel to the beam), and z (vertical), as well as tilting and rotation. We used the shadow of the STM tip on the Maxipix X-ray detector [37] as a probe for the alignment. First, the tip was brought to within a few micrometer from the sample surface. With the beam parallel to the sample surface, the chamber height (z) was set such that half of the beam was blocked by the sample. When the chamber is then translated in x , it passes through the configuration in which the beam hits the tip, casting a shadow on the detector. Figure 5.4a depicts the intensity of the beam spot on the detector recorded during such a chamber translation scan. The minimum of this curve is located at the position where the tip maximally blocks the beam, as is also evidenced by the tip shadow that can be seen in the X-ray detector images (see Figure 5.4c) and the reflections from the sides of the tip. In order to align in both lateral directions, the chamber was rotated by 90° and the same scan was performed.

To confirm the accuracy of this method, a similar scan was performed with the X-rays incident on the sample at 0.5° . In this case, the beam reflected from the sample is recorded, which can also be blocked by the tip. Simultaneously, the photo-electron current on the tip core was measured. As shown in Figure 5.4b, the mismatch between the current maximum and the maximal beam blocking by the tip is only a few micrometer. The origin of this slight mismatch is likely the asymmetry of the tip on the scale of the beam spot, which is also apparent in Figure 5.4c.

5.2.4 Electronics scheme for separating the regular from the X-ray induced tunneling current

To obtain the local X-ray absorption signal, the X-ray beam is chopped [11,24]. Without adjustments to the height-feedback mechanism, which uses the tip current as an input, this would result in an oscillation of the tip height. In principle, the height

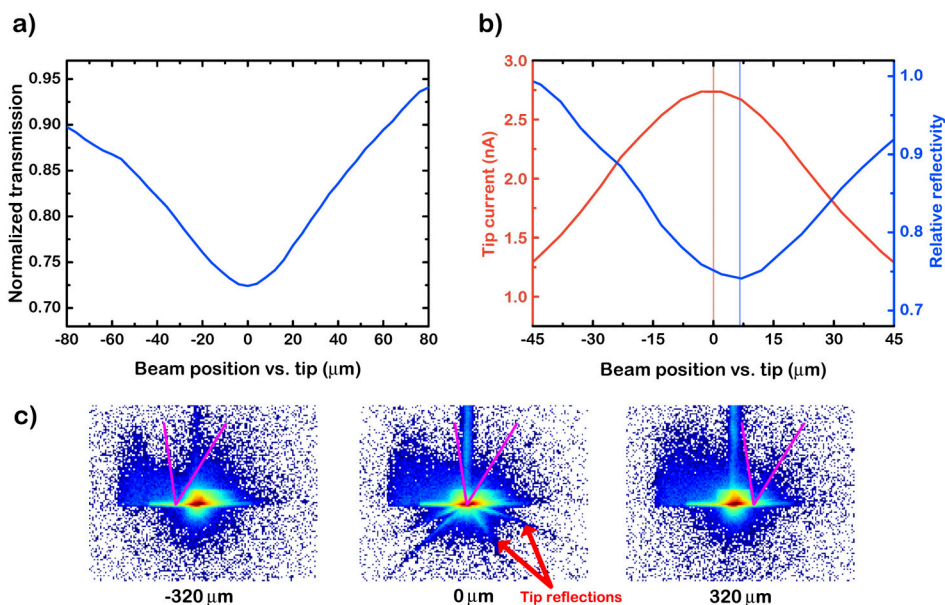


Figure 5.4: Alignment of STM tip and X-ray beam (tip-sample distance: $\sim 3 \mu\text{m}$). a) Transmission when moving the beam across the tip apex (beam parallel to sample). b) Tip current and X-ray reflection intensity when moving the beam across the sample underneath the tip (0.5° incidence). c) Beam spot on the detector when moving the beam across the tip. The purple lines indicate an estimate of the tip apex profile.

signal can be lock-in amplified to find the local X-ray absorption signal. However, the height signal has a logarithmic dependence on the tip current, making it relatively insensitive to the X-ray induced signal.

An alternative was proposed by Wang *et al.* [24], who performed height feedback on the tip current only after applying a low-pass filter. In this case the photo-induced signal is obtained from the tip current before the low-pass filter using lock-in amplification. In order to completely remove photo-induced effects from the height feedback, the photo-current signal from the lock-in amplifier is scaled and subtracted from the low-pass-filtered tunneling current. While this scheme allows for stable tunneling, the height feedback is limited to frequencies of maximally $0.1 \times$ chopper frequency. The bandwidth of the high-gain preamplifiers used in STM restrict the chopper frequency to roughly 10 kHz, leading to a maximal feedback frequency of 1 kHz. This is adequate for flat surfaces and slow data acquisition in environments with low vibrational noise levels. However, more flexibility is desired for the nanoparticle systems typically used in catalysis. Furthermore, the challenging boundary conditions resulting from the integration of an STM in a reactor end-station impose limitations to the vibrational noise reduction that can be achieved [14].

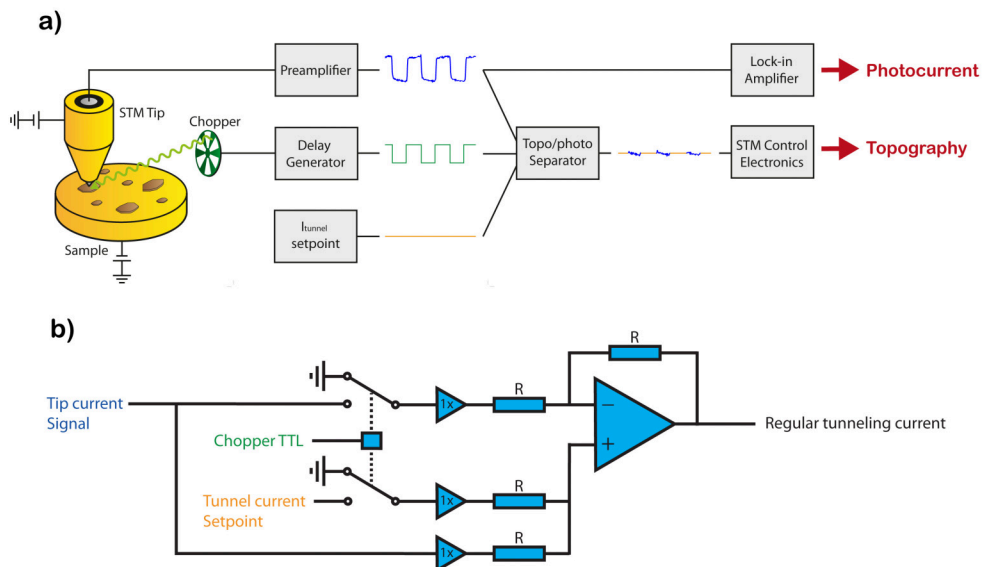


Figure 5.5: a) High-speed separation scheme for the regular tunneling current and the X-ray-induced current. b) Electronic circuit for the topo/photo separator, generating the input for the STM control system without X-ray-induced contributions.

In order to perform faster height feedback, we have developed a new scheme to separate the X-ray-induced current from the regular tunneling current. In essence, our circuit switches the height feedback off during the “beam on” phase of the X-ray chopper. This is accomplished by replacing the measured signal by the tunneling current setpoint during this phase. To do this, the transistor-transistor logic (TTL) signal from the beam chopper is fed into a delay generator, with which the phase and the duty cycle of the TTL signal can be adjusted independent of the phase and duty cycle of the chopper. Thus, the TTL phase can be matched to that observed in the tip signal. Adjusting the TTL duty cycle to prolong the “feedback off” period can be useful if the tip signal is not a perfect square wave, as is the case for our measurements in a gas environment.

The modified TTL signal is used in a purpose-built circuit (Figure 5.5b), which performs the following operation:

$$\text{Output} = \text{Tip current} + \text{TTL} \times (\text{Tunneling current setpoint} - \text{Tip current})$$

The output signal can be used for height feedback at frequencies up to the chopper frequency. In principle, the X-ray-induced signal could be obtained in a similar fashion. However, lock-in amplification of the tip signal provides a better signal-to-noise ratio.

We have first tested the acquisition scheme described above using the X-ray-induced current measured with the tip out of tunneling contact. From the data in 5. 6, it is clear that the X-ray-induced current is effectively removed from the regular signal. At high chopper frequencies, the signal deviates from the ideal square wave. Nevertheless, Figure 5.6b shows that the X-ray induced current can still be completely removed by changing the duty cycle of the TTL signal, thus evidencing the robustness of our scheme.

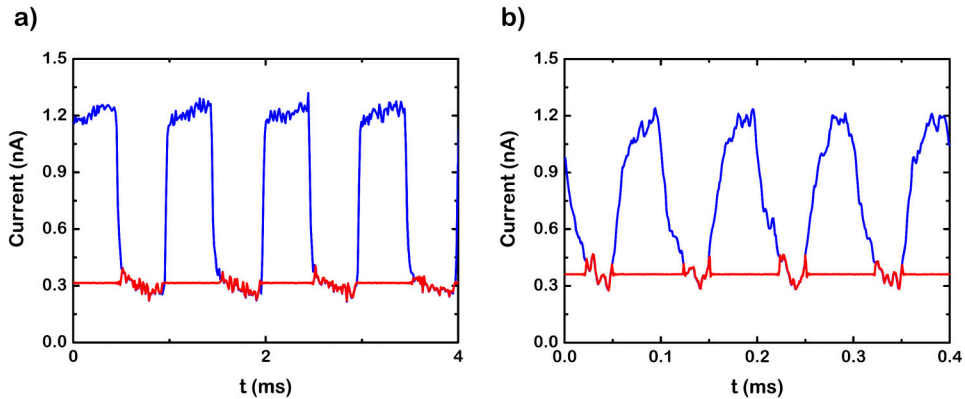


Figure 5.6: Test of the topo/photo current splitter using the X-ray-induced current with the tip out of tunneling contact in 1 bar O_2 . The blue and the red curves show the signal before and after the separation circuit, respectively. a) Chopper at 1kHz b) Chopper at 10 kHz.

5.3 Performance

5.3.1 Current contributions from the gas environment

We have studied the SXSTM background currents generated by photo-electrons and ions by comparing the currents measured with a coaxial tip out of tunneling contact above a Au(111) surface in Ar, O_2 and in a modest vacuum of approximately 1 mbar. Although it is clear that many ionization events occur in the gas phase [31,32], it is not evident how these translate into the detection of a net current. We observed that the background current exhibits complex behavior, which is strongly dependent on many parameters. For instance, the current measured on the tip core at large tip-sample distances was clearly much higher in Ar than in O_2 (see Figure 5.7a). In contrast, at a tip-sample distance of only a few micrometers, the current was slightly higher in O_2 . In general, the tip current was higher in a gas environment than in vacuum.

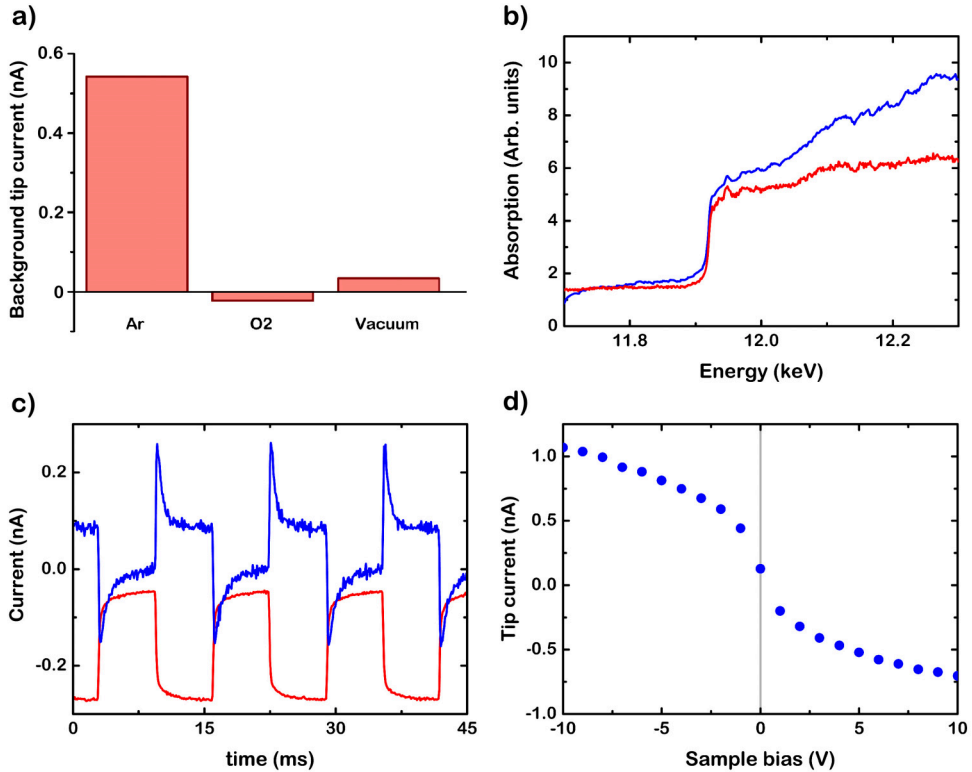


Figure 5.7: Characteristics of the SXSTM background currents in a gas environment, recorded with the tip out of tunneling contact. a) Background current on the tip in various environments at a photon energy of 12.3 keV for a tip-sample distance of 0.8 mm and a sample bias of -1 V. The Ar or O₂ pressure was 800 mbar, while ‘vacuum’ corresponds to a residual pressure of approximately 1 mbar. b) Au L3 edge absorption spectra from the fluorescence signal on the X-ray detector (red) and the tip current (blue), recorded in 800 mbar Ar. c) Sample current (red) and tip current (blue) in 500 mbar O₂ with the beam chopped at 80 Hz in an uncoated reactor, recorded with a SiO₂/Mo tip without Au shield. d) Dependence of the background signal on the sample bias, recorded in 800 mbar Ar.

From the Au L3 edge absorption spectrum in Figure 5.7b, it is clear that the tip current follows the absorption coefficient, apart from a difference in background slope. This is expected, as ion current collection is commonly used in conversion electron yield X-ray absorption spectroscopy [32]. Similarly, when changing the beam intensity (data not shown) the current-intensity relation only slightly deviates from linearity. In contrast, severe signal distortions can be observed in time-dependent measurements, when the beam is chopped. Figure 5.7c shows an example where the distortions occur both in the sample current and in the tip current. The origin of these distortions is likely related to charging and discharging of insulating surfaces in the reactor, which is accelerated in the presence of a gas environment [33–35]. For the measurement in Figure 5.7c, the Al dome reactor (with an insulating native oxide) was used, together

with a SiO₂-coated Mo tip without a conductive shield. Hence, charging/discharging may also occur on the insulating coating of the tip, strongly coupling into the tunneling current signal. This explains why the distortions are much more pronounced for the tip than for the sample. X-ray absorption by the gas was not a major contributor to the background currents, as was shown by measurements with the beam passing through the reactor without hitting the sample.

Figure 5.7d shows that the background current of the tip depends on the applied sample bias. For non-zero bias, the positively and negatively charged species generated by ionization events in the gas phase are separated by the electric fields between the sample, the tip and the reactor walls. The lack of precise symmetry in the tip current may be related to the fact that a net positive current is injected into the gas phase from the sample. As Figure 5.7a shows however, the current sign may also be inverted for different gases, again underlining the complexity of the charge dynamics in the background currents.

5.3.2 Background reduction using coaxial tips

To test the effectiveness of the coaxial STM tips described in Section 5.2.2, which consist of a conductive core and shield separated by an insulation layer, we simultaneously measured the current on the tip shield and on the core. As can be seen in Figure 5.8a, the maximum shield current is two orders of magnitude higher than that of the core. When the beam is placed more than 150 μm away from the tip, the core is completely insensitive towards the X-rays. In this situation, the electric field between tip shield and sample is sufficient to deflect all ions and electrons so that they cannot reach the tip core.

In many SXSTM studies, the STM tips were coated with an insulation layer only, not with a conductive outer shield [20–23]. While this can be adequate in UHV, Figure 5.7c shows that charging/discharging effects can cause signal distortions in a gas environment. The details of the shape of the distortions depend strongly on the precise beam-tip alignment and the gas environment, which makes it difficult to reproduce results. Hence, it is essential to use STM tips with a conductive outer shield for performing SXSTM measurements in a gas environment.

From Figure 5.6 it is clear that the coaxial tips provide the required improvement, since the square wave signal is only mildly distorted. It should be noted, however, that the magnitude of the background signal is still in the nA range and varies strongly from tip to tip. The type of insulation layer is not the most important factor, as the polymer-coated tips produced both the best and the worst background. Most likely, the geometrical variation at the tip apex is a major contributor to the observed differences between tips.

In addition to the fast signal distortions of the square wave, some Au/polymer-coated tips showed a slowly increasing offset current, which builds up during several minutes

after switching on the beam and can reach values of several hundred pA. The origin of this offset current must be a slow charging effect, which we have not been able to identify further. However, once the offset current has stabilized, it does not interfere with the SXSTM measurements.

To further reduce the background current, we applied a bias voltage to the shield. Figure 5.8b shows the effect of the bias on the X-ray-induced current received by the tip core. The current was corrected for the leakage current baseline in the absence of X-rays ($2\text{ G}\Omega$ shield-core resistance). Clearly, a small positive bias of $\sim 0.5\text{ V}$ on the shield strongly reduces the background current. Surprisingly, at negative or larger positive shield bias, the background is not effectively reduced or even amplified. This could be due to surface conduction induced by ions landing on the exposed part of the tip insulation layer, as this would increase the leakage current between shield and core.

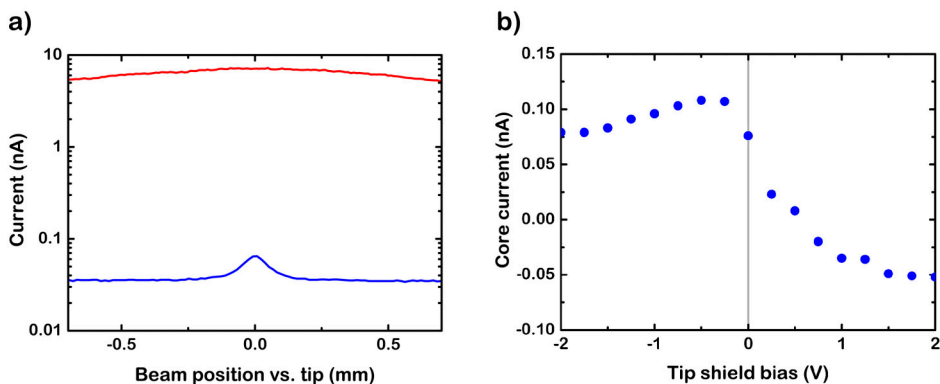


Figure 5.8: Effectiveness of the background reduction. a) Tip core (blue) and shield current (red) when scanning the beam across the tip in 1 bar O_2 at a tip-sample distance of $10\ \mu\text{m}$. Sample bias: -1 V , tip shield bias: 0 V b) Tip core current versus tip shield bias in 800 mbar Ar.

5.3.3 Imaging

A requirement in SXSTM measurements is that the tip is sufficiently sharp to properly image the surface: the height resolution should suffice to see atomic height steps and the lateral resolution should be better than 2 nm in order to identify nanoparticles. Figure 5.9 shows that atomic step resolution on Au(111) was indeed obtained with a Au/polymer coaxial tip in a beam chopped at 10 kHz . Line scans at higher magnification show that the Au(111) steps are imaged with a width of roughly 1 nm . Hence, the tip is sufficiently sharp to meet the lateral resolution criterion.

However, interference is clearly visible in Figure 5.9, decreasing the practical lateral resolution to approximately 5 nm . Nevertheless, spectral analysis of the tip current signal showed that the 10 kHz chopping frequency was effectively removed by the

topo/photo separator described in Section 5.2.4. Rather, the interference is caused by vibrational and electronic sources coupling into the signal, which are also present in regular STM mode without X-rays and the topo/photo separator. Because the STM was originally designed for X-ray scattering experiments, which require precise control over the incident angle and sample height, the STM could not easily be equipped with a vibrational isolation stage [14]. Improvements to suppress the interference are currently under development.

To get a lower bound estimate of the feedback responsivity, we scanned across a Au step edge with a tip repositioning speed of 5000 nm/s. Because the lateral width of the step edge feature is ~ 1 nm with the Au/polymer tip, the height feedback system needs to respond with a frequency of minimally 5 kHz in order to prevent a collision with the step edge. Since no tip-sample collisions occurred, it is clear that the topo/photo current separator allows for height feedback frequencies that are unfeasible with other separation schemes.

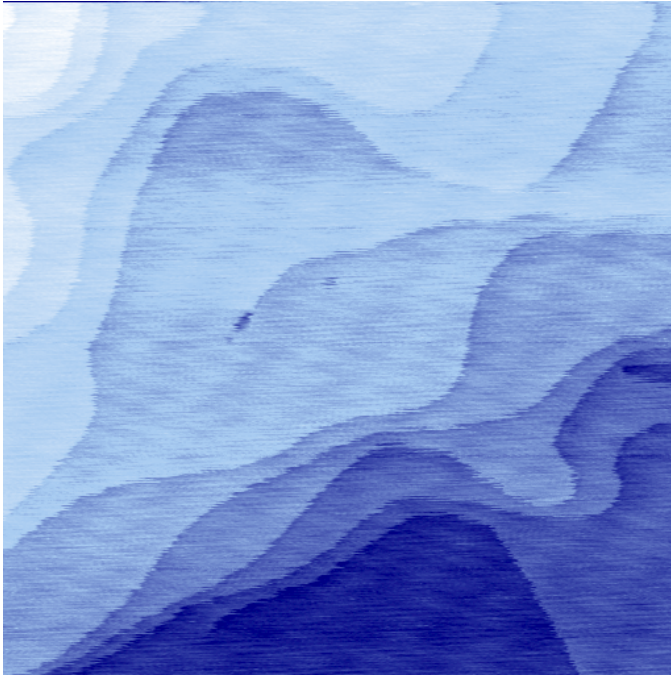


Figure 5.9: STM image of Au(111) recorded using a Au/polymer coaxial tip in a 12.1 keV beam chopped at 10 kHz in 800 mbar Ar, showing atomic steps. The topo/photo current separator was used to obtain the regular tunneling current, the input for the STM control system. Scanning parameters: 640 nm \times 640 nm, ~ 1 nA (excluding offset current), -1 V, tip speed 2500 nm/s.

5.3.4 X-ray induced tunneling current enhancement

The most essential prerequisite in SXSTM measurements is the ability to measure the X-ray induced increase in the tunneling current, which provides the local X-ray absorption information [17,18]. To provide proof of this ability for our instrument, we measured the X-ray-induced current as a function of the regular tunneling current. Figure 5.10 shows the result as recorded on Au(111) in 800 mbar Ar. To obtain the topographic current, the slowly varying X-ray-induced offset current was subtracted from the tunneling current setpoint. The normalized photocurrent was obtained as (X-ray induced current - ion current background)/ion current background, where the ion current background was measured with the tip out of tunneling contact. As can be seen in Figure 5.10, the photocurrent correlates with the regular tunneling signal. This is expected, because the X-ray-induced modification of the tunneling current is assumed to arise from hot secondary electrons [18,38]. Most of the hot electrons do not have sufficient energy to escape from the sample into the vacuum, but they do have a much higher tunneling probability to the tip than electrons at the Fermi level. Still, this enhanced tunneling probability depends on the tip-sample distance, which changes when the topographic tunneling current setpoint is changed. Thus, the clear correlation between the photocurrent and the regular tunneling current provides a proof-of-principle of our ability to performed SXSTM measurements in a gas environment.

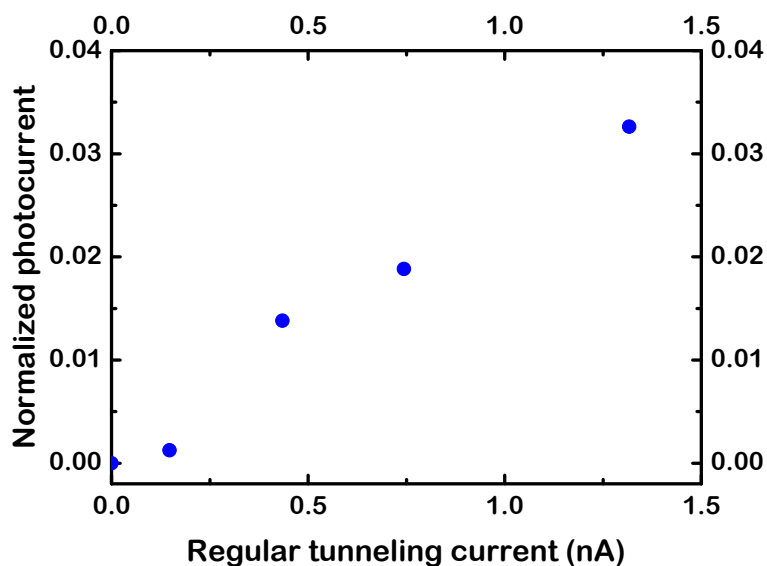


Figure 5.10: X-ray-induced current versus regular tunneling current, recorded on Au(111) in 800 mbar Ar using the topo/photo splitter with the 12.1 keV X-rays chopped at 10 kHz. The normalized photocurrent was obtained as (X-ray induced current-ion current background)/ion current background, where the ion current background was measured with the tip out of tunneling contact. Sample bias: -1 V, tip shield bias: 0 V.

5.4 Conclusion and outlook

We have developed an instrument suitable for performing local X-ray absorption measurements by modification of a previously developed high-pressure STM and X-ray scattering apparatus [14]. Several essential additions have been made in order to reach the required sensitivity to measure the small X-ray-induced modification of the tunneling current that carries the local X-ray absorption signal [17,18].

First, the STM is mounted on a new high-pressure cell with thin windows, providing high X-ray transparency in the energy range of interest, from 8 keV to 25 keV. Furthermore, we have shown that the beam shadow of the STM tip on a 2D X-ray detector can be used to align tip and beam with a precision of a few micrometer. Our measurements show that background currents from ions and photo-electrons cause much more severe signal distortions in a gas environment than in vacuum, particularly in the presence of insulating surfaces. We have therefore applied a Au coating to the high-pressure cell and employed coaxially shielded STM tips. The conductive outer layer of the coaxial tips can be biased to provide additional ion deflection. To separate the regular, 'topographic' tunneling current from the X-ray-induced current, a new high-speed electronics circuit was developed. Using these technical implementations, the X-ray induced modification of the tunneling current was measured on Au(111) in 800 mbar Ar. Combining our methodology with the knowledge of the spatial and chemical resolution of SXSTM developed in the literature [17,18], *operando* X-ray absorption measurements with nanometer spatial resolution have now come within reach.

References

- [1] A.I. Frenkel, J.A. Rodriguez, J.G. Chen, Synchrotron techniques for in situ catalytic studies: Capabilities, challenges, and opportunities, *ACS Catal.* 2 (2012) 2269–2280.
- [2] C.R.A. Catlow, Synchrotron radiation techniques in materials and environmental science, *Philos. Trans. R. Soc. A.* 373 (2015) 20130162.
- [3] K. Devloo-Casier, K.F. Ludwig, C. Detavernier, J. Dendooven, In situ synchrotron based x-ray techniques as monitoring tools for atomic layer deposition, *J. Vac. Sci. Technol. A Vacuum, Surfaces, Film.* 32 (2014) 010801.
- [4] S. Rackwitz, I. Faus, B. Lägél, J. Linden, J. Marx, E. Oesterschulze, K. Schlage, H.C. Wille, S. Wolff, J.A. Wolny, V. Schünemann, Installation of a combined Raman and AFM microscope as a sample environment for nuclear resonance scattering at P01, PETRA III, *Hyperfine Interact.* 226 (2014) 667–671.
- [5] M. V Vitorino, A. Panzarella, L. Porcar, F. Carla, M. Boilot, S. Guerber, P. Bernard, M.S. Rodrigues, F. Sanz, M.I. Giannotti, L. Costa, Custom AFM for X-ray beamlines : in situ biological investigations under physiological conditions research papers, *J. Synchrotron Radiat.* 22 (2015) 1364–1371.
- [6] T. Slobodskyy, a. V. Zozulya, R. Tholapi, L. Liefelth, M. Fester, M. Sprung, W. Hansen, Versatile atomic force microscopy setup combined with micro-focused X-ray beam, *Rev. Sci. Instrum.* 86 (2015) 065104.
- [7] I. Schmid, J. Raabe, B. Sarafimov, C. Quitmann, S. Vranjkovic, Y. Pellmont, H.J. Hug, Coaxial arrangement of a scanning probe and an X-ray microscope as a novel tool for nanoscience, *Ultramicroscopy.* 110 (2010) 1267–1272.
- [8] M.S. Rodrigues, O. Dhez, S. Le Denmat, J. Chevrier, R. Felici, F. Comin, S. Le Denmat, Local detection of X-ray spectroscopies with an in-situ Atomic Force Microscope, *J. Instrum.* 3 (2008) P12004–P12004.
- [9] Z. Ren, F. Mastropietro, A. Davydok, S. Langlais, M.-I. Richard, J.-J. Furter, O. Thomas, M. Dupraz, M. Verdier, G. Beutier, P. Boesecke, T.W. Cornelius, Scanning force microscope for *in situ* nanofocused X-ray diffraction studies, *J. Synchrotron Radiat.* 21 (2014) 1128–1133.
- [10] M.L. Cummings, T.Y. Chien, C. Preissner, V. Madhavan, D. Diesing, M. Bode, J.W. Freeland, V. Rose, Combining scanning tunneling microscopy and synchrotron radiation for high-resolution imaging and spectroscopy with chemical, electronic, and magnetic contrast, *Ultramicroscopy.* 112 (2012) 22–31.
- [11] A. Saito, J. Maruyama, K. Manabe, K. Kitamoto, K. Takahashi, K. Takami, M. Yabashi, Y. Tanaka, D. Miwa, M. Ishii, Y. Takagi, M. Akai-Kasaya, S. Shin, T. Ishikawa, Y. Kuwahara, M. Aono, Development of a scanning tunneling microscope for in situ experiments with a synchrotron radiation hard-X-ray microbeam, *J. Synchrotron Radiat.* 13 (2006) 216–220.
- [12] T. Matsushima, T. Okuda, T. Eguchi, M. Ono, A. Harasawa, T. Wakita, A. Kataoka, M. Hamada, A. Kamoshida, Y. Hasegawa, T. Kinoshita, Development and trial measurement of synchrotron-radiation-light- illuminated scanning tunneling microscope, *Rev. Sci. Instrum.* 75 (2004) 2149–2153.
- [13] K. Tsuji, K. Wagatsuma, K. Sugiyama, K. Hiraga, Y. Waseda, EXAFS- and XANES-like Spectra Obtained by X-ray-excited Scanning Tunneling Microscope Tip

- Current Measurement, *Surf. Interface Anal.* 27 (1999) 132–135.
- [14] W.G. Onderwaater, P.C. van der Tuijn, R. V Mom, S.B. Roobol, M.A. van Spronsen, A. Saedi, J. Drnec, H. Isern, F. Carla, T. Dufrane, R. Koehler, B. Crama, I.M.N. Groot, R. Felici, J.W.M. Frenken, Combined scanning probe microscopy and X-ray scattering instrument for in situ catalysis investigations, *Rev. Sci. Instrum.* (2016) accepted.
- [15] M.S. Rodrigues, T.W. Cornelius, T. Scheler, C. Mocuta, A. Malachias, R. Magalhães-Paniago, O. Dhez, F. Comin, T.H. Metzger, J. Chevrier, In situ observation of the elastic deformation of a single epitaxial SiGe crystal by combining atomic force microscopy and micro x-ray diffraction, *J. Appl. Phys.* 106 (2009) 103525.
- [16] C. Leclere, T.W. Cornelius, Z. Ren, A. Davydok, J.S. Micha, O. Robach, G. Richter, L. Belliard, O. Thomas, In situ bending of an Au nanowire monitored by micro Laue diffraction, *J. Appl. Crystallogr.* 48 (2015) 291–296.
- [17] N. Shirato, M. Cummings, H. Kersell, Y. Li, B. Stripe, D. Rosenmann, S.W. Hla, V. Rose, Elemental fingerprinting of materials with sensitivity at the atomic limit, *Nano Lett.* 14 (2014) 6499–6504.
- [18] T. Okuda, T. Eguchi, K. Akiyama, A. Harasawa, T. Kinoshita, Y. Hasegawa, M. Kawamori, Y. Haruyama, S. Matsui, Nanoscale chemical imaging by scanning tunneling microscopy assisted by synchrotron radiation, *Phys. Rev. Lett.* 102 (2009) 105503.
- [19] T. Eguchi, T. Okuda, T. Matsushima, A. Kataoka, A. Harasawa, K. Akiyama, T. Kinoshita, Y. Hasegawa, M. Kawamori, Y. Haruyama, S. Matsui, Element specific imaging by scanning tunneling microscopy combined with synchrotron radiation light, *Appl. Phys. Lett.* 89 (2006) 243119.
- [20] A. Saito, K. Takahashi, Y. Takagi, K. Nakamatsu, K. Hanai, Y. Tanaka, D. Miwa, M. Akai-kasaya, S. Shin, S. Matsui, T. Ishikawa, Y. Kuwahara, M. Aono, Study for noise reduction in synchrotron radiation based scanning tunneling microscopy by developing insulator-coat tip, *Surf. Sci.* 601 (2007) 5294–5299.
- [21] K. Akiyama, T. Eguchi, T. An, Y. Hasegawa, T. Okuda, A. Harasawa, T. Kinoshita, Fabrication of a glass-coated metal tip for synchrotron-radiation-light-irradiated scanning tunneling microscopy, *Rev. Sci. Instrum.* 76 (2005) 1–3.
- [22] H. Yan, M. Cummings, F. Camino, W. Xu, M. Lu, X. Tong, N. Shirato, D. Rosenmann, V. Rose, E. Nazaretski, Fabrication and characterization of CNT-based smart tips for synchrotron assisted STM, *J. Nanomater.* 2015 (2015) 492657.
- [23] V. Rose, T.Y. Chien, J. Hiller, D. Rosenmann, R.P. Winarski, X-ray nanotomography of SiO₂-coated Pt₉₀Ir₁₀ tips with sub-micron conducting apex, *Appl. Phys. Lett.* 99 (2011) 173102.
- [24] K. Wang, D. Rosenmann, M. Holt, R. Winarski, S.W. Hla, V. Rose, An easy-to-implement filter for separating photo-excited signals from topography in scanning tunneling microscopy, *Rev. Sci. Instrum.* 84 (2013) 063704.
- [25] R. Van Rijn, M.D. Ackermann, O. Balmes, T. Dufrane, A. Geluk, H. Gonzalez, H. Isern, E. De Kuyper, L. Petit, V.A. Sole, D. Wermeille, R. Felici, J.W.M. Frenken, Ultrahigh vacuum/high-pressure flow reactor for surface x-ray diffraction and

- grazing incidence small angle x-ray scattering studies close to conditions for industrial catalysis, *Rev. Sci. Instrum.* 81 (2010) 014101.
- [26] M.J. Rost, L. Crama, P. Schakel, E. Van Tol, G.B.E.M. Van Velzen-Williams, C.F. Overgaw, H. Ter Horst, H. Dekker, B. Okhuijsen, M. Seynen, A. Vijftigschild, P. Han, A.J. Katan, K. Schoots, R. Schumm, W. Van Loo, T.H. Oosterkamp, J.W.M. Frenken, Scanning probe microscopes go video rate and beyond, *Rev. Sci. Instrum.* 76 (2005) 053710.
- [27] C.T. Herbschleb, P.C. van der Tuijn, S.B. Roobol, V. Navarro, J.W. Bakker, Q. Liu, D. Stoltz, M.E. Cañas-Ventura, G. Verdoes, M.A. van Spronsen, M. Bergman, L. Crama, I. Taminiau, A. Ofitserov, G.J.C. van Baarle, J.W.M. Frenken, The ReactorSTM: atomically resolved scanning tunneling microscopy under high-pressure, high-temperature catalytic reaction conditions., *Rev. Sci. Instrum.* 85 (2014) 083703.
- [28] S.B. Roobol, M.E. Cañas-Ventura, M. Bergman, M.A. Van Spronsen, W.G. Onderwaater, P.C. Van Der Tuijn, R. Koehler, A. Ofitserov, G.J.C. Van Baarle, J.W.M. Frenken, The ReactorAFM: Non-contact atomic force microscope operating under high-pressure and high-temperature catalytic conditions, *Rev. Sci. Instrum.* 86 (2015) 033706.
- [29] J.C.D. B.L. Henke, E.M. Gullikson, X-Ray Interactions: Photoabsorption, Scattering, Transmission, and Reflection at $E = 50\text{--}30,000$ eV, $Z = 1\text{--}92$, *At. Data Nucl. Data Tables.* 54 (1993) 181–324.
- [30] S.J. Schowalter, C.B. Connolly, J.M. Doyle, Permeability of noble gases through Kapton, butyl, nylon, and “Silver Shield,” *Nucl. Instruments Methods Phys. Res. Sect. A Accel. Spectrometers, Detect. Assoc. Equip.* 615 (2010) 267–271.
- [31] S.L.M. Schroeder, G.D. Moggridge, R.M. Ormerod, T. Rayment, R.M. Lambert, What determines the probing depth of electron yield XAS?, *Surf. Sci.* 324 (1995) L371–L377.
- [32] S.L.M. Schroeder, G.D. Moggridge, T. Rayment, R.M. Lambert, In situ probing of the near-surface properties of heterogeneous catalysts under reaction conditions: An introduction to total electron-yield XAS, *J. Mol. Catal. A Chem.* 119 (1997) 357–365.
- [33] W.J. Miloch, S. V. Vladimirov, Charging of spinning insulating objects by plasma and photoemission, *Geophys. Res. Lett.* 36 (2009) L18110.
- [34] M. Salmeron, R. Schlögl, Ambient pressure photoelectron spectroscopy: A new tool for surface science and nanotechnology, *Surf. Sci. Rep.* 63 (2008) 169–199.
- [35] D.E. Starr, Z. Liu, M. Hävecker, A. Knop-Gericke, H. Bluhm, Investigation of solid/vapor interfaces using ambient pressure X-ray photoelectron spectroscopy., *Chem. Soc. Rev.* 42 (2013) 5833–57.
- [36] A.J. Bard, M. V. Mirkin, *Scanning Electrochemical Microscopy*, CRC Press, 6000 Broken Sound Parkway, Boca Raton, United States, 2012.
- [37] C. Ponchut, J.M. Rigal, J. Clément, E. Papillon, A. Homs, S. Petittedmange, MAXIPIX, a fast readout photon-counting X-ray area detector for synchrotron applications, *J. Instrum.* 6 (2011) C01069–C01069.
- [38] C.Y. Chiu, Y.L. Chan, Y.J. Hsu, D.H. Wei, Collecting photoelectrons with a scanning tunneling microscope nanotip, *Appl. Phys. Lett.* 92 (2008) 103101.

Summary and outlook

The work in this thesis showcases how close, at present, we can approach the catalysts and conditions in the chemical industry using high-pressure scanning tunneling microscopy (STM), while maintaining atomic-level detail. Evidently, flat and conductive model catalysts remain a requirement. However, the use of thin oxide films onto which nanoparticles can be deposited does allow one to prepare model catalysts that contain many of the characteristics of their industrial counterparts.

A key aspect in catalysis is to couple structural features to reactivity. Essential to obtaining such structure-activity relationships is to have control over the model catalyst structure. We investigated the example of the preparation of MoO_x nanoparticles on $\text{Al}_2\text{O}_3/\text{NiAl}(110)$. Two methods were used: direct deposition of MoO_x and the deposition of Mo in 5×10^{-7} mbar O_2 . Despite the fact that both methods yield highly oxidized MoO_x particles, MoO_x prepared via direct deposition of MoO_x produces smaller particles. We interpret this finding in terms of the interaction between the deposited material and the support, which is stronger for MoO_x than for Mo. The observed difference between the two preparation methods suggests that the Mo atoms are oxidized typically only after having attached to a stable Mo or MoO_x nucleus. This interpretation suggests that by increasing the O_2 pressure during the deposition of Mo, one can make a continuous transition from low to high dispersion. Thus, valuable size control may be obtained for the investigation of the size-activity relation of $\text{MoO}_x/\text{Al}_2\text{O}_3$ catalysts.

A major drawback of using a thin oxide film as support is that the film may not be stable under high-pressure conditions, particularly at elevated temperature. The $\text{MoO}_x/\text{Al}_2\text{O}_3/\text{NiAl}(110)$ catalyst proved to be unstable towards H_2S and O_2 even in ultrahigh vacuum, due to the catalytic effect of MoO_x in the dissociation of H_2S and O_2 . Hence, an important challenge for the future is to identify which model supports are suitable for high-pressure studies. One promising direction could be the use of oxide films deposited on noble metals such as FeO_x on $\text{Pt}(111)$ or $\text{Au}(111)$, and MgO on $\text{Ag}(100)$, because the metal substrates in these cases are relatively inert. Alternatively, conductive (doped) bulk oxides such as TiO_2 and $\alpha\text{-Fe}_2\text{O}_3$ could be employed, possibly in combination with Al_2O_3 or SiO_2 films.

Shifting the focus to realistic operating conditions, we studied the structure of MoS_2 nano-islands on $\text{Au}(111)$ during the hydrodesulfurization reaction, in which sulfur is removed from organic molecules. While the Au support is clearly not representative of the industrial alumina support, this study represents the first case in which a nanoparticle catalyst is imaged with single atom resolution under working conditions. Using our corrosion resistant high-pressure STM, we imaged the catalyst in H_2 and during the desulfurization of CH_3SH . The images show that the active edge sites of the catalyst nano-islands adapt their sulfur, hydrogen, and hydrocarbon coverages depending on the gas environment. By comparing the observations to density

functional theory calculations, we propose that the dominant edge structure during the desulfurization of CH_3SH contains a mixture of adsorbed sulfur and CH_3SH . Counterintuitively, the edge sulfur content is reduced by the presence of CH_3SH . In contrast, our theoretical analysis shows that a subtle lowering of the C-S bond-breaking barrier would result in sulfur deposition that is able to push the edge sulfur coverage far above its equilibrium value.

Like all surface science studies, our investigation of the hydrodesulfurization reaction only has a phenomenological comparability to industrial catalysis. However, high-pressure, high-temperature studies increase the chance to observe *relevant* phenomena, which also occur under industrial conditions. To further close the gap between our experiments and industrial practice, future experiments could increase the complexity of both the catalyst and the reactant feed. To improve the catalyst, $\text{TiO}_2(110)$ may be used as a support and Co or Ni promoters could be added. Especially the latter will have a profound effect on the reaction mechanism, as Co and Ni are known to replace Mo at the active edge sites. To approach a more realistic feed, heavier organosulfur molecules may be used, such as thiophenes. These molecules are significantly more difficult to desulfurize than CH_3SH , and hence are of greater interest.

Improvement of the understanding of catalysis may especially benefit processes that have not yet made it all the way to industrial use. Examples of such processes are oxidation reactions on oxide-supported gold catalysts, which provide a unique set of pathways for green chemistry. To investigate whether Au surface oxides may play a role in the catalysis, we studied their autocatalytic formation and stability on $\text{WO}_3/\text{Au}(111)$ and $\text{ReO}_3/\text{Au}(111)$ inverse model catalysts. We find that Au surface oxides are thermodynamically stable over a wide range of catalytically relevant conditions. The formation of the surface oxides requires initial seeds of AuO_x on our model catalysts, but proceeds autocatalytically from there on, with an O_2 dissociation barrier that is mainly entropic. Thus, our data indicate that Au surface oxides at the gas-surface interface of Au oxidation catalysts should be considered as a feasible reaction intermediate.

Two key questions that remain are whether the initial seeds of AuO_x can be generated on oxide-supported Au nanoparticles under typical reaction conditions, and whether the oxide formation rate balances out against the oxide consumption by the reactant that is being oxidized. High-pressure STM observations on various types of oxide nanoparticles on $\text{Au}(111)$ during CO oxidation could provide the answer to these questions, although such inverted catalysts may behave differently than the real catalyst. Alternatively, one may image Au nanoparticles on TiO_2 or CeO_2 . Although atomic resolution will not be achievable easily on the nanoparticles, changes in the particle height could provide a good indication for the presence of AuO_x . The presence of an oxide will affect the surface free energy of the Au particles and hence their aspect ratio.

To further improve the possibilities of high-pressure STM, we have developed an instrument that combines STM with synchrotron X-ray radiation, enabling chemical sensitivity in the images. By using the tip as a local X-ray absorption detector, one should be able to identify which type of atom is sitting where on the surface with nanometer spatial resolution. When performed in situ, such measurements could provide vital information on the distribution of promoters and reaction intermediates over the catalyst. The local chemical contrast can be obtained by measuring the X-ray induced increase in the tunnel current, which strongly depends on the proximity of X-ray absorbing atoms to the tunnel junction. Because this signal is extremely small compared to the ion currents generated in the gas phase, we used coaxially shielded STM tips. The conductive outer shield of the coaxial tips can be biased to deflect ions away from the tip core. In tunneling contact, the X-ray-induced current is separated from the regular topographic tunneling current using a novel high-speed separation scheme. Using these developments, we were able to detect the local X-ray-induced current on Au(111) in 800 mbar Ar.

After this proof-of-principle for the instrument, the next step is to obtain chemical contrast maps with high spatial resolution. Although the primary focus will initially be technical, a wide range of interesting future studies is possible. For instance, it should be possible to follow adsorbate-induced local changes in the chemical composition of alloys. Another possibility would be to pinpoint the local oxidation state of a substrate during its oxidation or reduction using the local white line absorption intensity.

Although by no means a plug-and-play technique, high-pressure STM has come to the point where the main focus can be on science rather than instrument development. The study of single crystals as well as more complex model catalysts shows that high pressures induce changes in the structure and mechanism of nearly all catalytic systems, which highlights the importance of the transition from vacuum to industrial conditions. Despite the limitations imposed by the requirement of flat and conductive samples, high-pressure STM allows for an unparalleled level of detail in its view on catalysts and should therefore play a key role in *operando* catalysis research. By combining it with X-rays or spectroscopic techniques, an even more complete picture of model catalysts can be drawn.

Samenvatting

Een van mijn eerste ervaringen met chemie had ik toen ik als kind een krijtje in een bakje azijn gooide. Dit gaat stevig bruisen door de CO_2 -belletjes die vrijkomen. Twee stoffen simpelweg bij elkaar brengen en er ontstaan spontaan belletjes, voor mij als kind had het iets weg van magie. In de chemische industrie is het echter zelden zo simpel. De meeste reacties starten namelijk niet vanzelf als je de reactanten bij elkaar brengt. Op moleculair niveau bestaan reacties uit het overhevelen van atomen uit het ene molecuul naar het andere. Om dat te kunnen doen, moeten de moleculen zich meestal vervormen en dat kost energie. Bij kamertemperatuur hebben moleculen vaak niet genoeg energie om over een dergelijke barrière heen te komen. De simpele oplossing: stop de reactanten in een vat en maak dat heet. Zo kun je al heel wat chemie doen. Je kunt bijvoorbeeld staal maken uit ijzererts en kolen. Vaak zijn echter wel erg hoge temperaturen nodig, waardoor er veel energie verloren gaat bij het verhitten van het reactorvat. Ook vindt veelal de verkeerde reactie plaats. Neem de productie van waterstofperoxide (H_2O_2), beter bekend als bleekmiddel. Dit zou je kunnen maken door waterstof (H_2) en zuurstof (O_2) met elkaar te laten reageren. Als je deze gassen echter mengt in een heet reactorvat, dan volgt een explosie waarbij water (H_2O) ontstaat in plaats van H_2O_2 .

Om toch bij het gewenste product te komen maakt de chemische industrie gebruik van katalysatoren, stoffen die een specifieke reactie versnellen zonder dat ze zelf verbruikt worden. Zo'n katalysator bindt de reactanten en vervormt ze, zodat ze makkelijker kunnen reageren. In het geval van H_2O_2 -productie gebeurt dit in twee stappen. Eerst wordt H_2 in losse atomen gesplitst aan het oppervlak van een palladium katalysator. De waterstofatomen worden vervolgens doorgegeven aan een tweede katalysator, anthraquinoon, die ze op een O_2 -molecuul kan zetten, zodat H_2O_2 gevormd wordt.

Een goede katalysator bindt de reactanten precies sterk genoeg, zodat ze goed genoeg vervormd zijn om te kunnen reageren, maar niet zo sterk dat ze aan de katalysator blijven plakken. Dit lijkt een simpel criterium, maar het vinden van een goede katalysator is nog altijd een hele opgave. Hoe sterk een katalysator bindt hangt namelijk niet alleen af van welk materiaal hij gemaakt is, maar ook van zijn oppervlaktestructuur. De palladiumkatalysator uit de vorige paragraaf bestaat uit heel kleine brokjes, nanodeeltjes, die vastzitten op een dragermateriaal. Die brokjes kunnen verschillende vormen aannemen, zoals een bal of een kubusvorm. Palladiumatomen op de hoekpunten van zo'n kubus binden waterstof heel anders dan die op de vlakken. De palladiumkatalysator heeft dus verschillende soorten bindingsplekken, waarvan sommige de reactie veel beter katalyseren dan andere. In industriële katalysatoren zitten niet alleen palladium en een drager, maar ook allerlei additieven. Hierdoor is de structuur van zo'n katalysator nog complexer, en zijn er honderden of zelfs duizenden verschillende bindingsplekken aanwezig. Om een betere

katalysator te maken, moeten er zoveel mogelijk bindingsplekken van het goede soort worden gemaakt. Zie maar eens uit te vinden welke soort dat is!

De chemische industrie lost de zoektocht naar betere katalysatoren op door simpelweg heel veel potentiële katalysatoren uit te proberen. Dit is een tijdrovend proces. Neem het voorbeeld van de katalysator voor de verwijdering van zwavel uit olie, noodzakelijk voor de productie van schone benzine. Het is al zo'n 90 jaar bekend dat een gemengde kobalt-molybdeensulfide hier een goede katalysator voor is. Toch worden er na al die jaren onderzoek nog altijd betere katalysatoren gevonden door de structuur van het kobalt-molybdeensulfide verder te optimaliseren.

Ondanks de moeizame trial-and-errormethode om katalysatoren te vinden is de chemische industrie erin geslaagd ons van hoge kwaliteit materialen, medicijnen en energie te voorzien. Het wordt echter steeds duidelijker dat de huidige aardolie-gebaseerde chemie niet houdbaar is op de lange termijn, wat ons noodzaakt om over te stappen op groene chemie. Dit vergt enorme veranderingen in de chemische industrie, waarin nieuwe katalytische processen zullen moeten worden ontwikkeld. De trial-and-errormethode die de chemische industrie op dit moment gebruikt om katalysatoren te vinden volstaat niet voor een vlotte overgang. Er zal daarom meer gericht gezocht moeten worden op basis van kennis over hoe katalysatoren op atomair niveau werken. Er wordt dan ook intensief onderzoek gedaan om zulk atomair begrip te creëren. Dit proefschrift draagt daar een steentje aan bij.

ReactorSTM

Om te weten hoe een katalysator er op atomaire schaal uitziet heb je speciale meettechnieken nodig. Hoewel er een heel scala van zulke technieken is ontwikkeld, is de meest voor de hand liggende strategie om extreem ingezoomde plaatjes van katalysatoren te maken. Met een gewone lichtmicroscop kun je echter niet ver genoeg inzoomen. Daarom zijn speciale microscopen ontwikkeld die op een andere manier plaatjes maken. In mijn proefschrift heb ik gebruik gemaakt van zo'n type microscoop, een zogenaamde rastertunnelmicroscop (in het Engels scanning tunneling microscopy, STM). Bij deze techniek kijk je niet naar de katalysator, maar tast je het oppervlak af zoals een blinde braille leest. Dat gebeurt door middel van een heel scherp naaldje, waarmee het tasten slechts door één atoom wordt gedaan. De microscoop "voelt" het oppervlak door een heel klein stroompje dat tussen het katalysatoroppervlak en het naaldje loopt. Door het oppervlak systematisch lijntje voor lijntje af te tasten kunnen zo plaatjes worden gemaakt, waarin de posities van de atomen van de katalysator zichtbaar zijn. Om een idee te geven hoe klein dit is: een haar is zo'n 200.000 keer dikker dan een atoom.

Meestal worden STM-plaatjes bij lage temperatuur en in vacuüm gemaakt. Onder zulke condities staat nagenoeg alles stil aan het katalysatoroppervlak, zodat er alle tijd is om het oppervlak heel rustig en precies af te beelden. In de industrie werken katalysatoren juist bij hoge druk en temperatuur. In de afgelopen decennia is duidelijk geworden dat de katalysatordeeltjes hun oppervlaktestructuur kunnen aanpassen aan

de gasomgeving. Daarom is het mogelijk dat plaatjes van katalysatoren die zijn opgenomen bij lage druk en temperatuur een heel verkeerd beeld geven van hoe een werkende katalysator eruit ziet.

Om ook katalysatoren in actie te kunnen vastleggen is in Leiden de ReactorSTM ontwikkeld. Dit is een rastertunnelmicroscopie die in een klein reactorvat is ingebouwd. Alleen onderdelen waarvoor het strikt noodzakelijk is zijn binnen de reactor geplaatst, terwijl alle overige onderdelen juist zijn afgeschermd. Daardoor is het mogelijk om bij hoge gasdruk en hoge temperatuur te meten. Voor mijn onderzoek heb ik verdere aanpassingen gedaan waardoor het ook mogelijk is om in zeer agressieve gassen te meten, zoals H₂S (rotte-eierengas).

Modelkatalysatoren

Omdat de duizenden verschillende bindingsplekken in een industriële katalysator niet tegelijk bestudeerd kunnen worden, maakt men voor onderzoek op atomair niveau gebruik van versimpelde modelkatalysatoren. Een goede modelkatalysator lijkt aan de ene kant zoveel mogelijk op de industriële versie, maar heeft aan de andere kant een vereenvoudigde, goed gecontroleerde structuur. Het maken van zulke modelkatalysatoren is daarom een kunst op zich. Voor katalysatoren die uit metaalnanodeeltjes bestaan hebben we die kunst behoorlijk onder controle. Voor metaaloxides (bijvoorbeeld roest), die bestaan uit metaal- en zuurstofatomen, zijn we echter nog minder ver. In Hoofdstuk 2 van dit proefschrift bestudeer ik twee methodes om modelmetaaloxidekatalysatoren te maken. In de ene methode maak ik metaaloxidenanodeeltjes door een dragermateriaal bloot te stellen aan metaaloxidedamp. In de andere methode gebruik ik metaaldamp gemengd met een heel klein beetje zuurstof (ongeveer een miljardste van de zuurstofdruk in lucht). Hoewel deze methodes heel erg op elkaar lijken, levert de metaaldampmethode veel grotere deeltjes op dan de metaaloxidedampmethode. Op deze manier is het dus mogelijk om te kijken hoe de katalytische activiteit van de metaaloxide deeltjes afhangt van de deeltjesgrootte.

Katalysatoren in actie bekijken

Met de ReactorSTM is het mogelijk om modelkatalysatoren zoals beschreven in de vorige paragraaf te bekijken terwijl ze 'in actie' zijn. In Hoofdstuk 3 laat ik zien hoe het mij als eerste ter wereld gelukt is om op deze manier individuele atomen in werkende katalysatornanodeeltjes vast te leggen. Het proces dat ik bestudeerd heb is de ontzwareling van organische moleculen. Dit proces wordt gebruikt om aardolie schoon te maken, zodat er bijvoorbeeld benzine van kan worden gemaakt. De katalysator bestaat uit driehoekige MoS₂-nanodeeltjes, die ik in mijn onderzoek op een heel vlak stukje goud heb gelegd, zodat het mogelijk was de deeltjes met de STM af te beelden. Op deze manier heb ik kunnen laten zien hoe de structuur van de MoS₂-eilanden afhangt van de gascompositie in de reactor. De verschillen bleken klein, maar wel erg belangrijk. Alleen aan de randen van de deeltjes veranderen de hoeveelheden geadsorbeerd zwavel, waterstof en organische moleculen. De randen zijn echter wel

dé plekken die ertoe doen, omdat hier alle katalytische reacties plaatsvinden. De kennis van de hoeveelheid adsorbaten op de randen van de MoS₂-eilanden is noodzakelijke informatie om te begrijpen hoe de katalysator de reactanten bindt. Tot nu toe was het onmogelijk om deze informatie te verkrijgen, omdat er geen manier was om de katalysator in het agressieve reactantenmengsel af te beelden.

In Hoofdstuk 4 kijk ik naar het oppervlak van een andere katalysator, namelijk goud. Dit klinkt heel opmerkelijk, want goud staat bekend als een materiaal dat chemisch niets doet. Als je goud tot nanodeeltjes verpoedert, blijkt het echter een fantastische katalysator te zijn voor oxidatiereacties, waarin zuurstofatomen op moleculen worden gezet. Hoe dat komt is nog niet duidelijk. Wel lijkt het erop dat het dragermateriaal waarop de gouddeeltjes vastzitten samenwerkt met de gouddeeltjes in de reactie om de O₂-moleculen te splitsen. De vraag die ik heb onderzocht, is of die gesplitste zuurstofmoleculen op de katalysator opgeslagen kunnen worden in de vorm van goudoxide (goudroest). Een blok goud roest natuurlijk niet, maar onder bepaalde omstandigheden is het wel mogelijk om een dun oxidelaagje aan het oppervlak te maken. In Hoofdstuk 4 laat ik zien dat dit oxidelaagje behoorlijk stabiel is, zelfs als er maar heel weinig zuurstof beschikbaar is. De structuur van het oxidelaagje hangt af van de temperatuur en de zuurstofdruk.

Nieuwe methode om katalysatoren in actie te bestuderen

Hoewel STM een extreem nuttige techniek is om de structuur van katalysatoren te bepalen, is de techniek “chemisch blind”. Het is namelijk niet zomaar uit de plaatjes op te maken om wat voor soort atomen het gaat. Om dergelijke chemische informatie te verkrijgen wordt vaak röntgenabsorptiespectroscopie gebruikt. Net als bij zichtbaar licht hebben stoffen ook voor röntgenstralen een kleur. Bij röntgenstralen is die kleur heel specifiek voor wat voor soort atomen er in het materiaal zitten en wat hun chemische toestand is. Röntgenabsorptiespectroscopie meet de “röntgenkleur” van de katalysator, en bepaalt daarmee wat voor soort atomen erin zitten, hoeveel en in welke chemische toestand ze zich bevinden. Echter, de techniek kan niet vertellen *waar* de atomen zich in de katalysator bevinden.

In Hoofdstuk 5 laat ik zien hoe ik, in samenwerking met de wetenschappers van de ID03-bundellijn van de European Synchrotron Radiation Facility (een heel intense bron van röntgenstraling), de eerste stap gezet heb om een ReactorSTM te combineren met röntgenabsorptiespectroscopie. Door het STM-naaldje te gebruiken als lokale röntgenabsorptiedetector zou het mogelijk moeten worden om niet alleen te bepalen waar atomen zich bevinden op het katalysatoroppervlak, maar ook wat voor soort atomen het zijn en wat hun chemische toestand is. Voor metingen in vacuüm is al aangetoond dat dit mogelijk is. In Hoofdstuk 5 laat ik zien welke aanpassingen nodig zijn om ook bij hogere gasdruk te kunnen meten. Hoewel de ontwikkeling zich nog in een vroeg stadium bevindt, toon ik de eerste proefmetingen.

Acknowledgments

Throughout the years that I spent in Leiden, many have played a part in the work presented in this thesis. With some I collaborated, others helped me simply out of kindness. In this last category, I would like to thank Marcel Rost, Gertjan van Baarle, Matthijs van Spronsen and Sander Roobol. My (lengthy) discussions with Marcel provided me with a firm technical basis and a very critical view on my own results. Gertjan's perceptive and didactic notions have been a similar inspiration. Matthijs and Sander I thank for being good company on the one hand, but also for their sharp contributions and ideas.

My supervisors, Joost Frenken and Irene Groot, I thank for their trust, deep pockets, and inspiration. They have given me the opportunity to pursue my own ideas, while embellishing them with a firm sense of realism and scientific background. Ellie van Rijsewijk I thank for being that silent force that makes everything run smoothly behind the scenes.

I am grateful to my collaborators in and outside the group: Willem Onderwaater, Anja Sjøstad, Jaap Louwen, Oleksii Ivashenko, Mahesh Prabhu, Maciej Jankowski, Francesco Carlà, Roberto Felici, Leon Jacobse, Stephan Steinmann, Sigismund Melissen, Vincent Vandalon, and Paul Alkemade. They spent real time and effort into making our joint projects successful. Similarly, my students Sabine Wenzel, Joost Vermeer and Matthijs van Weeren provided valuable contributions to my work.

The technical support staff in Leiden and at the ESRF, Peter van der Tuijn, Mirthe Bergman, Bert Crama, Peter van Veldhuizen, Ko Koning, Fred Schenkel, Merlijn Camp, René Overgaww, Johan Bakker, Thomas Dufrane, Hervé Gonzalez, and Helena Isern, I thank for the high-quality instruments, tools, supplies and insights they delivered.

I highly value the discussions with Jaap Louwen, Eelco Vogt and Bart Nelissen from Albemarle, and Stig Helveg from Haldor Topsøe. I gratefully acknowledge the financial support from the NIMIC consortium. Finally, I would like to thank all my (former) group members for the enjoyable, fruitful, and exciting moments we shared.

List of publications

Peer-reviewed publications

1. A. I. Yanson, P. Rodriguez, N. Garcia-Araez, R.V. Mom, F.D. Tichelaar, M.T.M. Koper
Cathodic Corrosion: A Quick, Clean, and Versatile Method for the Synthesis of Metallic Nanoparticles
Angew. Chem. Int. Ed., **2011**, 50, 6346–6350
2. R.V. Mom, C. Hahn, L. Jacobse, L.B.F. Juurlink
LEED Analysis of Nickel Cylindrical Single Crystal
Surface Science, **2013**, 613, 15-20
3. R.V. Mom, J. Cheng, M.T.M. Koper, M. Sprik
Modeling the Oxygen Evolution Reaction on Metal Oxides: The Influence of Unrestricted DFT Calculations
J. Phys. Chem. C, **2014**, 118, 4095-4102
4. R.V. Mom, M.J. Rost, J.W.M. Frenken, I.M.N. Groot
Tuning the Properties of Molybdenum Oxide on Al₂O₃/NiAl(110): Metal Versus Oxide Deposition
J. Phys. Chem. C, **2016**, 120, 19737–19743
5. W.G. Onderwaater, P.C. van der Tuijn, R.V. Mom, M.A. van Spronsen, S.B. Roobol, A. Saedi, J. Drnec, H. Isern, F. Carlà, T. Dufrane, R. Koehler, B. Crama, I.M.N. Groot, R. Felici, J.W.M. Frenken
Combined scanning probe microscopy and X-ray scattering instrument for in situ catalysis investigations
Rev. Sci. Instr., **2016**, 87, 113705
6. R.V. Mom, W.G. Onderwaater, M.J. Rost, M. Jankowski, S. Wenzel, L. Jacobse, P.F. A. Alkemade, V. Vandalon, M.A. van Spronsen, M. van Weeren, B. Crama, P. van der Tuijn, R. Felici, W.M.M. Kessels, F. Carlà, J.W.M. Frenken, I.M.N. Groot
Simultaneous scanning tunneling microscopy and synchrotron X-ray measurements in a gas environment
Submitted
7. R.V. Mom, S. Wenzel, M.K. Prabhu, J.W.M. Frenken, I.M.N. Groot
The growth and stability of Au surface oxides on WO₃/Au(111) and ReO₃/Au(111) inverse model catalysts
Submitted

8. R.V. Mom, J. Louwen, J.W.M. Frenken, I.M.N Groot
In situ observations of an active MoS₂ model hydrodesulfurization catalyst
Submitted
9. R.V. Mom, O. Ivashenko, J.W.M. Frenken, I.M.N. Groot, A.O. Sjøstad
The nucleation and thermal stability of Re and Co-Re nanoparticles on Al₂O₃/NiAl(110)
In preparation
10. R.V. Mom, S.N. Steinmann, S.T. Melissen, J.W.M. Frenken, P. Sautet, I.M.N. Groot
The adsorption of CH₃SH on Au(111) from vacuum to 1 bar
In preparation
11. R.V. Mom, J. Vermeer, J.W.M. Frenken, I.M.N. Groot
Crystalline Al₂O₃ on NiAl(110) beyond two-layer thickness
In preparation

Other publications

R.V. Mom

Oppervlaktewetenschap onder druk (Surface science under pressure)
Review article on high-pressure surface science in the NEVAC-Blad, the journal of the Netherlands Vacuum Society.

Curriculum Vitae

Rik Mom was born on the 28th of November 1988 in Haarlem, The Netherlands. He graduated from Atheneum College Hageveld in Heemstede in 2007 after manufacturing a prototype of a prosthetic arm in the framework of his school research project. Mom continued his studies through a Bachelor Degree in Molecular Science and Technology at Leiden University and Delft University of Technology in the Netherlands. He obtained his B.Sc. degree after a research project on the corrosion of gold and platinum under anodic and alternating potentials under the supervision of Dr. Alex Yanson and Prof. Marc Koper.

During his Master in Chemistry at Leiden University, Mom investigated the structure and H₂ adsorption properties of a Ni cylindrical crystal under the supervision of Dr. Ludo Juurlink. Before graduating Cum Laude, he performed a research project at the University of Cambridge, UK, in the group of Prof. Michiel Sprik. Under daily supervision of Dr. Jun Cheng, he studied the effects of spin restriction in density functional theory calculations on the binding energies of oxygen evolution reaction intermediates.

Mom pursued a Ph.D. project in the group of Prof. Joost Frenken at the Huygens-Kamerlingh Onnes laboratory, Leiden Institute of Physics, Leiden. After Frenken became director of the Advanced Research Center for Nanolithography in Amsterdam, in 2014, Dr. Irene Groot headed the group and became Mom's co-promotor. Most of the work performed during the project is described in this thesis.

After his Ph.D. defense, Mom will continue his academic research as a postdoc in the group of Dr. Axel Knop-Gericke at the Fritz-Haber-Institute in Berlin.